SCUOLA DI DOTTORATO
UNIVERSITÀ DEGLI STUDI DI MILANO-BICOCCA

Dipartimento di / Department of

FISICA “Giuseppe Occhialini”

Dottorato di Ricerca in / PhD program FISICA E ASTRONOMIA Ciclo / Cycle XXXIV

Curriculum in (se presente / if it is) FISICA SUBNUCLEARE

Search for the lepton flavour violating process $\tau^- \rightarrow \mu^+\mu^-\mu^-$ in the CMS experiment at the LHC with Run-II data

Cognome / Surname GUZZI Nome / Name LUCA

Matricola / Registration number 763189

Tutore / Tutor: dott.ssa SANDRA MALVEZZI

Coordinatore / Coordinator: prof.ssa MARTA CALVI

ANNO ACCADEMICO / ACADEMIC YEAR 2020-2021

Abstract

In this thesis, a search for Lepton Flavour Violating $\tau \to 3\mu$ *decays is performed using* τ *leptons coming from the* $W \to \tau\nu$, $D \to \tau\nu$ *and* $B \to \tau\nu$ *processes, using 146.9* fb^{-1} *of proton-proton collision data collected by CMS during Run-II. The expected upper limit on BR(*$\tau \to 3\mu$*) is estimated to be* 2.3×10^{-8} *at 90% of confidence level.*

Contents

List of Figures

List of Tables

Preface

The Large Hadron Collider (LHC) is a 27 km circumference proton-proton collider built at CERN with the goal of investigating the physics processes manifesting at the TeV scale. It started its operations in 2009, colliding two proton beams at the center of mass energy of 0.9 TeV. This energy was then gradually increased up to 13 TeV in 2015, which represents the highest energy reached so far by a hadron collider.
The Compact Muon Solenoid (CMS) is one of the two general-purpose experiments at the LHC. The main goals of the experiment are the study of the Higgs boson, indeed discovered in 2012 by ATLAS and CMS, and the search for new physics. One of the most promising fields is the search for Lepton Flavour Violating (LFV) processes, strongly suppressed in the SM but predicted by many Beyond Standard Model (BSM) theories at much higher rates.
The subject of this thesis is the search for the LFV decay $\tau^- \to \mu^-\mu^+\mu^-$[1], and it will focus on τ leptons originating from W bosons. The analysis is performed within the CMS experiment on Run-II data, which corresponds to an integrated luminosity of 146.9 fb^{-1}. The work presents the analysis of 2017 and 2018 data and completes the result obtained on 2016 statistics, recently published by CMS [5]. This was the first CMS result for the $\tau \to 3\mu$ search; I personally contributed to the analysis for the $W\to \tau\nu$ channel.
Indeed, the $\tau \to 3\mu$ process is studied within CMS also in the Heavy Flavour[2] (HF) channel to exploit the full potentiality of the experiment. The two channels have some advantages and some constraints. The sensitivity of the HF search is essentially limited by the low p_T of the τ leptons and by the large QCD background. By way of contrast, the factors limiting the sensitivity of the LFV search in $W \to \tau\nu$ decays mainly come from the much smaller W production cross section when compared to that of the Heavy Flavours in proton-proton collisions. Nevertheless, τ leptons from W are characterized

[1]The charge coonjugate decay $\tau^+ \to \mu^-\mu^+\mu^+$ is included in the analysis, as well. The decay will be more generally referred as $\tau \to 3\mu$ in the text.

[2]In the HF channel, D and B mesons are used as sources of τ leptons.

by clear signatures, i.e. the large missing energy, the good lepton isolation, the low background, and higher p_T values, which better suite the CMS triggers.
The 2016 study has allowed to identify the possible improvements of the analysis. In particular, a new trigger was studied and implemented to target specifically $\tau \to 3\mu$ processes from $W \to \tau\nu$ decays, taking advantage of the kinematic and topological characteristics of this channel. The new trigger version was included online in 2017.
The distinctive features of the W channel[3] are further exploited in the offline analysis of the collected events, which adopts multivariate techniques (MVA) to suppress the background contaminations. The signal yield upper limit is estimated from the distribution of the three-muon candidate invariant mass; the signal is fit with a Gaussian function in a signal region defined around the τ mass, while the background is extrapolated from the data sidebands and parametrized with a polynomial function.
The analysis has lead to an estimation of the expected upper limit (at 90% of confidence level) of 4.4×10^{-8} for the W channel. Combining the limit obtained in this thesis with the expected limit coming from the parallel analysis of HF decays and with the result on 2016 data, we obtained an expected global limit of 2.3×10^{-8} for the $\tau \to 3\mu$ decay, which is competitive with the the world-best result.
The analysis presented in this thesis was under internal approval at the time this thesis was written, so that only the expected upper limit, computed on blind data, is reported.

[3] In the W channel, W bosons are used as sources of τ leptons.

Sommario

Il *Large Hadron Collider* (LHC) è un collisore di protoni di circonferenza 27 km, costruito al CERN per studiare le interazioni delle particelle elementari alla scala di energia del TeV. A partire dal 2009, suo primo anno di funzionamento, l'energia a disposizione nel centro di massa dei due fasci di protoni che collidono è stata progressivamente aumentata dal valore iniziale di 0.9 TeV fino a raggiungere, nel 2015, 13 TeV. Questo valore rappresenta la più alta energia mai raggiunta da un collisore adronico.
CMS (*Compact Muon Solenoid*) è uno dei due esperimenti ad ampio spettro presenti ad LHC. Gli scopi principali di CMS sono lo studio del bosone di Higgs, scoperto nel 2012 da ATLAS e CMS, e la ricerca di evidenze di fisica oltre il Modello Standard (MS). In questa ottica, uno dei campi più promettenti è la ricerca di decadimenti caratterizzati da violazione del sapore leptonico (*Lepton Flavour Violation* - LFV), fortemente soppressi nel MS ma predetti con frazioni di decadimento più alte da alcune teorie oltre il MS (Beyond Standard Model - BSM). L'argomento di questa tesi è la ricerca del decadimento LFV $\tau \to 3\mu$, e si focalizza su leptoni tau provenienti da bosoni W. L'analisi è condotta nell'ambito dell'esperimento CMS sui dati raccolti durante Run-II, corrispondenti ad una luminosità integrata di 146.9 fb^{-1}. Questo lavoro completa il risultato ottenuto da CMS sui dati 2016, pubblicato recentemente [5]. Questo è stato il primo risultato ottenuto da CMS nella ricerca del decadimento $\tau \to 3\mu$; io ho personalmente contribuito all'analisi nel canale $W \to \tau\nu$.
A complemento dell'analisi nel canale di produzione W, a CMS è stata eseguita un'analisi utilizzando leptoni tau provenienti dai decadimenti di adroni pesanti, principalmente mesooni D_s e B (canale *Heavy Flavour* - HF). La loro combinazione permette di sfruttare appieno le potenzialità e la statistica di CMS. I due canali presentano dei vantaggi e degli svantaggi.La sensibilità del canale HF è essenzialmente limitata dal basso p_T dei leptoni τ e dal grande fondo QCD. Diversamente, i limiti principali dell'analisi nel canale $W \to \tau\nu$ sono dovuti alla piccola sezione d'urto di produzione dei bosoni W rispetto a quella dei quark pesanti nelle collisioni protone-protone. Tuttavia, questa tipologia di eventi risulta meno contaminata da fondi, grazie alla notevole Massa Trasversale Mancante (MET), al miglior isolamento dei leptoni e ad un più alto momento trasverso degli stessi, risultando

quindi più adatti alle selezioni del trigger.
L'analisi sui dati 2016 ha permesso di identificarne alcuni limiti e apportare migliorie. In particolare, è stata studiata ed implementata una nuova versione del trigger, online da luglio 2017. Questa nuova versione sfrutta maggiormente le caratteristiche cinematiche e topologiche dei decadimenti $\tau \to 3\mu$ nel canale di produzione W.
Queste caratteristiche distintive sono sfruttate appieno nell'analisi offline degli eventi raccolti grazie all'utilizzo di una tecnica di analisi multivariata per la reiezione degli eventi di fondo.
Il segnale e il suo limite superiore finale sono ricavati dagli istogrammi della massa invariante dei tre muoni ricostruiti; il segnale è interpolato con una funzione gaussiana centrata sul valore di massa del leptone tau, mentre il fondo è interpolato con una funzione polinomiale. L'analisi ha permesso una stima del limite superiore atteso (al 90% di livello di confidenza) pari a 4.4×10^{-8} per il canale W. Combinando il limite ottenuto in questa tesi con quello del canale comoplementare HF e con il risultato ottenuto sui dati 2016, si ottiene un limite preliminare di 2.3×10^{-8}, che risulta competitivo con il miglior limite mondiale.
L'analisi presentata è in fase di revisione interna nel momento in cui questa tesi viene scritta, e il risultato può essere citato solo in termini di limite superiore atteso, calcolato su dati blind.

Chapter 1

The Standard Model

This chapter gives a brief description of the Standard Model of particle interactions. First, the general properties of the model are given in terms of gauge theory. Then, the expected rate of the $\tau \to 3\mu$ process is given as predicted by the Standard model and for some new physics models (Sec. 3). In Sec. 1.5 the state of the art of the search for the $\tau \to 3\mu$ decay is presented. It includes the first CMS result obtained on the partial statistics corresponding to the 2016 only dataset. The analysis combines the W$\to \tau\nu$ and HF channels: I performed the W$\to \tau\nu$ analysis which is part of my PhD work.

1.1 Overview

The interactions between elementary particles are described by the gauge theory known as Standard Model (SM) [6, 7]. Formulated in the second half of the 20^{th} century by S. L. Glashow, S. Weinberg and A. Salam as a consequence of the experimental evidences collected in that period [8], the SM has shown its validity during the last decades of experiments. The discovery of W and Z bosons at the Super Proton Synchrotron (SPS) in 1983 and the consequent precise measurements of the electroweak associated interaction at the Large Electron-Positron collider (LEP) have increased the confidence in the model throughout the years.
The SM predictions have been tested by many experiments worldwide (such as LEP and TEVATRON) over a wide range of energies, providing an incredibly successful description of fundamental interactions. The core of the model, the mechanism which allows for the description of vector bosons and fermions in terms of massive fields, requires an additional scalar boson, known as Higgs particle. The validity of this mechanism was confirmed in 2012 with the observation of a Higgs-like boson by the ATLAS [9] and CMS [10] collaborations.

In parallel to the precise measurements of the SM predictions, one of its test fields is the search for the violation of the conservation of the leptonic number in charged-lepton decays (Charged Lepton Flavour Violation - LFV), which is allowed, taking into account the non-zero neutrino masses, at the lowest rates. Although some Beyond Standard Model (BSM) theories predict the existence of LFV currents with detectable branching ratios, no evidence of such processes has been found so far. The detection of LFV processes would imply the existence of Beyond Standard Model physics.

1.2 Particles and interactions

The constituents of matter are spin 1/2 particles called fermions. Fermions are divided into two categories, based on the different properties observed in nature.
Leptons are electroweak interacting fermions of unitary charge. Three different leptons are known up to today: the electron (e), historically associated to the electric properties of matter, the muon (μ), observed for the first time in 1936 by C. D. Anderson and S. Neddermeyer [11], and the tau (τ), discovered in 1977 by at the SLAC-LBL group [12]. A massless neutral fermion is associated to each lepton, the neutrino (ν). Together with the corresponding lepton, they form three different leptonic families. In SM processes, each lepton carries a number, called *leptonic number*.
Quarks are strong and electroweak interacting fermions of fractional electric charge, known to be the elementary constituents of nucleons. There are six quark flavours, subdivided into three families: up (u) and down (d), charm (c) and strange (s), top (t) and bottom (b). Each flavour can appear in three different colour states, red, blue or green. Quarks do not appear free, but form bounded and colourless states called hadrons. Commonly observed hadrons are mesons, a bound state of a quark and an antiquark, and baryons, a bound state of three quarks. More exotic bound states, such as tetraquark and pentaquarks, are predicted by the Gell-Mann quark model.

The Standard Model describes three different types of interactions: the weak, electromagnetic and strong interaction. Gravity is not described and its strength is negligible at experimentally achievable energies, if compared to the other interactions.

Figure 1.1 summarises the elementary particles described by the SM.

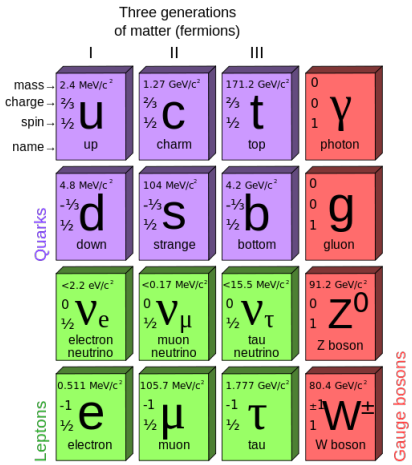

Figure 1.1: Elementary particles described by the Standard Model and their properties

1.2.1 A brief mathematical description

Each fermion is represented by a four component Dirac spinor ψ with mass m, that satisfies the equation of motion

$$(i\gamma^\mu \partial_\mu - m)\psi = 0 \tag{1.1}$$

generated by the free Lagrangian

$$\mathscr{L} = i\bar{\psi}\gamma^\mu \partial_\mu \psi - m\bar{\psi}\psi \tag{1.2}$$

The letter $\bar{\psi}$ is used to indicate the Dirac conjugate of ψ, $\bar{\psi} = \psi^\dagger \gamma^0$, while γ's are the Dirac matrices, defined by the equation

$$\{\gamma^\mu, \gamma^\nu\} = 2\eta^{\mu\nu} \tag{1.3}$$

where η is the Minkowsky metric.

The Dirac field ψ can be written in terms of two Weyl spinors, projecting it on its left and right chiaral components.

$$\begin{gathered} \psi_L = P_L\psi, \qquad \psi_R = P_R\psi \\ \psi = \psi_L + \psi_R = \begin{pmatrix} \chi - \phi \\ \phi - \chi \end{pmatrix} \end{gathered} \tag{1.4}$$

where χ and ϕ are the particle and antiparticle components of ψ. The left and right projectors are defined as

$$P_L = \frac{1-\gamma^5}{2}, \qquad P_R = \frac{1+\gamma^5}{2} \tag{1.5}$$

Despite chirality being a mathematical property of fields, it is related to the particle ellicity by the equation

$$\begin{aligned} \chi_L &= \chi^- + O(m/E)\chi^+ \\ \phi_L &= \phi^+ + O(m/E)\phi^- \end{aligned} \tag{1.6}$$

while opposite relations hold for right-handed particles and antiparticles.

Weak interactions intrinsically violates parity, as discovered in 1956 by Mme Wu and

Goldhaber [13] experiments, coupling only left handed fermions to charged weak bosons. For this reason, fermions are divided into left-handed $SU(2)_I$ doublets and right-handed $SU(2)_I$ singlets.

$$\begin{aligned} f_L &= \begin{pmatrix} e_L \\ \nu_{eL} \end{pmatrix}, \quad \begin{pmatrix} \mu_L \\ \nu_{\mu L} \end{pmatrix}, \quad \begin{pmatrix} \tau_L \\ \nu_{\tau L} \end{pmatrix}, \quad \begin{pmatrix} u_L \\ d_L \end{pmatrix} \\ f_R &= e_R, \quad \mu_R, \quad \tau_R, \quad u_R, \quad d_R \end{aligned} \tag{1.7}$$

The right-handed neutrino is not included in the Standard Model, since its coupling to electroweak bosons is null.

Vector bosons are in turn described by vectorial fields, and solve the equation of motion

$$(\Box + m^2)A^\mu = 0 \tag{1.8}$$

generated by the Lagrangian

$$\mathscr{L} = -\frac{1}{4}F^{\mu\nu}F_{\mu\nu} + \frac{1}{2}m^2 A_\mu A^\mu \tag{1.9}$$

where F is the kinetic tensor associated to the field A

$$F_{\mu\nu} = \partial_\mu A_\nu - \partial_\nu A_\mu - i[A_\mu, A_\nu] \tag{1.10}$$

1.3 The Yang-Mills electroweak theory

As Maxwell unification of electric and magnetic forces arises from a geometrical request, that is the invariance of the electromagnetic Lagrangian under a U(1) local transformation, it is possible to construct new interaction theories starting from a more generic gauge symmetry. As stated by the Noether theorem, new conserved charges and forces arise from this request. Generic SU(N) gauge theories are known as Yang-Mills theories [6].

The invariance under gauge transformations is expressed as invariance under field transformation of the from $\psi \to e^{i\varepsilon}\psi$, where the parameters ε is a function of the space-time coordinate, making the transformation local, and can be expressed as linear combination of the gauge group generators T as $\varepsilon = \alpha_a T^a$.

The necessity of having a local, gauge-invariant theory introduces a new derivative operator $D_\mu = \partial_\mu - igT_aA^a_\mu$ and a new vectorial field, denoted by A, together with a parameter g.

Taking into consideration the spinorial Lagrangian defined in Eq. 1.2, substituting the trivial derivative with the covariant derivative D, one can obtain

$$\mathscr{L} = i\bar{\psi}\gamma^\mu\partial_\mu\psi - m\bar{\psi}\psi - ig\bar{\psi}\gamma_\mu T^a A^\mu_a\psi \tag{1.11}$$

The interaction between fermions arises from the introduction of the new derivative operator, as a consequence of the local gauge-invariant nature of the theory. No mass terms for bosons are allowed in the Lagrangian, since they would break the SU(N) symmetry.

1.3.1 The electroweak interaction

The SM electroweak (EW) interaction is described by the $SU(2)_I \times U(1)_Y$ symmetry group. In this case, one boson for $U(1)_Y$, B, and three bosons for $SU(2)_I$, W's, are present; the transformation matrix U and the covariant derivative can be written as

$$U = exp\{i\beta(x)\frac{Y}{2} + i\alpha_i(x)\frac{\sigma^i}{2}\} \tag{1.12}$$

$$D_\mu = \partial_\mu - ig'\frac{Y}{2}B_\mu - ig\frac{\sigma_i}{2}W^i_\mu \tag{1.13}$$

where Y indicates the weak hypercharge and $I_i = \sigma_i/2$ are the weak isospin matrices. The two quantities are related to the electric charge by the Gell-Mann-Nishijima formula

$Y = 2(Q - I_3)$.

The electroweak interaction description relies on the additional request of non conservation of parity in the weak sector. For this reason, a distinction is made between left-handed and right-handed fermions: left-handed fermions appear as SU(2) doublets and right-handed fermions appear as SU(2) singlets. Under these assumptions, considering for simplicity only one lepton field as defined in Eq. 1.7, the SU(2) $\times$ U(1) Lagrangian can be written as

$$\begin{aligned} \mathscr{L} = \; & i\bar{f}_L\gamma_\mu\partial^\mu f_L + i\bar{l}_R\gamma_\mu\partial^\mu l_R - \frac{1}{4}B_{\mu\nu}B^{\mu\nu} - \frac{1}{4}W^i_{\mu\nu}W_i^{\mu\nu} + \\ & i\bar{f}_L\gamma^\mu(-ig\frac{\sigma_i}{2}W^i_\mu - ig'\frac{Y}{2}B_\mu)f_L - i\bar{l}_R\gamma^\mu(-ig\frac{Y}{2}B_\mu)l_R \end{aligned} \tag{1.14}$$

The last term is the interaction part of the Lagrangian. As already stated, mass terms are not allowed for vector bosons, since they would break the gauge symmetry. For the same reason, taking into consideration that left and right-handed spinors transform differently under $SU(2)_I$, fermionic mass terms cannot be naively inserted in the Lagrangian.

The interaction term can be rewritten in a more compact way as

$$\mathscr{L}_I = -gJ^\mu_i W^i_\mu - g'J^\mu_Y B_\mu \tag{1.15}$$

where the J vectors are the Noether currents associated to each generator

$$J^\mu_i = \bar{f}_L\gamma^\mu\tfrac{1}{2}\sigma_i f_L, \qquad J^\mu_Y = -\bar{l}_R\gamma^\mu\tfrac{1}{2}Y l_R - \bar{f}_L\gamma^\mu\tfrac{1}{2}Y f_L \tag{1.16}$$

The B and W bosons are not the physical fields: an orthogonal transformation, parametrized by the Weinberg angle θ_W, is required to define the observed bosons

$$\begin{gathered} W^\pm_\mu = \tfrac{1}{\sqrt{2}}(W^1_{mu} \mp W^2_\mu) \\ \begin{pmatrix} A_\mu \\ Z_\mu \end{pmatrix} = \begin{pmatrix} \cos\theta_W & \sin\theta_W \\ -\sin\theta_W & \cos\theta_W \end{pmatrix} \begin{pmatrix} B_\mu \\ W^3_\mu \end{pmatrix} \end{gathered} \tag{1.17}$$

while currents are redefined as

$$J^{\mu\pm} = 2(J^\mu_1 \pm J^\mu_2), \qquad J_{EM} = e(J^\mu_Y + J^\mu_3) \tag{1.18}$$

With this redefinition of the vector field, the interaction Lagrangian becomes

$$\begin{aligned}\mathscr{L}_I = \quad & -\frac{g}{2\sqrt{2}}(J^{\mu+}W_\mu^- + J^{\mu-}W_\mu^+) \\ & + J_3^\mu(g'\sin\theta_W - g\cos\theta_W)Z_\mu \\ & - J_3^\mu(g\sin\theta_W - g'\cos\theta_W)A_\mu \\ & - J_{EM}^\mu(-\frac{g}{e}\sin\theta_W Z_\mu + \frac{g'}{e}\cos\theta_W A_\mu)\end{aligned} \tag{1.19}$$

The final equation is derived requiring the object A to be the electromagnetic field, that is requiring its coupling to the weak current J_3 to vanish and the coupling to the EM current J_{EM} to be equal to -e. This request leads to

$$e = g\sin\theta_W = g'\cos\theta_W \tag{1.20}$$

Under this conditions, one can write the final result

$$\begin{aligned}\mathscr{L}_I = \quad & -J_{EM}^\mu A_\mu \\ & -\frac{g}{2\sqrt{2}}(J^{\mu+}W_\mu^- + J^{\mu-}W_\mu^+) \\ & -\frac{e}{\sin\theta_W\cos\theta_W}(J_3^\mu - \frac{\sin^2\theta_W}{e}J_{EM}^\mu)Z_\mu\end{aligned} \tag{1.21}$$

Writing the definition of Eq. 1.16 explicitly in the Lagrangian of Eq. 1.21 and letting the index j run over the fermion families accordingly, one can obtain the charged and neutral coupling of the SM electroweak theory

$$\begin{aligned}\mathscr{L}^{cc} &= -\tfrac{g}{2\sqrt{2}}\textstyle\sum_j\left[W_\mu^+\bar{q}_{u_j}\gamma^\mu(1-\gamma^5)q_{d_j} + \bar{\nu}_{l_j}\gamma^\mu(1-\gamma^5)l_j + h.c.\right] \\ \mathscr{L}^{z} &= -\tfrac{e}{\sin\theta_W\cos\theta_W}\textstyle\sum_j Z_\mu\bar{f}_j\gamma^\mu\left(gI_3\cos\theta_W - g'Y\sin\theta_W\right)f_j \\ \mathscr{L}^{em} &= -e\textstyle\sum_j A_\mu\bar{f}_jQ_j\gamma^\mu f_j\end{aligned} \tag{1.22}$$

where q_u and q_d indicate a generic up and down quark, l indicates a generic lepton and f indicates a generic fermion.
Figures 1.2 and 1.3 show the vertices described in Eq. 1.22.

The equations 1.22 describe the coupling of fermions to electroweak bosons. No mixing between quark nor lepton families is present at the tree level.

In addition to Eq. 1.22, one can obtain gauge bosons self-interaction terms introducing the gauge invariant term $B_{\mu\nu}B^{\mu\nu} + W^i_{\mu\nu}W_i^{\mu\nu}$ to the Lagrangian, thus obtaining

$$\begin{aligned}
\mathscr{L}_{si} = \;& ie\cot\theta_W \left(W^+_{\mu\nu}W^{\mu-}Z^\nu - W^-_{\mu\nu}W^{\mu+}Z^\nu + Z_{\mu\nu}W^{\mu+}W^{\nu-}\right) \\
& + ie\left(W^+_{\mu\nu}W^{\mu-}A^\nu - W^-_{\mu\nu}W^{\mu+}A^\nu + A_{\mu\nu}W^{\mu+}W^{\nu-}\right) \\
& - \frac{e}{2\sin\theta_W\cos\theta_W}\left((W^+_\mu W^{\mu-})^2 - W^+_\mu W^{\mu+}W^-_\nu W^{\nu-}\right) \\
& - e^2\cot^2\theta_W\left(W^+_\mu W^{\mu-}Z_\nu Z^\nu - W^+_\mu W^{\nu-}Z_\mu Z^\nu\right)
\end{aligned} \tag{1.23}$$

In figure 1.4, the self-interaction between gauge bosons is summarized.

The $SU(2)_I \times U(1)_Y$ Lagrangian was first introduced by Glashow in 1961. It is formulated under the assumption of a local gauge-invariant and parity violating theory. The first part of Eq. 1.21 represents the electromagnetic interaction, the second the weak charged interaction (W bosons), while the last term represents the neutral weak interaction (Z boson).

Following the same principle, one can define a non-abelian gauge theory that describes the strong force. This theory, known as quantum chromodynamics (QCD), is based on the $SU(3)_C$ gauge symmetry and predicts the existence of eight vector fields, called

gluons.

$$\mathscr{L}_{QCD} = -\frac{1}{4}G^a_{\mu\nu}G^{\mu\nu}_a + \sum_j \bar{q}^\alpha_j (i\gamma^\mu - m_f) q^\alpha$$

$$+ g_s G^a_\mu \sum_j \bar{q}^\alpha_j \gamma^\mu \frac{1}{2}(\lambda^a)_{\alpha\beta}\, q^\beta_j \tag{1.24}$$

$$-\frac{1}{2}f^{abc}G^a_{\mu\nu}G^b_\mu G^c_\nu - \frac{1}{4}g_s^2 f^{abc} f_{ade} G^b_\mu G^c_\nu G^\mu_d G^\nu_e$$

The Lagrangian in Eq. 1.24 describes the colour interaction between quarks and gluons. The first line is the kinetic term, the second line is the colour interaction term (λ's are the Gell-Mann colour matrices) and the third line describe the gluon field self interaction, consequence of the non-abelian nature of the strong force. The parameter f^{abc} is the SU(3) structure constant $[\lambda^a, \lambda^b] = 2if^{abc}\lambda^c$. The interaction vertices described by Eq. 1.24 are shown in Fig. 1.5.

Figure 1.2: Electroweak charged currents expected by the Standard Model

Figure 1.3: Electroweak neutral currents expected by the Standard Model. The weak neutral coupling is usually expressed in terms of vectorial and axial coefficients
$v_f = I_3^f(1-4|Q_f|\sin^2\theta_W)$, $a_f = I_3^f$

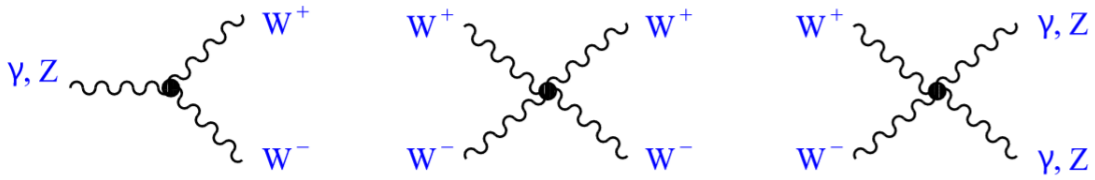

Figure 1.4: Self interaction of electroweak gauge bosons

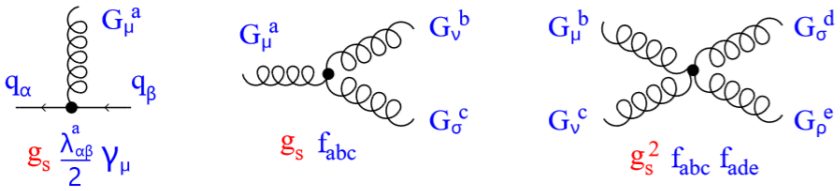

Figure 1.5: QCD vertices expected by the Standard Model

1.3.2 The Higgs mechanism

The Standard Model of electroweak interactions cannot describe fermions and bosons as massive field using a trivial approach, since the introduced mass terms would break the local gauge symmetry of the model. A different mechanism is needed in order to describe what is actually observed in nature, that is a non zero mass value for leptons and for W and Z bosons. This mechanism is called the Spontaneous Symmetry Breaking (SSB) Higgs mechanism.

In order to derive fermionic and bosonic mass terms, an additional scalar field is needed. This field can be expressed in the most generic way as a complex SU(2) doublet

$$\phi = \begin{pmatrix} \phi_1 + i\phi_2 \\ \phi_3 + i\phi_4 \end{pmatrix} \tag{1.25}$$

Its Lagrangian would then be

$$\mathscr{L}_{Higgs} = (D^\mu \phi)^\dagger D_\mu \phi - V(\phi, \phi^\dagger) \tag{1.26}$$

where V is the Higgs potential, $V = \mu^2 \phi^\dagger \phi + \lambda (\phi^\dagger \phi)^2$

For $\mu^2 < 0$, the Higgs potential shows a degenerate, gauge invariant set of minima, given by the relation

$$|\phi_0|^2 = -\frac{\mu^2}{2\lambda} := \frac{1}{2} v^2 \tag{1.27}$$

with v being the vacuum expectation value (VEV) of the Higgs field.

A choice of a particular minimum would break the gauge symmetry above. The theory is then said to be spontaneously broken. The simplest choice of vacuum is given by

$$\phi_0 = \frac{1}{\sqrt{2}} \begin{pmatrix} 0 \\ v \end{pmatrix} \tag{1.28}$$

The Higgs filed can be expressed as a perturbation around its minimum

$$\phi(x) = \frac{1}{\sqrt{2}} \begin{pmatrix} \theta_1(x) + i\theta_2(x) \\ v + H(x) - i\theta_3(x) \end{pmatrix} \approx \frac{1}{\sqrt{2}} e^{\frac{2\theta^i \tau^i}{2v}} \begin{pmatrix} 0 \\ v + H(x) \end{pmatrix} \tag{1.29}$$

The non-physical fields θ can be removed exploiting the SU(2) invariance of the Lagrangian, leaving only the scalar H field (unitary gauge). The remaining field is called Higgs field.

$$\phi(x) = \begin{pmatrix} 0 \\ v + H(x) \end{pmatrix} \tag{1.30}$$

It is worth noticing that, since the Higgs field is neutral, a residual symmetry under $U(1)_Q$ rotation is still present. This remnant symmetry will guarantee a zero mass value for the photon.

Substituting the result in Eq. 1.30, using the covariant derivative definition of Eq. 1.13 and the rotations defined in Eq. 1.17, the final result can be obtained

$$\begin{aligned} \mathscr{L}_{Higgs} = \quad & \left[\frac{1}{2} \partial_\mu H \partial^\mu - v^2 \lambda H^2 \right] \\ & + \left[\frac{1}{2} \frac{v^2 g^2}{4} W_\mu^- W^{-\mu} + \frac{1}{2} \frac{v^2 g^2}{4} W_\mu^+ W^{+\mu} \right] \\ & + \left[\frac{1}{2} \frac{v^2 (g^2 + g'^2)}{4} Z_\mu Z^\mu \right] \end{aligned} \tag{1.31}$$

The first line of Eq. 1.31 shows the Higgs boson kinematic term and its mass, while

the second and third lines show the mass terms for the W and Z bosons.

$$\begin{aligned} m_W &= \tfrac{1}{2} v g \\ m_Z &= \tfrac{1}{2} v \sqrt{g^2 + g'^2} \\ m_H &= v\sqrt{2\lambda} \end{aligned} \tag{1.32}$$

Considering higher orders of the Higgs potential, the interaction between gauge bosons and the Higgs boson is generated

$$\mathscr{L}_{gauge} = \left(1 + \frac{2}{v}H + \frac{H^2}{v^2}\right)\left(M_W^2 W_\mu^+ W^{\nu -} + \frac{1}{2} M_Z^2 Z_\mu Z^\nu\right) \tag{1.33}$$

Equation 1.33 is summarised in Fig. 1.6.
This procedure allows the electroweak theory to account for massive boson fields, while leaving the spinorial fields still massless. In order to explain the massive nature of fermions, an additional term must be considered. This term, called Yukawa Lagrangian, introduces a new coupling between the scalar field of Eq. 1.30 and the fermions, thus generating the fermion masses.

$$\mathscr{L}_{Yukawa} = -[c_1 \bar{q} \phi d_R - c_2 \bar{q} \phi^c u_R + \bar{l}_L \phi ł_R + h.c.] \tag{1.34}$$

where ϕ^c is the $\mathscr{C}$-conjugate of the field ψ.

In the unitary gauge, the Yukawa coupling takes the form

$$\begin{aligned} \mathscr{L}_{Yukawa} &= -\frac{1}{\sqrt{2}}(v+H)(c_1 \bar{d}d + c_2 \bar{u}u + c_3 \bar{l}l_R) \\ &= -(1 + \frac{H}{v})(m_d \bar{d}d + m_u \bar{u}u + m_l \bar{l}l) \end{aligned} \tag{1.35}$$

Introducing the Yukawa coupling, new mass terms for leptons are generated. Furthermore, a new coupling between leptons and the Higgs field has emerged.

It is possible to extend the Higgs mechanism to a three family model, obtaining the

complete Yukawa coupling

$$\begin{aligned}\mathscr{L}_{Yukawa} &= -\sum_{jk}\left[c^{(d)}_{jk}\bar{q}^j_L\phi d^k_R + c^{(u)}_{jk}\bar{q}^j_L\phi^c u^k_R + c^{(l)}_{jk}\bar{l}^j_L\phi l^k_R + h.c.\right] \\ &= -\left(1+\frac{H}{v}\right)\left(\bar{d}_L M_d d_R + \bar{u}_L M_u u_R + \bar{l}_L M_l l_R + h.c.\right)\end{aligned} \tag{1.36}$$

The mass matrices in Eq. 1.36 are not diagonal. In order to obtain the physical fields, a rotation is needed

$$\begin{aligned} u_L &\to V^u_L u_L \quad u_R \to V^u_R u_R \\ d_L &\to V^d_L d_L \quad d_R \to V^d_R d_R \\ l_L &\to V^l_L l_L \quad\quad l_R \to V^l_R l_R \end{aligned} \tag{1.37}$$

While leaving the neutral currents unchanged, this rotation introduces a mixing in the quark section of the electroweak charged currents, allowing transitions between quark families. This phenomenon, known as Cabibbo-Kobayashi-Maskawa mechanism, is described by the CKM matrix and it's partially responsible of the CP violation observed in nature.
Differently from quarks, neutrinos are massless fields in the minimal SM description. This allows to choose freely the rotation matrix associated to the neutrino. Choosing $V_{\nu_l} = V_l$, no lepton family rotation is introduced and the lepton number is conserved by both neutral and charged currents [14].
This mechanism, postulated by P. Higgs, F. Englert and R. Brute in 1964, found its validity in 2012 when the Higgs boson was observed for the first time by the ATLAS and CMS collaborations.

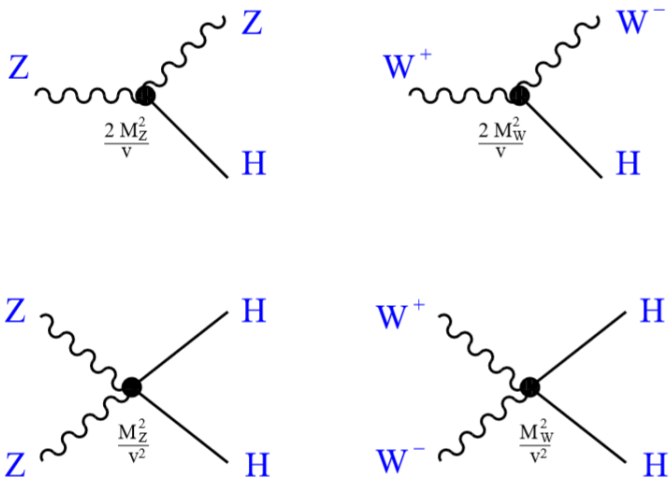

Figure 1.6: Higgs coupling to the electroweak bosons

1.4 Standard model and new physics predictions of lepton flavour violating decays

Charged Lepton Flavour Violation (LFV) is not allowed by the SM with massless neutrinos. However, neutrinos have been proved to have a finite mass, despite very small [15]; this property allows for SM LFV processes like those shown in Fig. 1.7 to occur.
Nonetheless, this kind of processes are expected to be suppressed by a factor $x_i = m_{\nu_i}/M_W$ (being m_{ν_i} the mass of the neutrino mass-eigenstate i, and M_W the mass of the W boson, 80 GeV). In fact, the amplitudes of the diagrams in 1.7 take the form [1]:

$$i\mathscr{A}_\gamma = \frac{\alpha G_F}{\sqrt{2}\pi}(\bar{l}\gamma^\mu P_L L)(\bar{l'}\gamma_\mu l')\sum_i U_{li}U^*_{Li}x_i \tag{1.38}$$

$$i\mathscr{A}_Z = \frac{\alpha G_F}{\sqrt{2}\pi}\sum_i U_{li}U^*_{Li}x_i(3+\log x_i)\times \tag{1.39}$$
$$[(\bar{l}\gamma^\mu P_L L)(\bar{l'}\gamma_\mu l') - \frac{1}{2\sin\theta_W}(\bar{l}\gamma^\mu P_L L)(\bar{l'}\gamma^\mu P_L l')$$

$$i\mathscr{A}_{box} = \frac{\alpha G_F}{\sqrt{2}\pi\sin\theta_W{}^2}(\bar{l}\gamma^\mu P_L L)(\bar{l'}\gamma_\mu P_L l')\sum_i U_{li}U^*_{Li}x_i(1+\log x_i) \tag{1.40}$$

where α is the fine structure constant, G_F is the Fermi constant, θ_W is the Weinberg angle, and U is the PMNS (Pontecorvo-Maki-Nakagawa-Sakata) matrix [16], defined as the rotation matrix which maps the neutrino mass-eigenstates ν_i (i = 1, 2, 3) into the observed flavour states:

$$\begin{bmatrix}\nu_e\\ \nu_\mu\\ \nu_\tau\end{bmatrix} = U\times\begin{bmatrix}\nu_1\\ \nu_2\\ \nu_3\end{bmatrix} \tag{1.41}$$

The matrix U can be parametrized in terms of three rotation angles (θ_{12}, θ_{13}, θ_{23}) and one complex phase (δ_{CP}) as follows:

$$U = \begin{bmatrix} c_{12}c_{13} & s_{12}c_{13} & s_{13}e^{-i\delta_{CP}}\\ -s_{12}c_{23}-c_{12}s_{13}s_{23}e^{i\delta_{CP}} & c_{12}c_{23}-s_{12}s_{13}s_{23}e^{i\delta_{CP}} & c_{13}s_{23}\\ s_{12}s_{23}-c_{12}s_{13}c_{23}e^{i\delta_{CP}} & -c_{12}s_{23}-s_{12}s_{13}c_{23}e^{i\delta_{CP}} & c_{13}c_{23}\end{bmatrix} \tag{1.42}$$

where s_{ij} indicates $\sin\theta_{ij}$ and c_{ij} indicates $\cos\theta_{ij}$.
The formulae in Eq. 1.40 are valid for the decay of heavy leptons ($L = \mu, \tau$) into lighter leptons ($l = e, \mu$). Two different approximations exist which predict the LFV branching fractions in the SM. The first is called zero-momentum-limit (ZML) [17] and assumes vanishing masses and momenta for external particles. The second is called physical limit

(PL) and keeps full dependence of external momenta in the computation [18].
In the ZML, one can obtain [1]:

$$\frac{\Gamma(L \to lll)}{\Gamma_0} = \frac{3\alpha^2}{16\pi^2} \left| \sum_{i=1}^{3} U_{li} U_{Li}^* \frac{\Delta m_{i1}^2}{M_W^2} \log \frac{\Delta m_{i1}^2}{M_W^2}^2 \right| \tag{1.43}$$

whereas, in the PL [18], one can obtain [1]:

$$\frac{\Gamma(L \to lll)}{\Gamma_0} = \frac{3\alpha^2}{16\pi^2} \left| \sum_{i=1}^{3} U_{li} U_{Li}^* \frac{\Delta m_{i1}^2}{M_W^2} \log \frac{\Delta m_{i1}^2}{M_W^2} \right|^2 \times$$
$$[\log x_L{}^2 + 2\log x_L - \frac{1}{6}\log x_l + \frac{19}{18} + \frac{17}{18}\pi^2 - \frac{1}{\sin\theta_W{}^2}(\log x_L + \frac{11}{12}) + \frac{3}{8\sin\theta_W{}^4}] \tag{1.44}$$

where $\Gamma_0 = \frac{G_F^2 m_L^5}{192\pi^3}$, $x_L = m_L^2/M_W^2$, and $x_l = m_l^2/M_W^2$. Equations 1.43 and 1.44 are obtained in the limit $m_1 \to 0$ and assume the normal neutrino mass hierarchy ($m_1 < m_2 < m_3$). The inverted hierarchy formula is obtained with the change $1 \leftrightarrow 2$.
Table 1.1 shows the predicted values of the $\tau \to 3\mu$ and other LFV processes branching fractions under the two approximations.

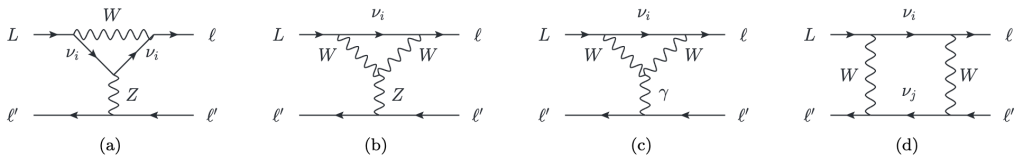

Figure 1.7: One loop diagrams contributing to the charged LFV decay $L \to lll$ in the unitary gauge: the Z penguin (a, b), the photon penguin (c) and the box (d) [1].

Table 1.1: Branching ratios of some charged LFV process predicted by the ZML and PL for normal (inverted) ordering of neutrino masses [1].

	ZML	PL
$\tau \to \mu\mu\mu$	2.0 (2.0) $\times 10^{-53}$	5.8 (5.8) $\times 10^{-55}$
$\mu \to eee$	4.1 (6.1) $\times 10^{-54}$	2.9 (4.6) $\times 10^{-55}$
$\tau \to \mu ee$	1.3 (1.3) $\times 10^{-53}$	3.8 (3.8) $\times 10^{-55}$
$\tau \to eee$	1.1 (0.6) $\times 10^{-54}$	3.3 (1.9) $\times 10^{-56}$
$\tau \to e\mu\mu$	7.6 (4.1) $\times 10^{-55}$	2.1 (1.2) $\times 10^{-56}$

The values of the $\tau \to 3\mu$ branching fraction predicted by the SM are, of course, far beyond the reach of experiments, which nowadays are able to achieve a sensitivity of the

order of 10^{-8} (see Sec. 1.5). However, some models Beyond the SM (BSM) exists which predict values of the LFV branching ratios of the order of 10^{-9} [19] [20] [2], much higher than the SM rates and not far from the experimental sensitivity.
One model of particular interest is the Patit-Salam (PS^3) model described in [2]; it has the merit of connecting the hints of $b \to s$ and $b \to c$ anomalies observed by LHCb and BaBar [21, 22, 23, 24] to the hierarchy of quark and lepton masses and to the violation of the leptonic numbers. As already hypothesized in other works [25, 26, 27], the mediator responsible for the B anomalies is a leptoquark field, which acquires mass with the dynamical breaking of the flavour symmetry present in the model. Two other fields responsible for the flavour-changing processes gain mass with the same symmetry breaking: a colour octet (a *coloron*) and a Z' boson. All these fields take masses in the TeV range [2]. The $\tau \to 3\mu$ process is mediated by the Z' boson, and its branching fraction is:

$$\mathscr{B}(\tau \to 3\mu) \approx C_{Z'}^2 s_\tau^2 [28(s_\tau^2 + \varepsilon_l)^2 - 38\frac{{g_1}^2}{g_4}(s_\tau^2 + \varepsilon_l - 2\frac{{g_1}^2}{g_4})] \tag{1.45}$$

where $C_{Z'}$ is the coupling constant to the Z' boson, s_τ is a mixing parameter, g_1 and g_4 are gauge couplings, and ε_l is a parameter controlling the breaking of the flavour symmetry. For typical values for these parameters [2], the branching fraction of the $\tau \to 3\mu$ process assumes a value around 10^{-9}, which approaches the current experimental sensitivity. In addition to $\tau \to 3\mu$ decays, also $\mu \to 3e$, $\mu \to e\gamma$ and $K_L \to \mu e$ decays are predicted to be close to the current exclusion limits [28, 29, 30].

As already mentioned, B anomalies and different LFV processes (such as $\tau \to 3\mu$ and $\tau \to \mu\gamma$) are connected by the same SSB mechanism. On the one hand, these channels provide an excellent test fot the SM on their own, allowing for a direct search of new physics events. On the other, as a distinctive signature, this PS^3 model predicts correlations between its observables (see for example Fig. 1.8), and offers a testing ground for the study of its validity, were these processes to be observed.

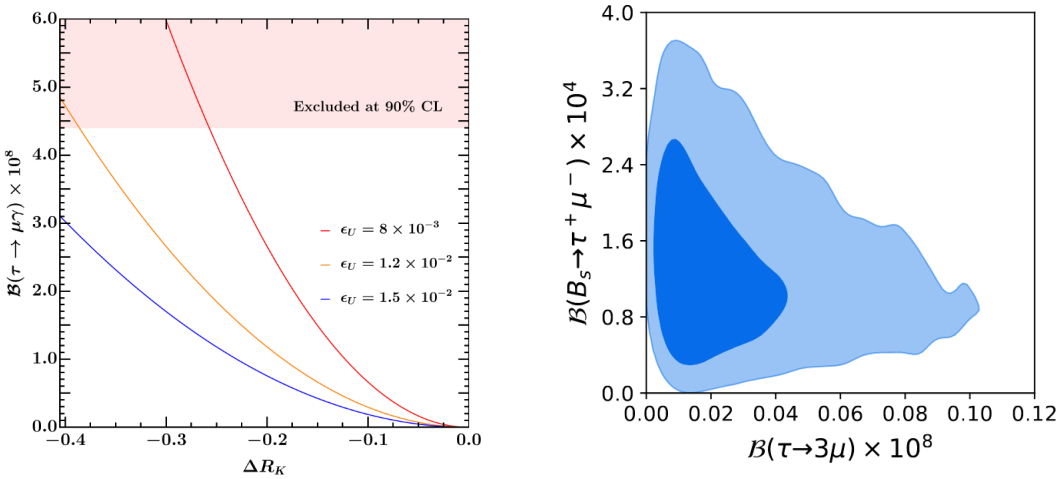

Figure 1.8: Left: $\mathcal{B}(\tau \to \mu\gamma)$ as function of the NP shift in R_K ($R_K = \frac{\mathcal{B}(B^+ \to K^+ \mu\mu)}{\mathcal{B}(B^+ \to K^+ ee)}$) for different values of the model parameter ϵ_U. Right: correlation between the LFV rates $\tau \to 3\mu$ and $B_s \to \tau^+\mu^-$. The blue areas show the 68% and 95% credible intervals estimated by the PS^3 model [2]

1.5 The experimental scenario for the $\tau \to 3\mu$ searches

As explained in the previous sections, Lepton Flavour Violating (LFV) decays of charged leptons are expected to have a negligible probability, if only SM processes are considered. Indeed, even taking into account the non zero values of neutrino masses, such processes are allowed only at undetectable rates. The $\tau \to 3\mu$ yield, vanishingly small in the Standard Model, is predicted at a rate of 10^{-10}–10^{-8} in various SM extensions. The detection of LFV processes above the lowest rates foreseen by the SM would then be a hint of the presence of new physics.

Different experiments have adopted different strategies in the investigation of this process. B-factories, like Belle and BaBar, can exploit the high cross section of τ leptons produced at the $\Upsilon(4s)$ resonance. The LHCb experiment has, instead, performed an inclusive analysis on τ leptons coming from Heavy Flavours Decays.This approach alone cannot be pursued at ATLAS and CMS, where the high QCD contamination and the low p_T of the τ leptons reduce the efficiency of signal selection. Nonetheless, in these experiments tau leptons from W and Z bosons, although less copious, can be more conveniently triggered, due to the large Missing Transverse Energy (MET) and the good lepton isolation which characterises the decay.
The world best limit has been set by the Belle collaboration, and is 2.1×10^{-8} at 90% of Confidence Level (CL) [3].

1.5.1 Belle and BaBar

Up today, the best experimental limit on the $\tau \to 3\mu$ process has been set by the Belle collaboration, using an integrated luminosity of 782 fb^{-1} [3]. The data were collected at the e^+e^- asymmetric collider KEKB, with a CM energy of 10.48 GeV ($\Upsilon(4S)$ resonance) and a maximum instantaneous luminosity of about 2×10^{34} s^{-1} cm^2. With a cross section of 0.9 nb for the $\tau^+\tau^-$ production, B-factories are an excellent source of τ leptons, allowing to reach a high sensitivity for rare τ decay experiments [31].

Signal events containing two τ are selected, requiring one lepton to decay into a SM leptonic final state (tag side) and the other into a LFV final state (signal side). Each event is divided into two hemispheres, one containing the signal and one containing the tag, in order to exploit the missing energy expected in the tag side and reduce the background.

Leptons are identified using likelihood ratios calculated from the response of various subdetectors, where the signal selection efficiency is optimized using Montecarlo (MC)

samples. After the selection, signal candidates are plotted in a two-dimensional space defined by the invariant mass of the LFV candidate and the energy residue taken as a difference from the CM beam energy. Signal events are expected to exhibit an invariant mass close to the τ mass (1.78 GeV) and a zero deviation from the beam energy, as shown in figure 1.9.
The main background sources are semi-leptonic τ decays, $q\bar{q}$ production and radiative Bhabha scattering.
The main source of systematic uncertainty is represented by the lepton identification efficiencies, the MC statistics and the luminosity estimation.

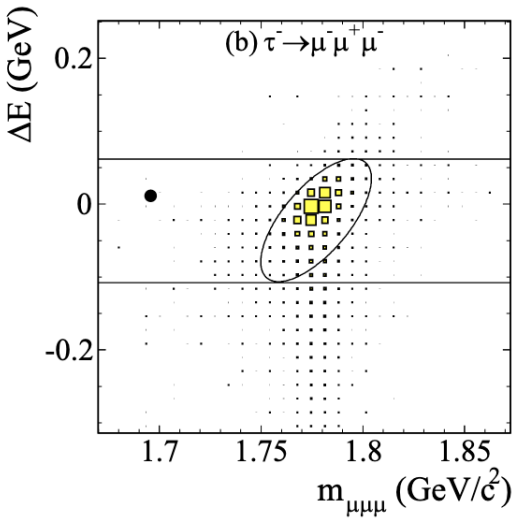

Figure 1.9: Scatter plot in the $M_{3\mu}$- ΔE plane [3]. The black dots indicate the data collected, while the yellow boxes indicate the MC simulation. The elliptical region is used to evaluate the signal yield.

The final limit is calculated in an elliptical region containing the 90% of the signal. No evidence of decay was found and an upper limit was set at 90% CL.

$$\mathscr{B}(\tau \to 3\mu) < (2.10 \pm 0.16^{sys}) \times 10^{-8} \quad @ \quad 90\%\ CL$$

The currently operating collider SuperKEKB is expected to push the instantaneous luminosity up to forty times the current value, reaching 80×10^{34} s^{-1} cm^{-2}. If New Physics is nested in this process, evidences are expected to be found within the large statistics that will be collected [32].

A similar strategy was employed by the BaBar collaboration at the SLAC (Stanford Linear Accelerator Center) National Accelerator Laboratory [33] using an integrated luminosity of 468 fb^{-1}, setting an upper limit on the branching ratio at 90% of CL of 3.3

$\times 10^{-8}$.

1.5.2 LHCb

The first searches for the $\tau \to 3\mu$ decay at hadronic colliders has been carried out by the LHCb collaboration.
The search for LFV in τ decays at LHCb takes advantage of the large inclusive τ production cross-section at the LHC, where τ leptons are produced almost entirely from the decays of b and c hadrons. Using the bb and cc cross-sections measured by LHCb [34] [35] and the inclusive $b\to \tau$ and $c\to \tau$ branching fractions, the inclusive τ cross-section is estimated to be 85 μb at 7 TeV.

A careful study of background contaminations is performed: the background processes for $\tau \to 3\mu$ decay mainly consist of heavy meson decays yielding three muons in the final state, or one or two muons in combination with two or one misidentified particles. There is also a large number of events with one or two muons from heavy meson decays combined with two or one muons from elsewhere in the event. In addition, decays containing undetected final-state particles, such as K^0_L mesons, neutrinos or photons, can give large backgrounds, which vary smoothly in the signal region. The dominant contributions to the background from misidentified particles are from $D_s \to K^+\pi^-\pi^-$ and $D_s \to \pi^+\pi^-\pi^-$, which can be reduced to negligible level thanks to the Multivariate Particle Id classifier.

The sensitivity reached by analysing LHCb data corresponding to 3 $fb^{-1}$is sufficient to constrain the branching fraction of $\tau \to 3\mu$ to be smaller than 4.6×10^{-8} at 90% CL [36].

1.5.3 ATLAS

The ATLAS collaboration set a limit on the $\tau \to 3\mu$ process utilising the W boson as a source of τ lepton. The analysis was conducted on a 20.3 fb^{-1} data sample, collected during the 2012 LHC Run at the centre of mass energy of $\sqrt{s}$ = 8 TeV [4].

The analysis procedure is developed in four steps. First, events containing high-quality muon objects are selected, applying a p_T cut of 2.5 GeV. These muons are required to originate from a common vertex, on which quality constraints are imposed, such as a goodness-of-fit cut and the request of a displaced τ decay, the latter made possible by the high transverse mass of the W bosons.
Second, a loose selection is applied to the sample obtained in the previous step. The

background passing the selection was used to train the final multivariate discriminator (a Boosted Decision Tree - BDT).
Third, a tight selection is applied and, at the same time, a cut on the BDT score was required in order to exclude the looser background events.
Fourth, the discriminating power of the BDT is studied as a function of the cut point. The final analysis is conducted on events passing this cut and the tight selection. The BDT score distribution is shown in figure 1.10.

The final result is obtained fitting the signal region, defined between 1.713 GeV and 1.841 GeV, extrapolating the background from the sidebands with a polynomial function, as shown in figure 1.11. No signal evidence is found and an upper limit equal to 3.76×10^{-7} is imposed on the $\tau \rightarrow 3\mu$ branching ratio [4].

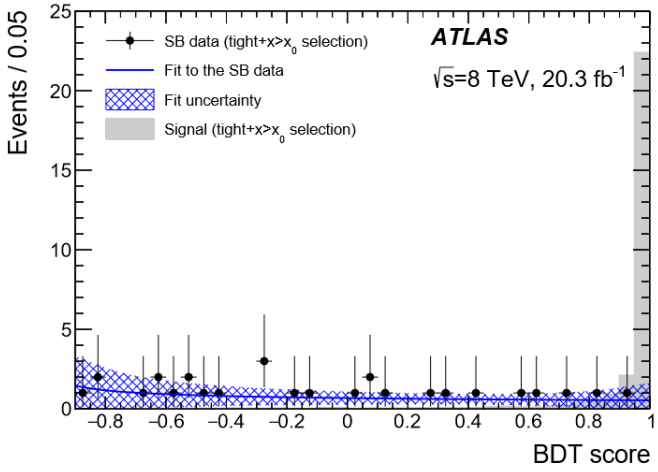

Figure 1.10: The ATLAS $\tau \rightarrow 3\mu$ final discriminator [4]. The black points corresponds to the sidebands events, while the gray area shows the signal distribution, obtained from a MC simulation. The events shown are required to pass the tight selection plus a loose selection on the BDT score.

1.5.4 CMS: results from 2016 Run-II data

The CMS collaboration published the first result on the $\tau \rightarrow 3\mu$ search in Jan. 2021 [5]. This result is obtained using the data collected during 2016 proton-proton collisions at the centre of mass energy of 13 TeV, corresponding to an integrated luminosity of 33 fb^{-1}. This work served as a benchmark for the study carried out on the full Run-II statistic, described in chapter 3.

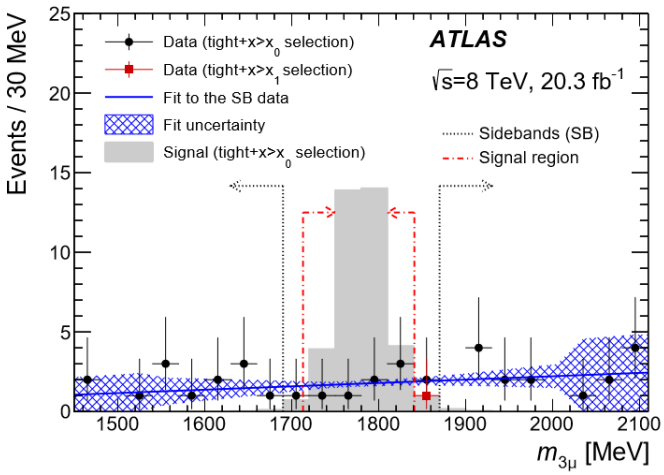

Figure 1.11: Results from the ATLAS analysis. Data passing the tight muon ID and the loose BDT cut are represented as black dots, while data passing the tight muon ID and the tight BDT cut are represented as red squares.

The analysis at CMS is done exploiting two sources of τ lepton: W bosons ($W\rightarrow \tau\nu$ decays) and Heavy Flavour (HF) mesons (mainly from $D_s \rightarrow \tau\nu$ and $B+ \rightarrow \tau\nu$ decays). I contributed to the W channel analysis, which is part of my PhD work.
The W channel τ production happens via the $W\rightarrow \tau\nu$ decay. At the LHC, at the centre of mass energy of 13 TeV, the $pp\rightarrow W$ production cross section is equal to 19950 pb [37]. At this rate, about 10^9 τ leptons are expected to be produced in 150 fb^{-1}. This number, although comparable to that of B-factories Belle and BaBar (where the τ pair production cross section is about 0.9 nb [38]), is far lower than the heavy hadron production rate. In fact, at hadron colliders, τ leptons are mainly produced via B and D meson decays, which represent more than 99.99% of the total τ production rate, as summarised in Tab. 1.2. Anyway, although less abundant with respect to B and D meson events, W bosons events are more suited for trigger selection and background suppression if compared to events from the HF channel. Indeed, the harder momentum spectrum of the signal muons, the isolation of the three-muon final state, and the larger missing energy associated to the neutrino make this channel more suited to reconstruction and trigger selection at CMS. For this reason, a dedicated trigger selection has been developed for the W channel and will be described in Sec. 3.1.1. Table 1.2 shows the number of τ leptons produced in different channels during 2016.

The two channels share the same strategy for computing the final limit on the $\tau \rightarrow 3\mu$ branching fraction.

Table 1.2: Tau lepton production numbers at the LHC in proton-proton collisions at the centre of mass energy of 13 TeV. Estimates are obtained by the Pythia 8 generation tool.

source	number of tau leptons produced in 33 fb^{-1}
$D \rightarrow \tau\nu$	4.0×10^{12}
$B \rightarrow \tau\nu$	1.5×10^{12}
$B \rightarrow D(\tau\nu)$	6.3×10^{11}
$W \rightarrow \tau\nu$	6.7×10^{8}

First, events are selected by the dedicated High-Level trigger (see Sec. 2.4) HLT_ DoubleMu3_Tau3Mu, which tags events, during data acquisition, with two L3 muons and one track with the following requirements:

- the L3 muons should have a p_T greater than 3 GeV and fall in the pseudorapidity range (-2.5, 2.5).
- the L3 muons should make a good secondary vertex, with a probability greater than 1%.
- the displacement of the di-muon secondary vertex should be greater than one time its uncertainty.
- the pointing angle between the segment connecting the primary and secondary vertex, and the di-muon momentum vector should have a cosine greater than 0.
- the p_T of the di-muon object should be greater than 6 GeV.
- the radial distance $\sqrt{\Delta\phi^2 + \Delta\eta^2}$of the two muons should be lower than 0.6.
- the additional track should have a p_T greater than 1.2 GeV and fall in the pseudorapidity range (-2.5, 2.5).
- the three-body object (the two L3 muons and the track) should make a good vertex, with a fit χ^2 lower than 8.
- the three-body object should have a p_T greater than 8 GeV.
- the displacement of the secondary vertex identified by the three-body object should be greater than twice its uncertainty.
- the pointing angle between the segment connecting the primary and secondary vertex, and the di-muon momentum vector should have a cosine greater than 0.9.
- the invariant mass of the three-body object should fall into the range (1.6 GeV, 2.02 GeV).

The HLT path described above was seeded by the L1 seeds listed in Tab. 1.3.
After the online selection, data are skimmed and the $\tau \to 3\mu$ candidates are identified. To do this, events with three muons reconstructed offline, lying within the CMS acceptance region (p_T > 1 GeV and 0 <= |η | < 2.4), with an invariant mass between 1.6 and 2.0 GeV, and with a total electric charge of ± 1 are selected; to improve the τ candidate mass resolution, the muon tracks are refit to a common vertex (the $\tau \to 3\mu$ decay vertex),

Table 1.3: Lists of L1 seeds used by the HLT_DoubleMu3_Tau3Mu trigger.

name	requirements
L1_DoubleMu0er1p6_dEta_Max1p8	two L1 muons with η<1.6 and a maximum distance in pseudorapidity of 1.8
L1_DoubleMu_10_0_dEta_Max1p8	two L1 muons with η<1.6 and a maximum distance in pseudorapidity of 1.8. The first muon is selected with a p_T greater than 10 GeV
L1_DoubleMu0er1p6_dEta_Max1p8_OS	two opposite-sign L1 muons with η<1.6 and a maximum distance in pseudorapidity of 1.8
L1_DoubleMu0er1p4_dEta_Max1p8_OS	two opposite-sign L1 muons with η<1.4 and a maximum distance in pseudorapidity of 1.8
L1_DoubleMu_11_4	Two L1 muons. The first muon is selected with a p_T greater than 10 GeV. The second muon is selected with p_T greater than 4 GeV.
L1_TripleMu0	three L1 muons
L1_TripleMu_5_0_0	three L1 muons. The first muon is selected with a p_T greater than 5 GeV

and their parameters are recomputed. Events with two opposite-charge signal muons with invariant mass close to the ϕ and ω resonances masses are vetoed to suppress the possible contamination coming from $D^{\pm} \to \phi/\omega\,\pi^{\pm}$ decays.
Events with a valid $\tau \to 3\mu$ candidate are further processed by a multivariate discriminator. For both the W and HF production channels, the discriminator is a Boosted Decision Tree (BDT), trained on simulated signal samples to model the signal, and on data events whose $\tau \to 3\mu$ candidate invariant mass lies outside the τ mass region [1] to model the background. This strategy was adopted as it allowed for an excellent separation of the signal from the background, and proved to be more effective than a cut-based approach, as shown in Fig. 1.12.

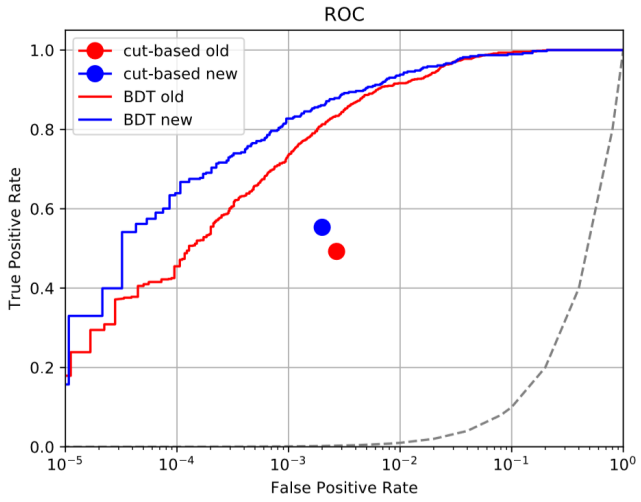

Figure 1.12: Comparison of the signal efficiency and background rejection power of the BDT used by the W channel analysis (two different versions of the BDT are shown) and a cut based-analysis (two different versions of a cut based approach ara shown). Typical values of signal efficiency used in the search are around 30%, which correspond to a background rejection efficiency of about 99.995%.

In the case of the D and B production channel, the simulated signal sample is normalized with respect to the $D^{\pm} \to \phi\pi^{\pm}$ production rate observed in data. For the W production channel, the signal sample is normalized to the pp$\to$W ($\tau\nu$) cross section, taken from literature, using the formula:

$$N = \mathscr{L}\sigma(pp \to W, W \to \mu\nu)\frac{\mathscr{B}(W \to \tau\nu)}{\mathscr{B}(W \to \mu\nu)}\mathscr{B}(\tau \to 3\mu) \tag{1.46}$$

[1] These two regions, corresponding to the 1.6-1.74 GeV and 1.82-2.0 GeV regions, will be referred as *sidebands*

where N is the number of expected signal events in the collected data, $\mathscr{L}$ is the integrated luminosity of the collected data, $\sigma_{pp\to W,W\to\mu\nu}$ is the W production cross-section in the $\mu\nu$ channel [37], and $\mathscr{B}(W\to\mu\nu)$ and $\mathscr{B}(W\to\mu\nu)$ are the W boson branching fraction taken from the PDG.
To improve the search sensitivity, events are separated into different categories. For events originating from D and B meson decays, three categories are defined based on the three-muon mass resolution (with the separations at 0.7% and 1.0%) and for each one of them two categories are defined based the BDT score; for the W boson production channel, events are divided into two categories based on the $\tau\to 3\mu$ candidate pseudo-rapidity, with the separation at 1.6 (the *barrel* and *endcap* categories).

The presence of the $\tau\to 3\mu$ process is inferred from the three-muon mass distribution of data events passing the BDT selection. If the signal was present, it would manifest as an accumulation of events around the τ lepton mass value (1.777 GeV); thus, the signal strength of the process is computed with an unbinned maximum likelihood fit to the mass distribution.
Figure 1.13 shows the $\tau\to 3\mu$ candidates mass distribution for the events passing the BDT selection. As no evidence of signal was found, an upper limit was set at 90% of Confidence Level (CL); to set the upper limit, the CLs method (see Sec. A) with the LHC test statistics was used. The result obtained is

$$\mathscr{B}(\tau\to 3\mu) < 8.0\times 10^{-8} \;\; @ \;\; 90\%\; CL \tag{1.47}$$

The result obtained on 2016 data showed the potentiality of the CMS experiment in this search. The analysis of the remaining data of the Run II period (the years 2017 and 2018, corresponding to about 90 fb^{-1}) and the combination with the 2016 result are the topic of this thesis and will be discussed in details in chapter 3.

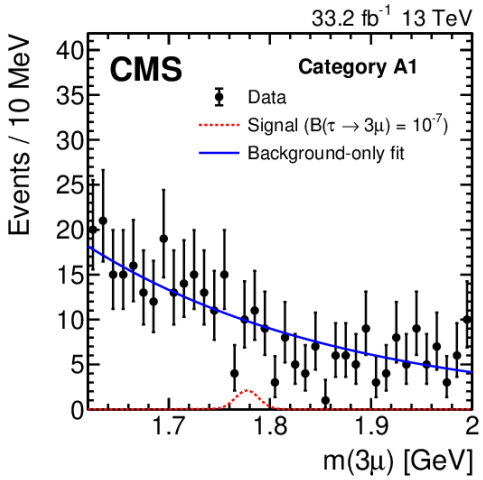
33.2 fb^{-1} 13 TeV
CMS
Category A1
Data
Signal (B(τ → 3μ) = 10^{-7})
Background-only fit
Events / 10 MeV
m(3μ) [GeV]

(a)

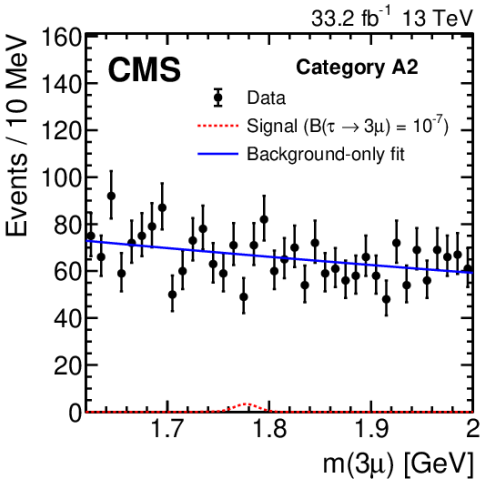
33.2 fb^{-1} 13 TeV
CMS
Category A2
Data
Signal (B(τ → 3μ) = 10^{-7})
Background-only fit
Events / 10 MeV
m(3μ) [GeV]

(b)

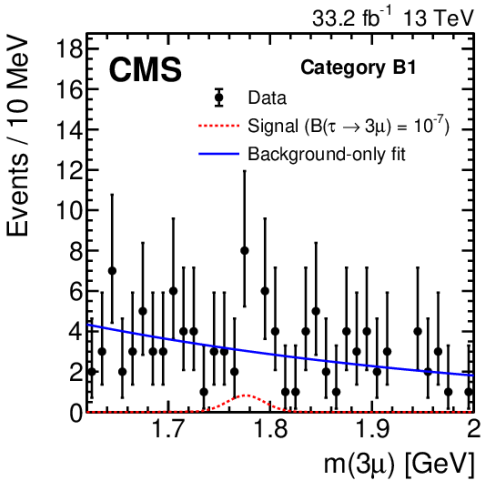
33.2 fb^{-1} 13 TeV
CMS
Category B1
Data
Signal (B(τ → 3μ) = 10^{-7})
Background-only fit
Events / 10 MeV
m(3μ) [GeV]

(c)

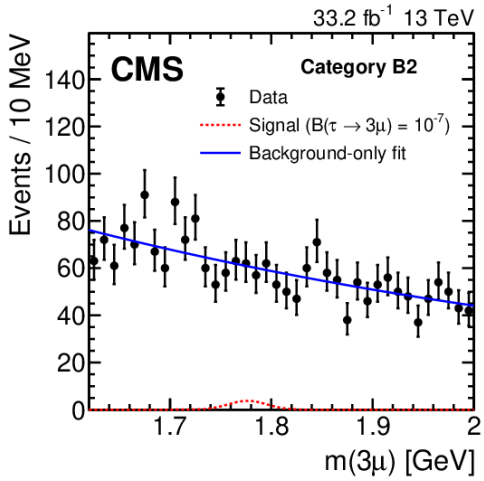
33.2 fb^{-1} 13 TeV
CMS
Category B2
Data
Signal (B(τ → 3μ) = 10^{-7})
Background-only fit
Events / 10 MeV
m(3μ) [GeV]

(d)

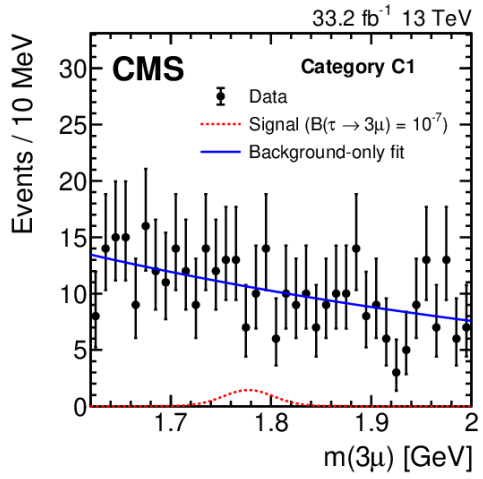
33.2 fb^{-1} 13 TeV
CMS
Category C1
Data
Signal (B(τ → 3μ) = 10^{-7})
Background-only fit
Events / 10 MeV
m(3μ) [GeV]

(e)

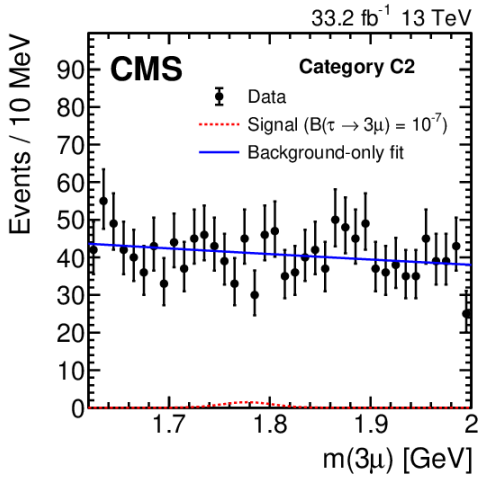
33.2 fb^{-1} 13 TeV
CMS
Category C2
Data
Signal (B(τ → 3μ) = 10^{-7})
Background-only fit
Events / 10 MeV
m(3μ) [GeV]

(f)

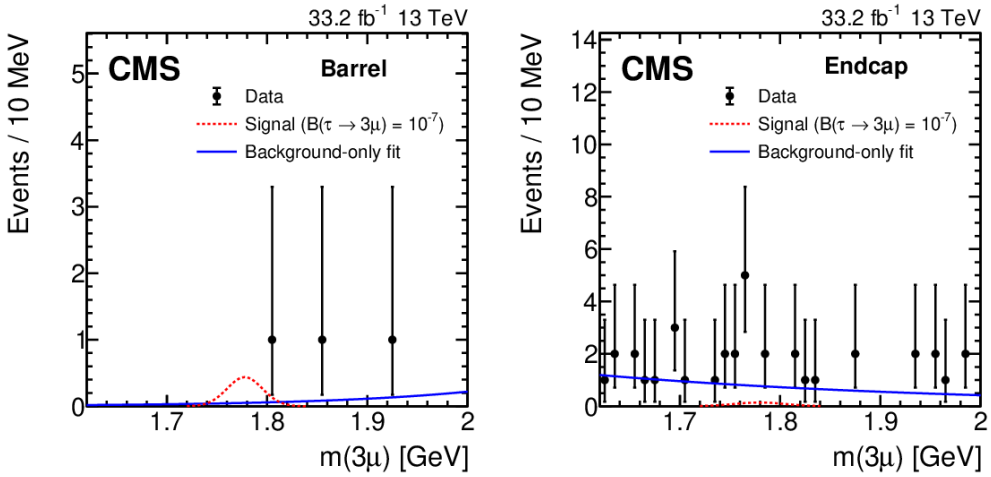

(g) *(h)*

Figure 1.13: Signal candidate invariant mass plots of the events selected by the BDT for the heavy flavour production channel (plots 1.13a to 1.13f) and for the W production channel (plots 1.13g and 1.13h). Each plot corresponds to an event category, as described in the text. The black points represent the data, the red dots the signal simulation normalized to a $\tau \to 3\mu$ *branching fraction of* 10^{-7}*. For both channels, the background is modelled by an exponential function; the signal is modelled by a gaussian function for the W channel and by a gaussian-plus-crystalball function for the heavy flavour channel*

Chapter 2

The LHC collider and the CMS experiment

In this chapter an outline of the LHC collider properties and of the CMS experiment is given, which will be useful to better understand the analysis strategy implementation and its details. The high performance reached by the LHC machine (described in Sec. 2.1), in particular its high proton collision rate, makes the search for rare processes possible at hadron colliders. At the same time, the excellent performance of the CMS detector allows for a physics programme which spans from high p_T ranges, such as the study of the Higgs boson properties or the searches for new physics at the TeV scale, to the low p_T range, like the search for lepton anomalies. The excellent tracking resolution (described in Sec. 2.2.1), together with a dedicated high-field dipole magnet, has an essential role in the high luminosity regime of the collider, making the precision measurements of the position of primary and secondary vertices possible, thus reducing the impact of the large hadron activity of proton collisions. The presence of hermetic electromagnetic and hadron calorimeters (described in Sec. 2.2.2 and Sec. 2.2.3) allows for a good estimation of the missing transverse energy, a peculiar signature of many physics final states. This, together with dedicated muon sub-detectors (described in Sec 2.2.4) and a complex trigger system (described in Sec. 2.4) allows to target efficiently specific processes, reducing the contamination which arises from the abundant soft activity of proton collisions.
The $W\rightarrow \tau\nu$, $\tau \rightarrow 3\mu$ process, topic of this thesis, is characterized by a three-muon final state, the presence of a large missing energy and of a displaced secondary vertex; for these reasons, it can benefit from all the above-mentioned features of the detector, allowing CMS to reach world-competitive results in the field of lepton flavour violation searches.

2.1 The Large Hadron Collider

The Large Hadron Collider (LHC) is a superconducting particle accelerator built between the French and Swiss border at the Conseil Européen pour la Recherche Nucléaire (CERN). Installed in the 27 km underground tunnel previously occupied by the Large Electron-Positron collider (LEP), LHC has been designed to collide proton beams at a centre of mass energy $\sqrt{s} = 14$ TeV and achieve an instantaneous luminosity of $10^{34}\ s^{-1}\ cm^{-2}$ [39].
The prime motivation that lead to the construction of LHC was the study of the spontaneous symmetry breaking mechanism and the search of the Higgs boson. The experimental study of the Higgs mechanism will shed light on the mathematical consistency of the SM at the TeV energy scale. Indeed, although the SM describes with a high precision physical processes at the GeV scale, it is thought to be an effective theory, valid up to some scale $\Lambda \approx$ TeV. New physics might manifest at the energies provided at the LHC.
The LHC can also accelerate and collide heavy ions at an average centre of mass energy of 5.02 TeV per nucleon [40], allowing to recreate the conditions similar to those of the early stages of the universe, and extend the knowledge of heavy ion physics and hot nuclear matter.
For all these reasons, LHC represents an unprecedented challenge from the point of view of technologies and human resources involved.

2.1.1 The LHC operation

The LHC collider delivered the first proton-proton collision on November 23, 2009, at the centre of mass energy of 0.9 TeV, followed immediately by a 1.18 TeV collision. During the years, LHC has constantly improved its luminosity and collision energy, achieving a maximum of $\sqrt{s} = 13$ TeV.
During 2011 Run, the LHC collider worked with $\sqrt{s} = 7$ TeV and a peak instantaneous luminosity of 4×10^{33} $s^{-1}cm^{-2}$, while during 2012 it reached $\sqrt{s} = 8$ TeV and a luminosity of 7×10^{33} $s^{-1}cm^{-2}$. In this period, the total integrated luminosity collected from pp collisions was about 25 fb^{-1}.
After the 2012 Run, the first Long Shutdown (LS1) period followed and LHC resumed the collisions in 2015. This technical stop allowed for further upgrades and permitted to reach the nominal luminosity goal. In 2015 the LHC collider delivered proton-proton collisions at $\sqrt{s} = 13$ TeV, reaching a peak luminosity of 1.74×10^{34}, 74% more than the purported value.
During the following years, the peak instantaneous luminosity increased from 1.5×10^{34} $s^{-1}cm^{-2}$ in 2016, to reach 2.0×10^{34} $s^{-1}cm^{-2}$ in 2017 and 2018 [41]. At the end of this period, known as Run2, the total integrated luminosity collected by CMS was equal to

146.9 fb^{-1}, with 38.25 fb^{-1}, 44.98 fb^{-1}and 63.67 fb^{-1}collected respectively in 2016, 2017 and 2018.

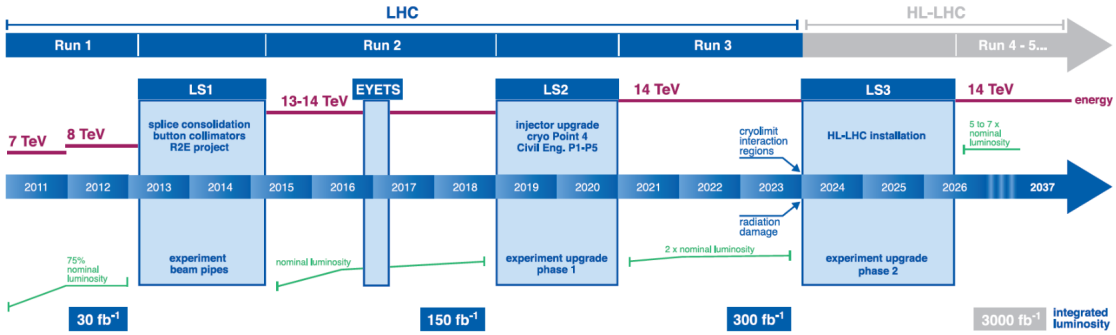

Figure 2.1: The LHC collider operation outline for the future years

2.1.2 The LHC luminosity and general properties

In high energy physics, luminosity is a quantity used to measure the capability of a machine to collide particle in an efficient way, and can be defined as the rate of collision for a given process, that is $L = n\sigma^{-1}$, where n is the observed interaction rate and σ the cross section. In terms of machine parameters, it can be expressed as

$$\mathscr{L} = \frac{N_b^2 n_b f}{A_{eff}} F \tag{2.1}$$

where N_b is the number of particles per bunch, n_b is the number of bunches per beam, f is the revolution frequency, A_{eff} is the effective transverse area of the beam.
In addition, a small crossing angle (about 123 µrad) is required at the interaction points (IP), in order to avoid multiple bunch interactions. This angle lowers the luminosity by a factor F (geometrical factor), due to the partial overlap of the bunches. Some techniques can help to reduce the impact of this effect. For example, special RF cavities (crab cavities), capable of generating a transverse electric field, hence rotating the bunch and allowing a head-on collision, will be employed during the HL-LHC period [42].

The nominal number of bunches per beam is 2808, equally spaced by 25 ns and circulating at a frequency of 11.24 kHz. Each bunch contains 10^{11} protons and has a transverse dimension of about 20 µm at the interaction points (IP) [43].
The LHC collider reached a maximum luminosity of 1.74×10^{34} s^{-1} cm^{-2} already in 2015. The major upgrade foreseen for the LS2 (High Luminosity LHC) will permit to reach a peak five times bigger than the nominal value.

The request of a high nominal luminosity value, and thus the necessity of having high populated bunches, prohibited the use of antiproton beams, making necessary the construction of two different pipes. Two beams of protons circulates in opposite direction inside the LHC tunnel and cross only at the interaction points, where the experiments are located. For this purpose, as there is hardly enough room for two separated beam pipes, LHC employs twin bore magnets consisting of two sets of coils and beam channels within the same mechanical structure and cryostat [44].

The high energy provided by the LHC ring cannot be achieved in one step. Different phases of acceleration, hence different accelerating machines, are needed in order to reach the nominal 7 TeV value.
Protons are obtained by stripping electrons off from hydrogen atoms and firstly accelerated in a linear machine, called Linac2, which uses radio-frequency (RF) cavities to boost the particles up to 50 MeV. The beams are then injected into the Proton Synchrotron Booster (PSB), which also uses RF cavities and brings the particles up to 1.4 GeV. After the PSB acceleration, protons are sent to the Proton Synchrotron (PS) and brought to 24 GeV and then sent into the Super Proton Synchrotron (SPS). The SPS represents the final stage of pre-acceleration, bringing the proton beams up to 450 GeV.
Once the bunches are in the LHC ring, they are accelerated to the final energy using eight 40 MHz RF cavities per beam, each delivering a 5 MV m^{-1} accelerating field. With a curvature radius of 2780 m, LHC employs 1232 superconducting dipole magnets operating at about 8 T in order to bend 7 TeV protons. LHC dipoles are made of a niobium-titanium compound, which is kept at superconducting regime by a liquid helium cooling system working at 1.9 K. Together with bending magnets, 392 quadrupole magnets are installed along the LHC ring, allowing to focus the beams and shrink their size at the collision points [44]. Figure 2.2 shows the LHC pre-accelerating system.

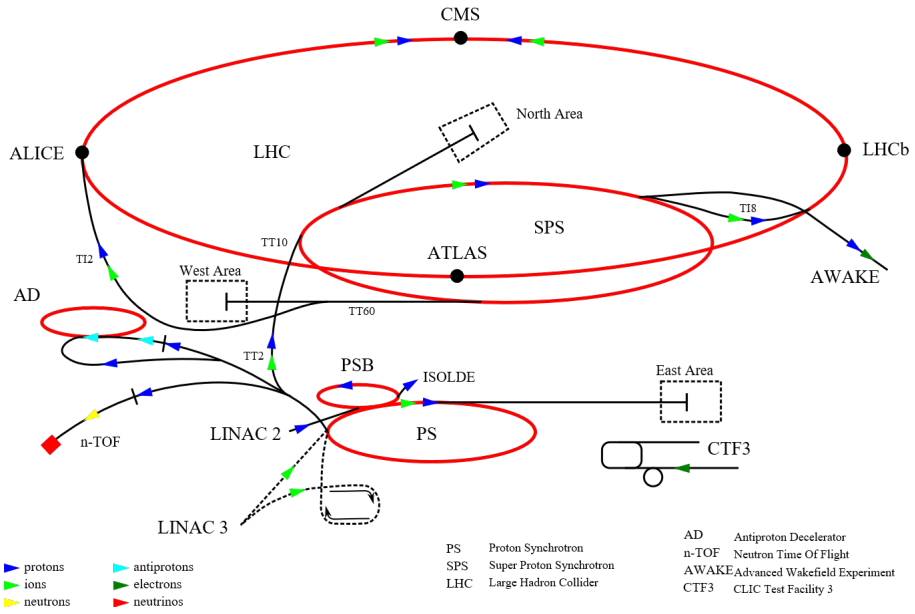

Figure 2.2: The LHC pre-accelerating system

Four large experiments are placed along the LHC ring at the collision points: ALICE (A Large Ion CollidEr), ATLAS (A Toroidal LHC ApparatuS), CMS (Compact Muon Solenoid) and LHCb (Large Hadron Collider beauty).
ATLAS and CMS are general purpose experiments, looking for answers to open questions in high energy physics, such as the possible existence of supersymmetric particles and dark matter. ATLAS and CMS have been the first experiments to observe the Higgs boson in 2012. Although they have common goals, they employ different techniques and solutions to achieve them.
ALICE is dedicated to the study of heavy ions physics and the investigations of strong interacting matter. This experiments exploits the Pb ions fills of LHC, and aims to recreate the conditions of the early stages of the universe. ALICE has been built to study the peculiar state of matter known as quark-gluon plasma, a state where quarks and gluons are weakly bounded.
LHCb is dedicated to the study of CP-violating processes and rare heavy flavour decays to reveal indirect evidences of new physics beyond the standard model.

2.1.3 Proton-proton collisions at LHC

In a hadron collider, the particles responsible for the final states production are the partons (quarks and gluons), which carry a fraction of the total momentum of the proton. For this reason, the total momentum involved in the interaction is unknown and cannot be used as a constraint; the transverse total momentum is although known and equal to

zero, and its conservation plays a fundamental role in the event reconstruction.

Different types of interactions can occur in a hadronic collision. At 13 TeV, the total cross section for two colliding protons is 110.6 mb; about 70% of it is constituted by inelastic collisions [45], among which soft and hard collisions can be distinguished.
The former are generated when a small momentum transfer is involved in the process. The produced particles have a low transverse momentum and a higher longitudinal momentum and therefore are very close to the beam pipe and likely to escape detection.
The latter are characterized by a high momentum transfer originating from a head-on collision. This type of interactions are suited for high energy physics analyses. However, hard scattering is but a small part of the total inelastic cross section and the detector requires a trigger system in order to exclude the uninteresting soft collision products.
Other types of events are present in a bunch collision, making the selection and reconstruction more complicated: underlying events can be generated by the hard scattering remnants, initial or final state radiation, and multiple parton interaction occurring during the same bunch crossing (*pileup*). The number of underlying events is influenced by the value of the instantaneous luminosity of the machine. During 2016, the average number of pileup interaction was 23. This number has increased to 32 during 2017 and 2018, and reached peak values up to 60. For the HL-LHC, its average value is predicted to be as big as 200, and new techniques will be required to reduce the impact on events reconstruction [46] [47].

2.2 The CMS detector

The Compact Muon Solenoid is a general purpose experiment installed in one of the interaction points situated along the LHC beam line. The CMS detector was built to fulfill the following requests:

- Good reconstruction of leptons and photons with large transverse momentum, excellent reconstruction of electromagnetic energy deposits and muon tracks
- Good jet reconstruction and resolution, good reconstruction of hadronic energy deposits, efficient τ and b identification
- Good measurement of the missing energy in the transverse plane
- Capability of measurements in the forward region
- High granularity, fast readout and radiation hard tracking detector

The detector, shown in figure 2.3, is a 21.6 m long cylinder with a diameter of 14.6 m and a weight of about 12 kt, inside which in five regions can be distinguished: the central barrel, two endcaps and two forward regions outside the endcaps.
The core of the detector is constituted by the magnet. It is a 12.9 m long superconducting solenoid made of high purity aluminium coils traversed by 20 kA and able to produce a uniform magnetic filed of 3.8 T parallel to the beam axis, allowing to measure the transverse momentum of the particles with good resolution within compact dimensions. The solenoid is kept at the temperature of liquid helium inside a vacuum tank. Combined with the high precision tracker, it allows a precise measurement of the particle track parameters, and of the primary and secondary vertices positions.
The magnet is sustained by a 1.5 m thick steel yoke, which ensures the magnetic field return and guarantees the homogeneity of the field. The yoke encompasses the muon stations, responsible of the muon tracking and identification, acting at the same time as a muon filter.
The bore of the solenoid is big enough to store the electromagnetic and hadronic calorimeters and, closer to the beam pipe, the tracking sub-detector [39].

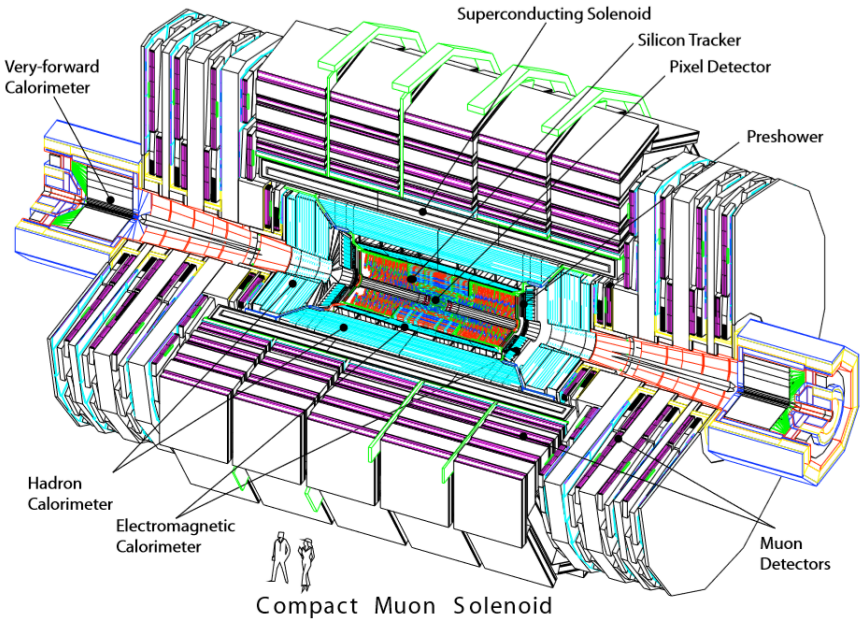

Figure 2.3: The CMS detector and its subdetectors

CMS adopts an orthogonal right-handed Cartesian system, centred in the interaction point. The z axis is parallel to the beam line, while the x axis is directed towards the centre of the LHC ring and the y axis is directed upward. Due to its cylindrical symmetry, a different system is widely used, defined by the r, ϕ and η coordinates, being r the distance from the z axis, ϕ the azimuthal angle and η a quantity defined upon the polar angle θ

$$\eta = -ln\left(\tan\frac{\theta}{2}\right) \tag{2.2}$$

The advantage of η over θ is that the distribution of particles is approximately uniform along the η coordinate.
Due to the impossibility of ensuring the longitudinal momentum conservation, the transverse momentum is taken into consideration

$$p_T = \sqrt{p_x^2 + p_y^2} \tag{2.3}$$

The CMS detector is built to ensure an high hermeticity up to $\eta = 5$.

2.2.1 The inner tracker

The CMS tracker is an all-silicon detector with a sensitive area of 200 m^2 [39] [48] [49]. Its sensors are arranged in concentric cylinders around the interaction region, inside the

3.8 T magnetic field generated by the superconducting solenoid. The aim of the detector is to guarantee a high precision reconstruction of the particles trajectories up to a pseudorapidity of $|\eta| = 2.5$.
The CMS tracker was built upon the request of a fast and radiation hard detector, able to sustain the high luminosity operation regime of the LHC machine without degrading its performance. The tracking detector is divided in three different regions, and each region occupies a different part of the detector, undergoing different radiation loads. Therefore different technologies are implemented in the inner and outer areas of the tracker.
In the inner part of the barrel (r between 4 cm and 10 cm), where the flux of particles is higher, a pixel detector is used. In the outer barrel, where the radiation flux is lower, a strip detector is sufficient. The barrel region is enclosed by two endcap, that also employ silicon strip detectors.
The CMS tracker operates at - 20°C in order to reduce the temperature dependent radiation damage [50] [51].

The pixel detector, shown in figure 2.4, is composed by four layers located at 2.9 cm, 6.8 cm, 10.9 cm and 16.0 cm. It is enclosed by three endcap disks at each side, extending from 6 cm to 15 cm of radius and situated at $|z| = 29.1$ cm, 39.6 and 51.6 cm.
The pixel tracker has a surface of about 1 m^2 and it is segmented into 80 million n^+ type pixels, each with a size of $100 \times \mu m^2$ and a thickness of 250 µm, arranged in 1200 modules. The $r-\phi$ resolution of the tracker is enhanced making use of the Lorentz angle (about 32°), exploiting the charge sharing among adjacent pixels. The endcap part of the pixel detector is composed by three disks on each side, mounting three layers of silicon pixel detectors, for a total of 45 million channel assembled into 672 modules. The result is a tracking detector with a 10 µm resolution in the $r-\phi$ plane and a 20 µm resolution in the z coordinate per point.
The current pixel detector is the result of the LS1 upgrade [52] [53], during which a fourth layer was added in the barrel area and a third layer was added in the endcap area, allowing a better vertex resolution and track extrapolation. A new cooling system was implemented, as well as a new mechanical structure, allowing to reduce the overall material budget, as shown in figure 2.5

The strip detector is divided in two regions: the Tracker Inner Barrel (TIB, r between 25 cm and 64 cm) and Tracker Outer Barrel (TOB, r between 64 cm and 110 cm).
The TIB is composed by four concentric layers, each mounting 320 µm thick silicon sensors with a strip pitch varying between 80 and 120 µm, covering up the $|z| < 65$ cm region. The first two layers are double sided sensors with a 100 mrad stereo angle, allowing the measurement of the $r-\phi$ and $r-z$ coordinates with a precision between 23 and 34 µm for the $r-\phi$ plane and 23 µm for the z direction.

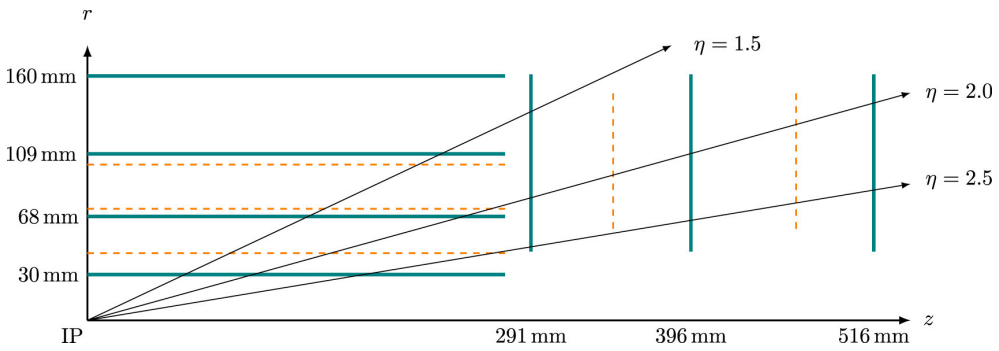

Figure 2.4: The CMS pixel detector layout in the z-r view. The green lines indicated the current arrangement, the orange dashed lines indicated the Run1 arrangement.

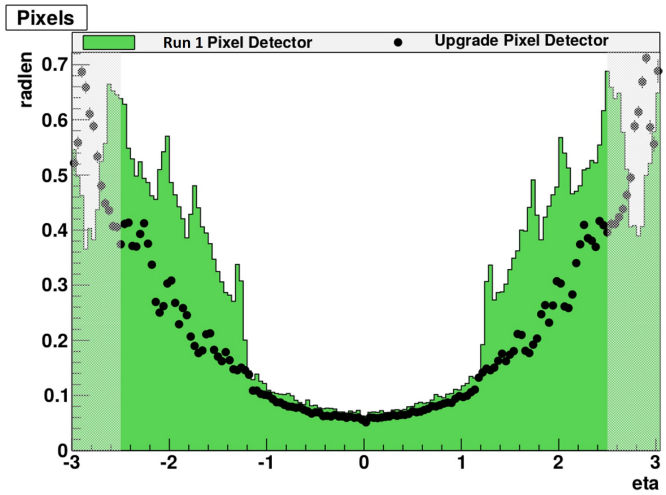

Figure 2.5: The CMS tracker material budget before and after the LS1 pixel upgrade

The TOB is composed by six layers covering up to $|z| = 110$ cm, with 500 µm thick strip sensors and a pitch that varies between 120 and 180 µm. As for the TIB detector, the first two layers of the TOB are double sided modules with a stereo angle of 100 mrad. The single point resolution varies from 35 to 52 µm for the $r - \phi$ plane and is 52 µm in the z direction.

The endcap detector is also divided in two regions: the Tracker End Cap (TEC) and the Tracker Inner Disks (TID).
Each TEC is composed of nine disks that extend from $|z|$ = 120 cm to $|z|$ = 180 cm, while the TID are made of three smaller disks that fill the gaps between the TEC and the TIB. Both the TEC and the TID disks are made of strip detectors pointing towards the beam line, therefore presenting a variable pitch. The two innermost and the fifth TEC ring mount stereo modules. The thickness of the sensors is 300 µm for the TID and the three

innermost rings of the TEC, and 500 μm for the remaining rings of the TEC.
The CMS tracker guarantees a full coverage up to $|\eta|$ = 2.5, with more than 10 high-resolution measurements points [54].

The CMS tracker schematic is shown in figure 2.6.

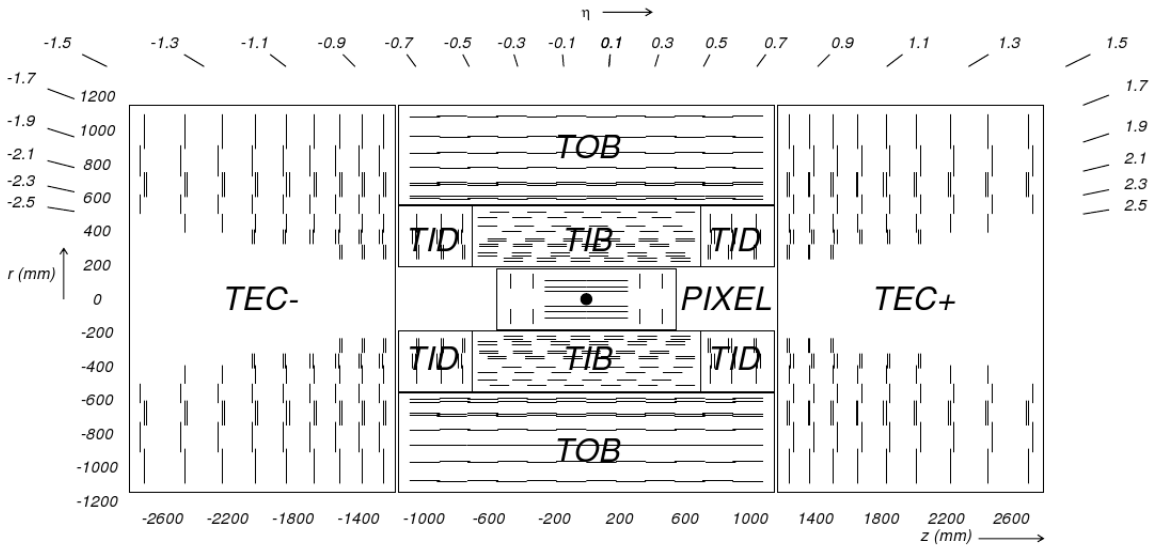

Figure 2.6: The CMS tracker in the r-z view

The track reconstruction allows to measure the transverse momentum of the charged particles, according to the relation $p_T = qRB$, where the magnetic field B and the charge q are known and the curvature R is deduced by the track reconstruction. The p_T estimation efficiency gets worse as the transverse momentum of the track increases, since the bending radius decreases. The CMS tracker performance is reassumed in Eq. 2.4.

$$\begin{aligned} \frac{\sigma_{p_T}}{p_T} &= 0.015\% \cdot p_T \ [GeV] \ + 0.5\% \quad |\eta| < 1.6 \\ \frac{\sigma_{p_T}}{p_T} &= 0.060\% \cdot p_T \ [GeV] \ + 0.5\% \quad |\eta| \in (1.6, 2.4) \end{aligned} \tag{2.4}$$

2.2.2 The electromagnetic calorimeter

The CMS electromagnetic calorimeter (ECAL) is a hermetic and homogeneous detector, composed by 61 200 $PbWO_4$ crystals mounted in the barrel and 7 324 $PbWO_4$ crystals mounted in each endcap [39] [55]. The choice of lead tungstate, which presents a radiation length X_0 of 0.89 cm and a Moliere radius of 2.19 m, ensures a good compactness and radiation hardness. The ECAL design is driven by the necessity of having an excellent energy resolution and a good hermeticity, allowing a precise measurement of

the missing transverse energy.
The small radiation length and Moliere radius guarantees a good longitudinal and transverse containment of the electromagnetic showers, while its fast response (25 ns) and its radiation hardness make the detector capable of operating within the harsh LHC environment. However, the relatively low light yield (30γ/50 MeV) requires the use of photodiodes with an intrinsic gain, able to operate inside the high magnetic field of CMS. For this purpose, avalanche silicon photodiodes (APDs) are used in the barrel region and vacuum phototriodes (VPTs) are used in the endcaps.

The barrel part (EB) has a inner radius of 129 cm. It consist of 36 identical modules, each covering half of the barrel length and the interval $\eta < 1.48$. Crystals are disposed in a $\eta \times \phi$ grid, each with a length of 25.8 radiation length (230 mm) and a section of 22 $\times$ 22 mm^2, allowing a granularity of 0.0175 $\times$ 0.0175.
The endcap region (EE) is situated at a distance of 3.14 m from the IP and covers the pseudorapidity region $1.48 < \eta < 3.0$. Each endcap is structured in two semicircular aluminium plates containing 5 $\times$ 5 crystal modules disposed in a $x \times y$ grid. The EE crystals have a section of 28.6 $\times$ 28.6 mm^2 and a length of 24.7 radiation length (220 mm).
The highly collimated photon reconstruction is guaranteed by a fine granularity preshower device placed in front of the EE calorimeter. It consist of two planes of silicon strip modules with a pitch of 1.9 mm placed behind two absorbing lead disks of length respectively equal to 2 and 3 X_0. Since the expected rate of highly collimated photon, mostly coming from π_0 events, is lower in the barrel region, the EB detector does not have preshower modules.

The energy resolution of ECAL can be described by Eq. 2.5.

$$\left(\frac{\sigma_E}{E}\right)^2 = \left(\frac{2.28}{\sqrt{E}\ [GeV]}\right)^2 \% + \left(\frac{12}{E\ [GeV]}\right)^2 \% \tag{2.5}$$

where the first term is the stochastic term, the second term is the noise term and the last term is given by the non-uniformity of the longitudinal light collection and electronic calibration, and by the energy leakage from the back of the calorimeter.
Figure 2.7 shows the ECAL subdetector.

2.2.3 The hadronic calorimeter

The CMS hadronic calorimeter (HCAL) is a sampling calorimeter ed upon the necessity of minimizing the non-Gaussian energy distribution tail, providing a good estimation

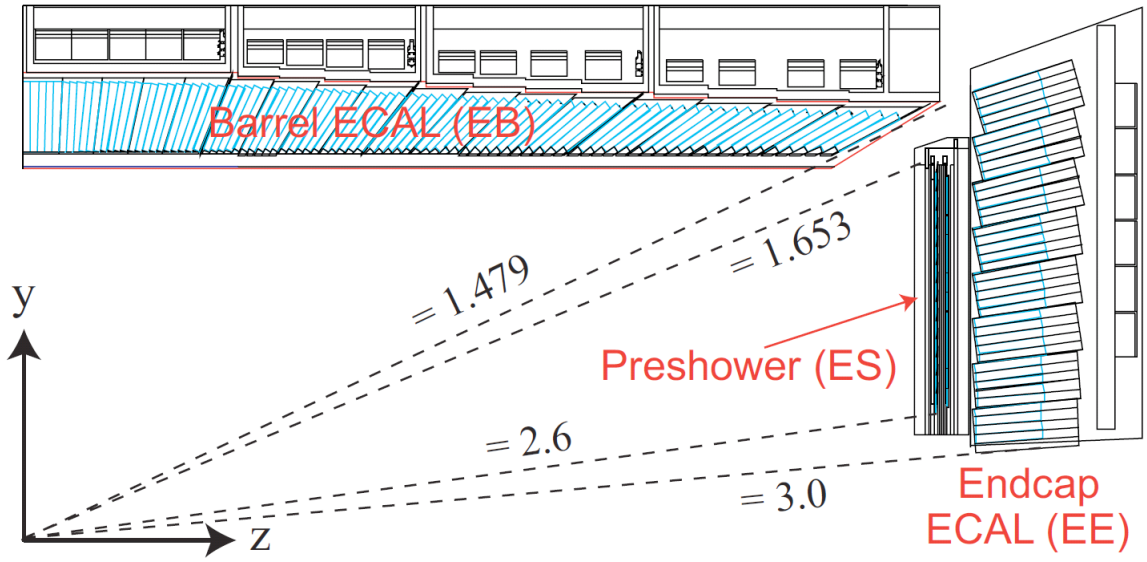

Figure 2.7: The CMS ECAL subdetector

of the missing transverse energy, whence the necessity to guarantee a good hermeticity [39]. Its properties are strongly bonded by the presence of the magnetic solenoid and the electromagnetic calorimeter. For these reasons, HCAL is designed to maximize the material inside the magnetic bore: brass has been chosen for the absorbing material, since it has a reasonably short interaction length and does not introduce inhomogeneities in the magnetic field, while scintillating plastic tiles with embedded wavelength shifters are chosen for the active mean.
Four different areas can be distinguished inside the HCAL: the barrel region, (HB), the hadron outer detector (HO), the endcaps detectors (HE) and the forward calorimeter (HF).

The HB consists of thirty-two modules of seventy-two towers each, covering the pseudorapidity region up to $|\eta| = 1.4$, built with a segmentation $\eta \times \phi = 0.087 \times 0.087$. The absorber consists of fifteen brass plates, each with a thickness of 5 cm, supported by two steel plates. The scintillation signal induced in the active mean is collected by optical fibres and sent to readout boxes, where the light signal is converted into an electric signal and amplified by hybrid photodiodes (HPDs).
The HO is a scintillation detector made by 10 mm thick modules situated outside the magnetic coil. It acts as a tail catcher, adding 10 interaction length to the barrel calorimeter, thus ensuring a better hermeticity and reducing the tails in the energy resolution distributions and improving the estimation of the missing energy. The HO covers the barrel region

between -1.26 $< \eta <$ 1.26. It is divided in 5 rings along the η coordinate, each formed by 12 section along the ϕ angle.
Th HE detector consist of 14 modules for a total of 2 304 towers disposed along the η coordinate for both endcaps. The eight innermost towers presents a 0.087 segmentation along both ϕ and η, while the remaining outermost towers present a 0.175 segmentation along ϕ and a 0.09 segmentation along η.
The HF calorimeter guarantees the coverage for the $3 < |\eta| < 5$ region. This detector is a sample calorimeter made of steel absorber plates and quartz scintillating fibres, arranged in 18 wedges and disposed in a cylindrical shape with a segmentation of 0.175 $\times$ 0.175, positioned at $|z|$ = 11.2 m.

The energy resolution of the hadronic calorimeter is given by Eq. 2.6.

$$\begin{aligned} \left(\frac{\sigma_e}{E}\right)^2 &= \left(\frac{90\%}{\sqrt{E\ [GeV]}}\right)^2 + (4.5\%)^2 \quad (HB\ and\ HE) \\ \left(\frac{\sigma_e}{E}\right)^2 &= \left(\frac{172\%}{\sqrt{E\ [GeV]}}\right)^2 + (9\%)^2 \qquad (HF) \end{aligned} \tag{2.6}$$

2.2.4 The muon system

Muon detection is one of the CMS most important tasks. In many events, such as electroweak or heavy flavour decays, muons are present in the final state. Given the peculiar sign that they leave in the CMS detector, muons play an important role in the CMS physics.
As muons can penetrate several meters of material without interacting, they are able to reach the outer part of the detector, situated outside the magnetic coil and inside the magnetic yoke, without being stopped by the calorimeters or the yoke itself.
The muon system has three functions: measuring the muon momentum, identifying the muons and triggering the events containing muons.

The choice of the detector technologies has been driven by the large amount of surface to be covered and by the different radiation environments. Indeed, three different types of gaseous detectors are used [56]

- 250 drift tubes (DT) in the barrel region, $|\eta| < 1.2$
- 540 cathode strip chambers (CSC) in the endcaps, $0.9 < |\eta| < 2.4$
- 610 resistive plate chambers (RPC) in both regions, $|\eta| < 1.6$

The DT are organized in four stations, labelled, starting from the innermost station, as MB1, MB2, MB3 and MB4, and placed inside the magnetic yoke at a radii of approximately 4.0 m, 4.9 m, 5.9 m and 7.0 m. Each station consists of eight layers of drift chambers. The first three station present a total of sixty drift chambers, while the outermost station has seventy drift chambers. Each chamber has an average size of 2×2.5 m^2 and it's constituted by drift tubes containing a wire within a gaseous volume. The basic element of the DT detector is a 42×12 mm^2 cell with a gold plated stainless steel anode wire in the centre operating at 3 600 V. Each cell is filled by a mixture of Ar and CO_2, which provides a good quenching property and a drift velocity of 55 µm ns^{-1}. The first three station can measure both the muon position in the $r-\phi$ bending plane and in the z coordinate, while the last station only measures the $r-\phi$ position. The spatial resolutions ranges from 80 μm to 120 μm.
The endcap region presents a less uniform magnetic field. In this area, CSC are used, since they allow a finer segmentation and have a shorter response time. As a result, CSC are less sensitive to this inhomogeneity. Each endcap has four stations mounted perpendicular to the beam, where the cathode strips run radially outward, while the anodic wires run perpendicular to them, allowing a three dimensional measurement of the muon position ($r-\phi$ plane and z coordinate), for an overall position resolution of 40-150 µm.
The RPCs provide a complementary and trigger dedicated detector system with an excellent time resolution, also able to solve the CSC reconstruction ambiguities. They are double-gap chambers, operating in avalanche mode to ensure a good operation at high rates. The RPC spatial resolution (0.8-1.2 cm) is worse than the DT and CSC resolution, but the excellent time response (2 ns) provides efficient bunch crossing assignment even in the high rate background of LHC.
The muon station geometry is shown in figure 2.8.

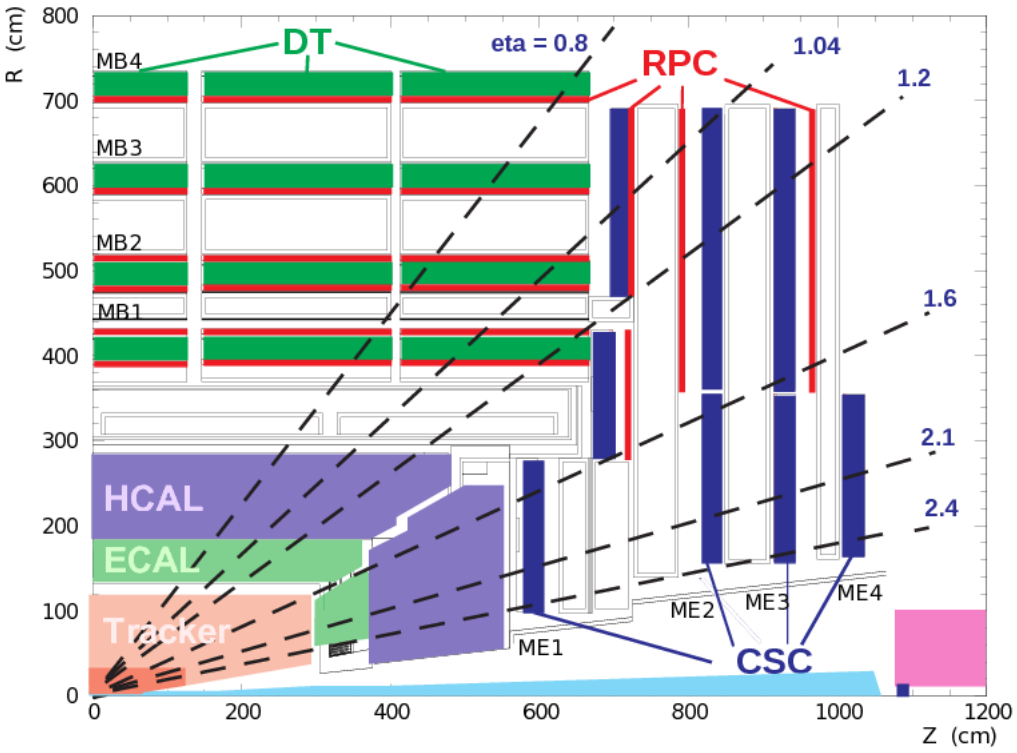

Figure 2.8: The CMS muon stations in the z-r view

2.3 Particle reconstruction

Particle identification is a critical issue in data analysis. The CMS apparatus shows properties particularly suited to the particle flow (PF) reconstruction: a highly segmented tracker, a fine-grained electromagnetic calorimeter, a hermetic hadron calorimeter, a strong magnetic field, and an excellent muon spectrometer are the characteristics that allow the PF algorithm to enhance the particle measurement and identification. For each collision, the PF reconstruction provides a global event description that greatly improves the hadronic jet reconstruction, the missing transverse energy determination, and the muon and electron identification.

The PF algorithm exploits the exclusive traces left by different particles inside the CMS detector. Starting from the IP, a particle first enters the silicon inner tracker, in which charged particles trajectories are reconstructed through the hits left in the detector and their momentum is calculated thanks to the high magnetic field.
Photons and electrons are then absorbed by the electromagnetic calorimeter, where different processes such as bremsstrahlung radiation and pair production contribute to the formation

of the electromagnetic showers. Those showers are detected as clusters of energy deposits, which allow to determine the particle energy and direction. Charged and neutral hadrons are absorbed by the hadron calorimeter.
Muons and neutrino escape the inner part of the detector, leaving the steel magnetic yoke almost unperturbed. While neutrino do not leave a trace inside the CMS detector at all, giving rise to missing momentum, muons produce additional hits inside the external muon stations. A pictorial representation if this process is shown in figure 2.9.

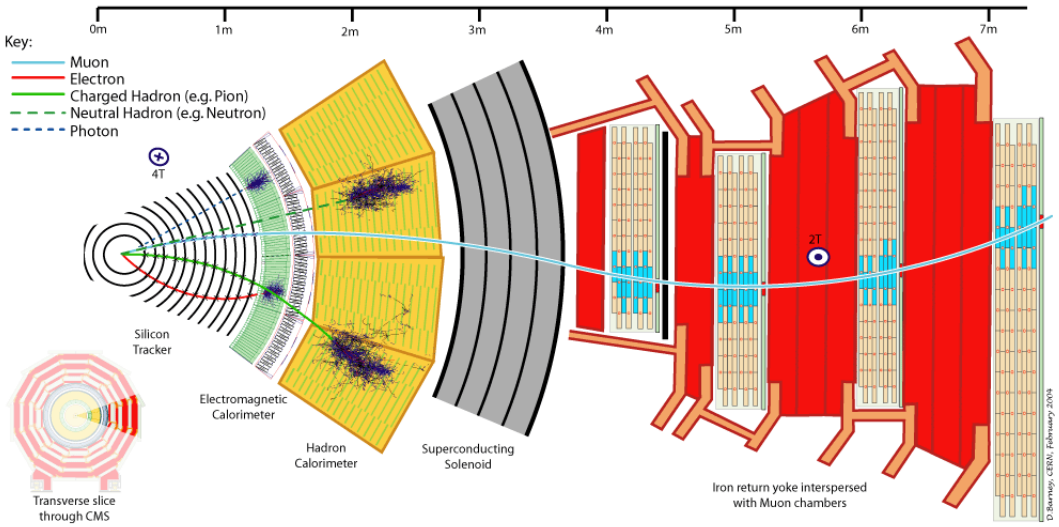

Figure 2.9: Particle interaction inside the CMS detector

The apparent semplicity and modularity of the CMS detector lead to a definition of physical objects that is, to a large extent, mostly based on the signal coming from specific detector areas [57]:

- Jets consists of hadron and photon ensambles, whose properties can be measured by the calorimeters without any contribution from the tracker or the muon stations
- Isolated photons and electrons reconstruction concerns the ECAL
- τ and b jets identification mostly involves the tracker
- Muon identification is based on the trace left in the outer muon chambers

A significantly improved event reconstruction can be achieved by correlating the basic signals coming from all the detector layers, combining those information to reconstruct the particle properties.

2.3.1 The particle flow

A particle is expected to give rise to several distinct traces inside the CMS detector . The goal of the PF algorithm is to correlate those information and generate a better description of the event [57]. This is done linking the signals coming from the different subdetectors, such as tracker hits and colorimetric clusters. Once a link is found between two elements, the algorithm defines a distance between the two, in order to quantify the quality of the link. In order to reduce the computational time, the link procedure only considers neighbours elements in the $\eta - \phi$ plane, since the computing time grows quadratically with the number of particles.

The links between the tracker and the calorimeters are obtained extrapolating the tracker trajectories to the preshower layers, to the ECAL calorimeter at a depth corresponding to the expected maximum of a electronic shower, and to the HCAL at a depth corresponding to one interaction length. A track is linked to a cluster if it falls inside the cluster area, defined by the cells activated by the energy deposit. This area is enlarged in every direction by the size of a cell to mitigate the systematic effects that arises from the choice of the interaction depth, the multiscattering, and the presence of possible gaps or cracks between the calorimeter cells. The distance between the track and the clusters is defined in the η-ϕ plane for the barrel region and in the *x*-*y* plane for the endcap regions; in case multiple clusters are activated by the same event, only the smallest distance is considered. To count for bremsstrahlung photons, tangent trajectories are extrapolated from the tracks to the ECAL. If a match is found and its distance from the main cluster is sufficiently small [57], a cluster is then linked. A dedicated routine looks for possible pair productions originating from the bremsstrahlung photons.
Charged particle tracks can be linked together through a common secondary vertex if at least three tracks can be related to the same vertex, among which one is the incoming particle, and their invariant mass is higher than 0.2 GeV.
Calorimeter links are sought between the preshower clusters and ECAL clusters, and between ECAL clusters and HCAL clusters. A link is established when the more granular calorimeter cluster (preshower or ECAL) is within the cluster envelope of the less granular calorimeter (ECAL or HCAL).
Links between the inner tracker and the outer stations are established to take account of muons.

The set of links found by the PF algorithm in the event is called PF block. For each PF block, the reconstruction start from the identification of muons, as described in section 2.3.1. The electron identification follows, at the same time of the photon identification.

At every step, the corresponding PF elements are removed form the picture. At this point, tracks with a pt resolution worse than the calorimetric energy resolution are discarded in order to reduce the mis-reconstructed tracks. The remaining elements are then subject to hadron and hadron-originated-particles (such as photons arising from parton fragmentation) identification.

Muon reconstruction and identification

The strategy for physics analyses in CMS is based on the reconstruction of high-level physics objects which correspond to particles travelling through the detector. The detector components generate a signal every time they are traversed by a particle; those signals identify points in space called hits, which are used to reconstruct the particle track and its characteristics, such as the momentum, the charge and different identification tags [58].

The muon reconstruction chain starts with the local reconstruction, that is, the reconstruction of hits inside the DT, CSC and RPC detectors to generate segments. During the off-line reconstruction, these segments are used as seeds in the estimation of the muon direction and transverse momentum. The result is an object referred as *standalone muon*. For each standalone muon, a match is sought among the silicon tracker tracks. To do so, tracker and standalone tracks are extrapolated to a common surface and the goodness of the match is defined upon some discriminating variables, such as the compatibility between the momenta or between the $\eta - \phi$ position [58]. Once a match has been found, a new track is fitted using the information coming from both the inner and outer detector, generating a new object called *global muon*.
An approach complementary to the global reconstruction can be employed if informations coming from the inner silicon tracker are used as first seeds. In this case, every silicon track is considered a potential muon candidate, and compatible signatures are sought inside the calorimeters and the muon system. The inner track is indeed extrapolated to the ECAL first, and then to the muon station, and the compatibility with a minimum ionizing particle is checked in those detectors. Muon identified by this procedure are referred as *tracker muons*. This method can successfully reconstruct muons with a low p_T , which would not leave consistent traces inside the outer stations, eluding the global reconstruction [59].
As mentioned in section 2.3.1, muon reconstruction can be achieved by the PF algorithm, where global and tracker information are used. Isolated global muons are first selected and matched to additional inner tracks and calorimeter deposit close to them in the $\eta - \phi$ plane. An isolation criterion is applied to those candidates, requiring the sum of the tracks p_T and the calorimeter energies to be less than 10% of the muon p_T . This

criterion is sufficient to discard hadrons that would otherwise be misidentified as muons; no further selection is applied to those candidates.
For non isolated global muons, a tight selection, as described later in this section, is applied. In addition, it is required that at least three matching track segments are found in the muon detector or that the calorimetric deposit associated to those global muons is compatible with the muon hypothesis.

Based on the reconstructed informations, some additional tags can be defined [60]

- **loose muon ID**. This selection requires the muon to be either a global or tracker muon.
  This criterion is designed to be highly efficient with prompt muons, as well as with muons coming from heavy and light quark decays.

- **medium muon ID**. The medium muon ID adds further requirements on the track of a loose muon. The medium ID is assigned to loose muons with a fraction of valid tracker hits greater than 0.8. In addition, the muon is required either to be a *good global muon* or have a tight segment compatibility [60].
  This selection is designed to be efficient with prompt muons and with muons coming from heavy quark decays.

- **tight muon ID**. This selection requires a global muon with a track χ^2 smaller than ten, segments in at least two muon stations, a transverse impact parameter smaller than 2 mm and a longitudinal distance smaller than 5 mm with relation to the primary vertex, and at least five tracker hits.

- **soft muon ID**. This selection requires at least one muon segment in the outer stations, at least five tracker layer hits, among which at least one pixel hit, and a high-purity quality of the track [54]. This selection is optimized for low-p_T muons for B-physics and quarkonia analyses

2.4 The CMS trigger

The trigger system plays a fundamental role in the CMS experiment, as it help the identification of interesting physical processes among the moltitude of proton-proton interaction products. At the LHC, the event rate is largely dominated by soft proton-proton interactions with low transverse momentum. The trigger is therefore designed to exclude these type of events, taking decisions based on the information coming from the

CMS subdetectors.
The trigger ssytem also permits to save only a selected portion of events to the mass storage. With an average of 25 inelastic collisions per bunch crossing and a bunch crossing every 25 ns, events are generated at a frequency of 40 MHz with the approximate size of 1 MB. The data writing capacity should be of the order of 10 TB s^{-1}, considerably exceeding the modern data storage capabilities [61].

The acquisition rate is reduced to about 40 MB s^{-1} using two different trigger layers. The first, called Level 1 (L1) Trigger, is a hardware trigger, designed to reduce the rate down to 100 kHz. The second, the High Level Trigger (HLT) is a software trigger that is designed to further reduce the rate to 1 kHz.

2.4.1 The Level 1 Trigger

The L1 trigger is a hardware trigger working at a fixed latency. Within 4 μs, the system must decide if an event should be accepted or rejected using the information coming from the muon detectors and the calorimeters.
The first level fo decision is made after a fixed time from the interaction on a subset of information available for the event. Considering that a new event must be accepted every 25 ns, the full data are temporarily store in pipelines of processing elements before arriving at the L1 hardware. Since that the total time used to store the event must not exceed 3.2 μs, a maximum of 128 bunch crossing can be saved. The remaining time, about 1 μs, is dedicated to the effective decision. Given the small amount of time available to make the decision, the L1 trigger cannot read the whole CMS feedback, and it must rely on simple information coming from the calorimeters and the muon stations. The tracker is excluded from the L1, since the information that it provides is too sophisticated to be analysed in such a small period of time. The L1 is organized in three major subsystems: the Calorimeter Trigger System, the Muon Trigger and the Global Trigger, as shown in figure 2.10.

The first computation step of the Calorimeter Trigger System is performed by the Trigger Primitive Generator (TPG), which interacts directly with the ECAL and HCAL front-end electronic system. Data coming from the calorimeters are used to generate primitive objects such as photon, electrons, muons and jet candidates, as well as the identification of MIP-like clusters, subsequently sent to the Muon Global Trigger. As already stressed, the L1 must rely on fast decisions in order to keep up with the LHC collision rate. For this reason, the informations coming from the ECAL do not exploit the high granularity of the detector entirely, but are defined upon 5×5 crystal elements called towers.

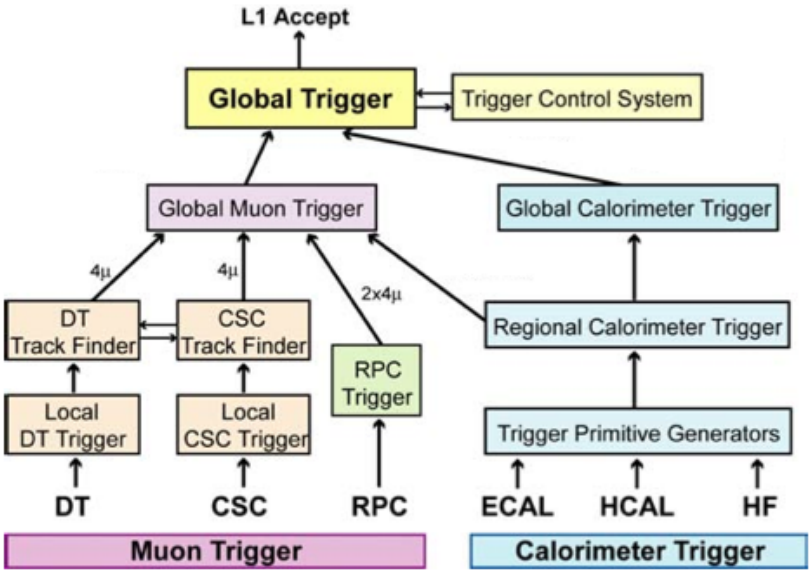

Figure 2.10: The CMS L1 trigger main structure

The TPG information is transmitted to the Regional Calorimeter Trigger (RCT), that classifies and sorts the best candidates among isolated photons and electrons, central and forward jets, and tau jets. The RCT transmits the information to the Global Calorimeter Trigger (GCT), the final element of the calorimeter trigger chain. The GCT goal is to do a final sorting of the candidates received by the RCT and calculate the missing energy of the event. The GCT selects four candidates among isolated and non-isolated electrons and photons, τ candidates, central and forward jets, sending also information about the total number of jets and the missing energy value and direction of the event [61] [62].

The muon L1 reconstruction

The muon trigger processes data coming from the outer stations. Starting from DT, RPC and CSC information, a module called Local Trigger reconstructs track segments and vectors. Vectors from different stations are collected by the Track Finder (TF), which combines them to extrapolate the muon tracks and calculate their momentum. The four best recognized muon candidates are sent to the Global Muon Trigger (GMT). Differently from the DT and CSC, the RPC information are not processed by a local and TF module, but if their hits are aligned along a possible muon track, a p_T value is assigned and the four best candidates are sent to the GMT. The GMT combines the informations coming from the single subdetectors modules, removing and merging the possible duplicates, calculating the correct p_T and position of those tracks and assigning

the muon candidates a quality code. The GMT also receives information from the GCT, thus being able to associate isolation information to the muon candidates. The best four muons, selected based on their quality and momentum, are sent to the Global Trigger [61] [62].

The Global Trigger (GT) is the final step of the L1 Trigger system. For every LHC bunch crossing, the GT decides whether to reject or accept a physics event for subsequent evaluation by the HLT. This decision is based on trigger objects coming from the L1 muon and calorimeter systems, which contain information about transverse energy E_T, transverse momentum p_T , location (pseudorapidity and azimuthal angle), and quality. The GT event selection is achieved via the *menu* of the trigger. The menu is a sequence of selections, combined by simple logic operators (AND-OR-NOT) to form algorithms and applied on the final list of triggered data processed by the CT and MT; the algorithm are combined with an OR-function, thus generating the final L1 signal. The rates of the L1 Trigger can be kept under control by adjusting the energy and momentum thresholds, or prescaling the trigger algorithms relative to processes with a large cross section [61] [62].

2.4.2 The High Level Trigger

The upper level of real time data selection is called High Level Trigger (HLT). The HLT is designed as algorithms running in parallel in a dedicated farm of commercial processors. As first functionality, the HLT has to perform the readout of the front-end electronics after the Level 1 Trigger accepts the event. The HLT trigger was designed upon three simple requests [63]

- having access to data that, except for the calibration constant used by the HLT, is essentially of offline quality
- having access to data originating from any part of the detector, without any restriction from the physical connection of the detector elements
- full algorithmic flexibility, without any limitation arising from the programming language, instruction sets, or any other limitation of sort

The first request is satisfied, since the data given to the HLT processors are the full raw data contained in the front-end electronics, without any loss of information that could arise from digitalization or information merging. The second request is also satisfied, since each processor is connected, by design, to all the detector elements of CMS, and can therefore access any data it deems valuable for the event selection and reconstruction.

The third request is satisfied, too, since the HLT farms is composed by commercial processors running a version of Scientific Linux [61].
The filtering process uses the full data from all the detector: it is based on better granularity and resolution informations from the inner tracker. As a result, the HLT preforms the full reconstruction and selection of physical objects assimilating and matching the full information available from all the different subdetectors. Up today, the HLT computational power allows L1 input rates as high as 100 kHz, being able to process an event every 175 ms [61].

The data processing of the HLT trigger is structured around the concept of the HLT *path*, which is a set of algorithmic processing steps run in a predefined order, used to both reconstruct and select the physical objects. The reconstruction modules and selection filters of the HLT use the software framework that is also used for offline reconstruction and analyses. Significant physics decisions needs to be taken at the HLT level: the rate of accepted events must be as low as what the current technology allow to write on disk, which is about 400 Hz.
The basic event building strategy is to reconstruct those parts of each physic object that can be used for selection while minimizing the overall CPU usage. This goal is achieved with two different techniques: the regional reconstruction and the development of different trigger levels.
To minimize the CPU required by the HLT, a key feature of the algorithms is to reconstruct the information in the CMS detector only partially. In many cases the decision on whether an event should be accepted by the HLT involves the reconstruction of quantities in only a limited region of the detector. As an example, for an event accepted by the Level 1 trigger in the inclusive muon stream, only the parts of the muon chambers indicated by the Level 1 trigger results and the corresponding road in the tracker need to be considered for the validation of the muon. This approach is made possible by the transmission of the location coordinates of the trigger objects in the L1 system. Also, the implementation of the HLT through the computer farm guarantees freedom in the selection of the data and easiness in their handling.
The reconstruction and selection in the HLT takes place in steps which correspond roughly to what would have been distinct trigger systems: the Level 2, Level 2.5 and Level 3 trigger systems. The CMS HLT architecture does not include a sharp division between these trigger steps, other than the order in which they are applied. Each step implements a series of selection algorithms of increasing complexity, performing specific tasks. The Level 2 step, which undergoes the highest event rate, relies only on information from the calorimeter and muon detector. In contrast, the Level 3 refers to the whole event information, including the reconstruction of the tacks in all tracking detectors. The Level

2.5 step uses only partial tracking information, such as pixel hits, for a fast confirmation of the electromagnetic candidates.
Only data that survive all the trigger levels are accepted and subsequently stored for the offline analysis, exception made for some portion of data which is saved from the HLT rejection and reserved for the trigger calibration and to ensure a complete and accurate understanding of the detector.

The muon HLT reconstruction

Events selected by the L1 trigger are passed to the HLT, which uses information from the full CMS detector to reconstruct muons. Level 1 muon candidates are used as a seed to reconstruct muons at Level 2 using information only from the muon detectors and the *beamspot* position (this reconstruction is identical to the offline *standalone* reconstruction). L2 muon trajectories are extrapolated to the inner tracker, looking for a compatibility between the muon track and a tracker track or hit. In case a match is found, the tracker and muon tracks are combined to build the L3 trajectory [64]. This combination is made using three algorithms applied sequentially from fastest to slowest, and subsequent algorithms are attempted only if the previous one failed to reconstruct a muon in order to minimize computation time.
The first algorithm propagates the L2 trajectory inward to the inner tracker to reconstruct the L3 muon. The second algorithm is similar to the first, except that it combines the L2 muon with hits in the outer layer of the inner tracker to improve its trajectory before propagating it inward. The third algorithm is different from the first two in that it builds tracker tracks with an inside out approach within a region based on the position of the L2 muon [65].
After reconstruction, the muon isolation is evaluated in HLT by considering the additional tracker tracks and calorimeter energy deposits in a cone $\Delta R < 0.3$ around the muon: each of the contributions is required to be below a fraction of the muon p_T .
For the double-muon triggers, the L3 algorithm is first used to reconstruct one muon. In order to save computing time, this L3 muon must pass pT and quality constraints before the reconstruction of a second muon is attempted. The second muon can be reconstructed with either the L3 or the HLT tracker muon algorithm to maximize efficiency. Tracker track isolation criteria are then applied to both tracks [65]. A pictorial representation of the detector areas involved in the HLT reconstruction is shown in figure 2.11.

Alternatively, an unseeded reconstruction can be performed using the information coming from the tracker. The HLT unseeded tracker muon reconstruction is a particular reconstruction strategy that looks for a muon independently from the presence of a L1 muon candidate.

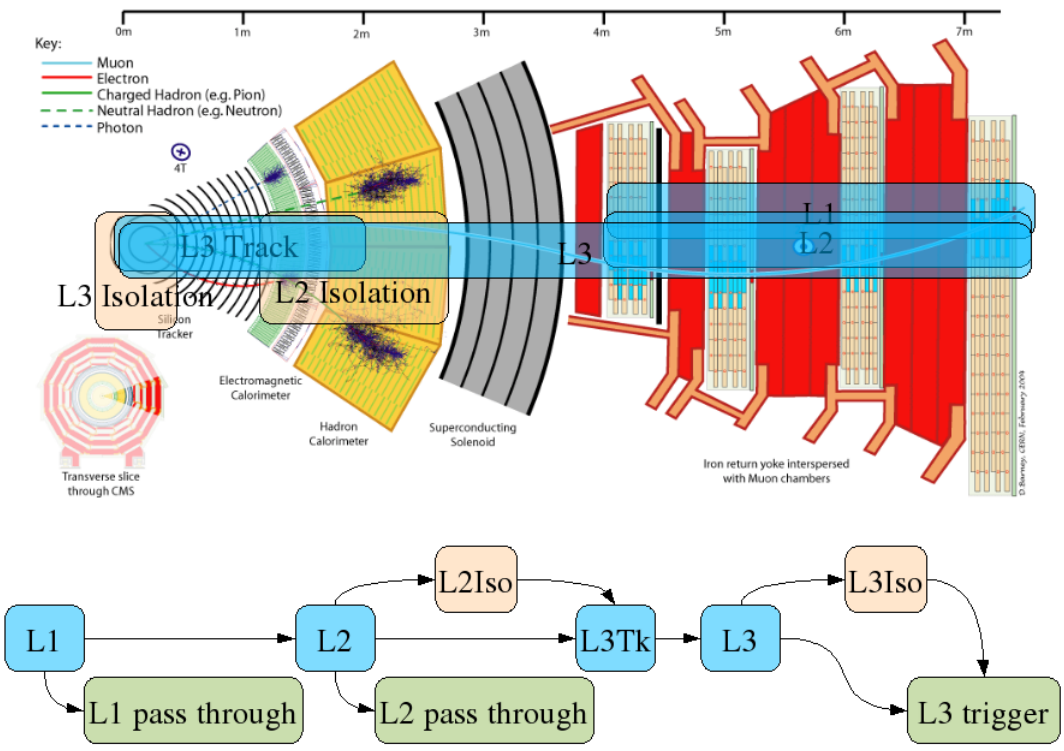

Figure 2.11: Detector areas involved in the various HLT reconstruction steps of the muon objects

A simplified track reconstruction in the whole tracker detector is first performed, followed by the matching of the tracker track to at least one hit in the muon stations. This procedure allows to recover eventual L1 inefficiencies intrinsic to the L1 reconstruction itself, especially for low p_T and collimated muons.
The unseeded tracker muon reconstruction is highly CPU consuming, and therefore cannot be run in parallel with the standard L3 muon reconstruction. Consequently, it is used only in those trigger paths where some tight selection is already applied.

Chapter 3

Search for $\tau \to 3\mu$ events in 2017 and 2018 data

This chapter describes the search for the $\tau \to 3\mu$ process in proton-proton collision data collected by CMS during 2017 and 2018. First, the search in the W production channel is described; then, the search in the *heavy flavour* (HF) production channel is briefly described. In the end, the combination of the two channel, together with the results from the 2016 analysis [5], is illustrated.
The final result is given in terms of the *expected upper limit* on the branching fraction of the $\tau \to 3\mu$ process, computed on the blinded data sample, as at the time this thesis was written the analysis was still under CMS internal review.
To conclude, the projection of the search for the $\tau \to 3\mu$ process in the near future at hadron colliders and B-factories is outlined.

3.1 The W channel analysis

The $W \to \tau\nu$ production channel (from here on, the *W channel*) represents an essential and unavoidable contribution to the τ lepton production in the context of the search for the $\tau \to 3\mu$ rare process at CMS; due to the harder spectrum of the muon momenta (if compared to the complementary *heavy flavour* channel), to the large missing transverse momentum, and to the better isolation of the signal tau lepton, its final state is most suited to trigger selections and signal identification at the CMS detector, thus compensating for the smaller production rate. My analysis on the $\tau \to 3\mu$ search in proton-proton collision data collected by CMS during 2017 and 2018, using τ leptons originating from $W \to \tau\nu$ decays is described. The criteria adopted to collect, manipulate and tag events are illustrated in the following sections, and are summarized below.

The first step of event selection is done online by a dedicated HLT path. During 2016, the same trigger path was used to select events for the W and HF analysis. As its clear from Tab. 1.3, most of the L1 seeds used by the trigger were limited to the central region of the detector (mostly $|\eta| < 1.6$). This choice was made to reduce the rate of acquisition of the trigger, constrained by bandwidth limitations, in the context of the HF analysis on 2016 data. It was however clear that the signal from $\tau \to 3\mu$ decays, whether from W bosons or heavy mesons, has a fair contribution in the forward region (about 50% for $|\eta|$ > 1.5, see Fig. 3.1). For this reason, a new version of the HLT path was developed for the 2017 and 2018 data taking, specifically designed to target W channel events. The new trigger exploited the characteristics of τ leptons coming from a W boson decays, namely the presence of three well-reconstructed signal muons with good isolation properties, to reduce the rate and allow mitigate the pseudorapidity restrictions. More details of the new version of the trigger are discussed in the 2017-2018 analysis section (see Sec. 3.1.1).
After the trigger selection, data are pre-selected offline to form $\tau \to 3\mu$ signal candidates, as described in Sec. 3.1.2. The pre-selection stage applies mild requirements on the final state properties and the signal-background separation is entrusted to a Boosted Decision Tree (BDT), as explained in 3.1.4. My work on the 2016 data proved this strategy to be an excellent way to reduce the background contamination and it was adopted also in the 2017-2018 analysis.
As the $\tau \to 3\mu$ would manifest as a peaking structure around the τ lepton mass, a particular attention is reserved to the possible sources of structured background populating the analysis phase space (namely, D meson decays); these studies are described in Sec. 3.1.5.
Finally, the statistical treatment adopted to compute the sensitivity of the experiment to the $\tau \to 3\mu$ process is describe in 3.1.6, and the result obtained using the W channel only is stated in Sec. 3.1.6.

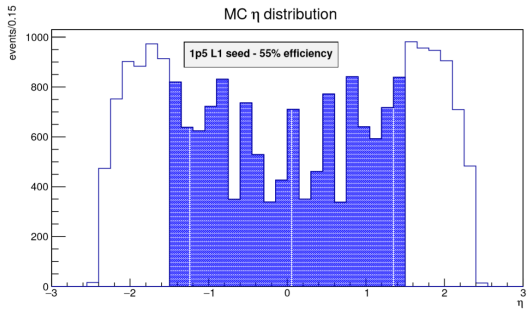

Figure 3.1: Pseudorapidity distribution of $\tau \to 3\mu$ signal events taken from a simulated sample. Events falling in the region $\eta < 1.5$ are shown with blue bars.

3.1.1 Trigger and data samples

The events used in the analysis are selected by the dedicated trigger HLT paths HLT_Tau3Mu_Mu7_Mu1_TkMu1_IsoTau15_Charge1 and HLT_Tau3Mu_Mu5_Mu1_TkMu1_IsoTau10_Charge1, which have been active since July 2017. The trigger was developed, also with my contribution, after the work on 2016 data showed the limitations of the previous version. The new trigger was designed to specifically to target $W \to \tau\nu$ events, exploiting the peculiar signature of the analysis, that is, the presence of three isolated muons in the final state of the decay. The trigger requirements are:

- one L3 muon with $p_T > 7$ GeV (or 5 GeV, depending on the trigger) and $|\eta| < 2.5$
- one L3 muon with $p_T > 1$ GeV and $|\eta| < 2.5$
- the invariant mass of the di-muon object should be lower than 1.9 GeV
- the radial distance $\sqrt{\Delta\eta^2 + ||\Delta\phi||^2}$ of the two muons should be lower than 0.5
- the distance along the z coordinate between the two muons should be lower than 0.3 cm
- one tracker muon with $p_T > 1$ GeV
- the tau object built with the three muons should have a $p_T > 15$ GeV (or 10 GeV, depending on the trigger)
- the isolation of the tau object should be lower than 2 GeV, its relative isolation lower than 0.2 (isolation is calculated as described in sec. 3.1.2)
- the invariant mass of the tau object should be between 1.3 GeV and 2.1 GeV, its pseudorapidity between -2.5 and 2.5

Additional versions of the main trigger paths were used, which do not require the tau candidate to be isolated. Due to hardware limitation, these triggers was switched on only every few events during data-taking, and are said to be *prescaled*. Table 3.1 shows the list of prescaled and unprescaled trigger paths used in the analysis and the corresponding integrated luminosity. Prescaled trigger paths are not employed to select the events for the final result computation, but were used for complementary studies (see Sec. 3.1.3).

The HLT paths are seeded by the logic OR of the L1 seeds described below:

- **L1_SingleMu22** : one L1 muon with $p_T > 22$ GeV

- **L1_SingleMu25** : one L1 muon with $p_T > 25$ GeV
- **L1_DoubleMu_15_7** : two L1 muons with $p_T > 15$ GeV and 7 GeV respectively
- **L1_DoubleMu4_SQ_OS_dR_Max1p2** : two opposite-charge L1 muons with $p_T >$ 4 GeV, track distance in the ϕ -η plane < 1.2
- **L1_DoubleMu4p5_SQ_OS_dR_Max1p2** : two opposite-charge L1 muons with $p_T > 4.5$ GeV, track distance in the ϕ -η plane < 1.2
- **L1_DoubleMu0er1p5_SQ_OS_dR_Max1p4** : two opposite-charge L1 muons with $p_T < 1.5$ GeV and $\eta < 1.5$ and a track distance in the ϕ -η plane < 1.2
- **L1_DoubleMu0er1p4_SQ_OS_dR_Max1p4** : two opposite-charge L1 muons with $\eta < 1.4$ GeV and track distance in the ϕ -η plane < 1.4
- **L1_TripleMu_5SQ_3SQ_0OQ_DoubleMu_5_3_SQ_OS_Mass_Max9** : three charge-one L1 muons with $p_T > 5$, 3 and 0 GeV, and the highest p_T muons must be opposite-charge muons and have an invariant mass lower than 9 GeV

Table 3.1: List of HLT trigger paths used in the analysis

Trigger name	Int. lum. [fb^{-1}]	Prescaled
HLT_Tau3Mu_Mu5_Mu1_TkMu1_IsoTau10_Charge1	3.42	no
HLT_Tau3Mu_Mu7_Mu1_TkMu1_IsoTau15_Charge1	86.95	no
HLT_Tau3Mu_Mu7_Mu1_TkMu1_Tau15_Charge1	1.77	yes
HLT_Tau3Mu_Mu7_Mu1_TkMu1_Tau15_Charge1	5.86	yes

The analysis is performed on data collected by CMS during the 2017 and 2018 proton-proton collisions at the centre-of-mass energy of 13 TeV, using the HLT triggers mentioned above.
The data format chosen for the analysis is the MiniAOD format [66], widely used in CMS. Proton-proton collision events are stored in c++ structures which collect detector and trigger information in vectors of high-level objects. The version of data including the final and best detector calibrations (called *Ultra Legacy* - UL) is used. The analyzed integrated luminosity is 30.54 fb^{-1} for 2017 and 59.83 fb^{-1} for 2018[1].

[1] This is about 6.7% less than the total 96.68 fb^{-1} collected by CMS in 2017 and 2018, as it encompasses only the period covered by the relevant triggers `HLT_Tau3Mu_Mu7_Mu1_TkMu1_IsoTau15` (active since July 2017) and `HLT_Tau3Mu_Mu5_Mu1_TkMu1_IsoTau10_Charge1`

The $W \to \tau\nu$, $\tau \to 3\mu$ signal process is centrally simulated with the software Pythia 8 [67], using the phase space model to generate the $\tau \to 3\mu$ decay, while using the SM description for the $pp \to W$ process. The process is generated using the CP5 tuning [68] (based on the Monash 2013 tune [69]) and the NNPDF3.1 [70] parton distribution functions.
The 2017 sample consists of 500000 generated events. The 2018 sample consists of 494200 generated events. The number of generated events is such to reduce the impact of the systematic uncertainty related to the size of the MC events to the percent range and to have a signal sample size comparable with the background sample size; these numbers were obtained assessing a signal efficiency of about 20%, inferred from the 2016 analysis.
Supplementary samples with artificial τ masses ranging from 1.65 GeV to 1.95 GeV[2] have been produced to improve the robustness of the BDT training (more in Sec. 3.1.4). These samples contain 50000 events each and are generated using the same parameters (except for the τ mass) and the same detector conditions as the nominal mass samples.
The background contamination is estimated purely from data events whose candidate lies outside the τ mass region (sidebands) and no MC sample is adopted for its modeling, as it would be hardly possible to simulate a large enough background sample which includes all possible contributions to the three-muon final state in a reasonable time.
Additional data and MC samples have been used to estimate scale factors and corrections applied to the simulated signal samples (see Sec.3.1.3). These samples includes data samples from events collected by *single-muon* and *double-muon* HLT paths, and $J/\psi \to \mu^+\mu^-$ and $D^\pm \to \phi\pi^\pm$ simulated samples. All the simulated samples have been produced using the same detector conditions and reconstruction campaign, to guarantee the consistency of the studies.

3.1.2 Signal candidate selection

Events with at least three offline muons in the full pseudo-rapidity range $0 < |\eta| < 2.4$ are selected. The MC simulation (Fig.3.2) shows that the p_T of the signal muons ranges as high as 50 GeV for the leading muon, and as low as a few GeV for the trailing one. Therefore, only a loose cut on the muon p_T is applied, which matches the detector muon acceptance ($p_T > 3.5$ GeV for $0 < |\eta| < 1.2$ and $p_T > 2.0$ GeV for $1.2 < |\eta| < 2.4$). Muon candidates are required to pass the medium quality identification criteria (see Sec. 2.3.1).

[2] 1.65 GeV, 1.70 GeV, 1.85 GeV, 1.90 GeV and 1.95 GeV.

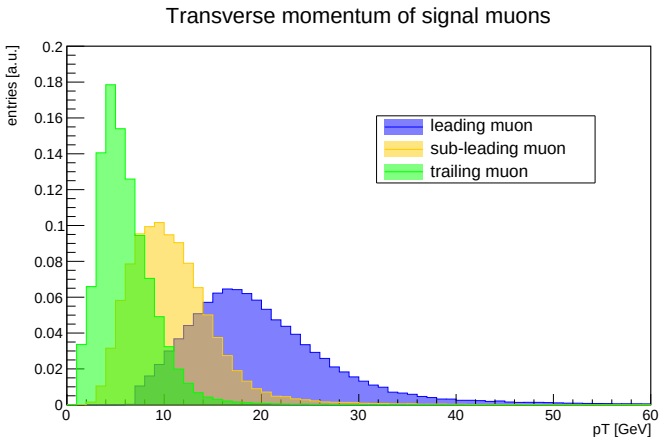

(a)

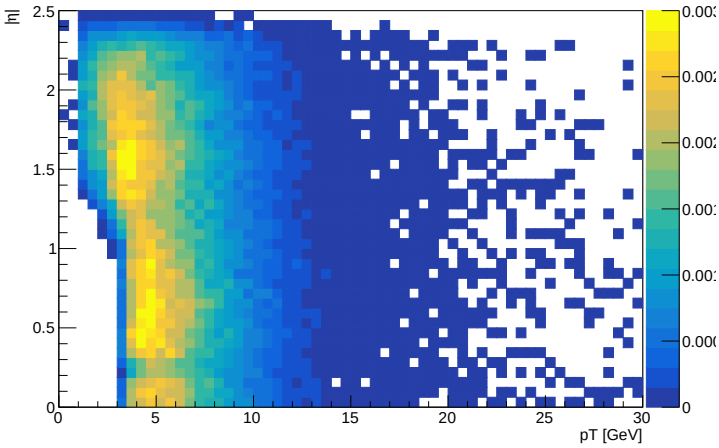

(b)

Figure 3.2: Reconstructed transverse momenta of μ_1, μ_2 and μ_3, where the three muons are sorted by p_T (a), and trailing muon p_T , $|\eta|$ distribution (b). Both plots refer to the 2018 signal MC sample.

Missing transverse momentum

The $W \to l\nu$ process is characterized by the presence of large missing transverse momentum (also improperly *missing transverse energy*, MET), which can be used as a handle to discriminate signal events from background. The missing momentum magnitude and direction in the transverse plane is determined by the PF algorithm, balancing the visible transverse momentum of the collision. A correction to the MET, based on a Deep Neural Network (DNN), is later applied.
This DNN, called deepMET, brings an improvement in the MET resolution for the primary event, if compared to the standard Pileup-per-particle-identification (PUPPI) [71] MET correction, commonly used in CMS, as shown in Fig. B.4. The PUPPI and deepMET corrections are described in App. B.

The τ candidate selection

Signal candidates are formed in each event by combining all the possible triplets of muons passing the pre-selection described above and being matched (in the η -ϕ plane) to the objects firing the trigger (for further details on the trigger matching, see Sec. 3.1.2). The invariant mass of the τ candidates should be lower than 3 GeV, and the τ candidate charge has to be equal to ± 1. A valid secondary vertex (i.e. with an associated fit probability greater than 5%), common ot the three muons, is required; the muon tracks are refitted, using this common vertex as a constraint, and the refitted parameters of the track are used in all the following steps of the analysis. Fig. 3.3 and Fig. 3.4 show the τ candidate invariant mass using the original or refitted muon quantities, respectively. The three-muon mass resolution improves by 4.3% in 2017 and 4.6% in 2018.

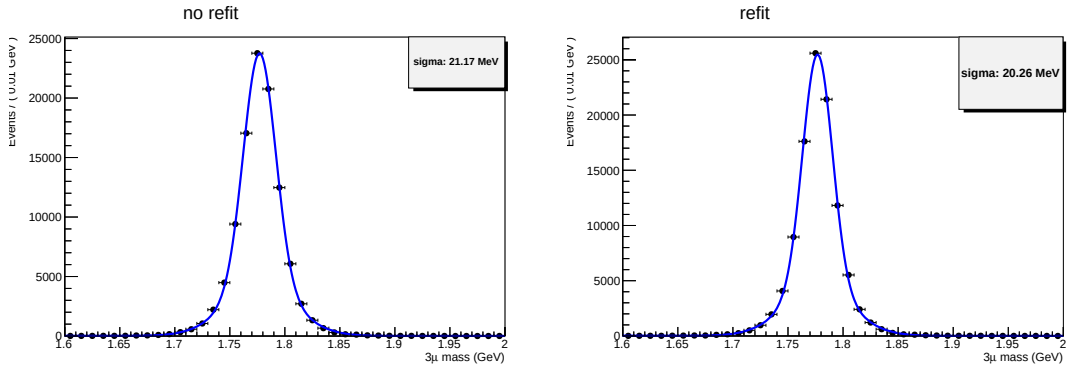

Figure 3.3: Three-muon invariant mass as reconstructed using the original muon four-momenta (left) or those calculated after the three-muon vertex fit (right) in the 2017 signal sample.

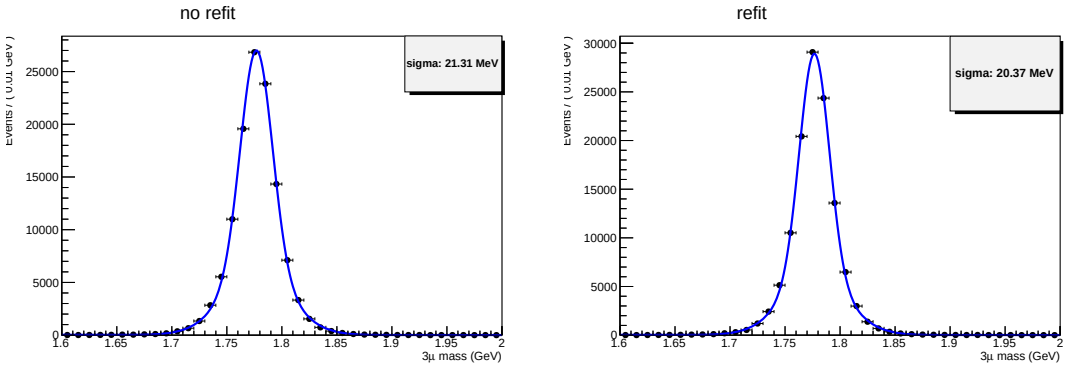

Figure 3.4: Three-muon invariant mass as reconstructed using the original muon four-momenta (left) or those calculated after the three-muon vertex fit (right) in the 2018 signal sample.

To reduce the contamination from the combinatorial background (that is, three muons not originated from a single process), signal candidates are discarded if any of the three muons shows a valid vertex[3] with an opposite charged muon not already considered as part of the signal candidate, and their invariant mass falls within 2σ from the nominal mass of the resonances listed in Tab. 3.2.

Finally, if more than one signal candidate per event is found, that with the largest transverse mass is retained[4]. The average number of candidates per event is shown in Fig. 3.5, and is 1.008 for signal MC events and 1.03 for data for both the 2017 and 2018 periods. The fraction of events with more than one candidate is 0.9% in MC and 4% in data for both the 2017 and 2018 periods. Different arbitration criteria have been tested: maximum p_T (best three-muon vertex probability, best isolation and maximum m_T); all have led to very similar probability of finding the correct candidate in a multiple-candidate signal event.

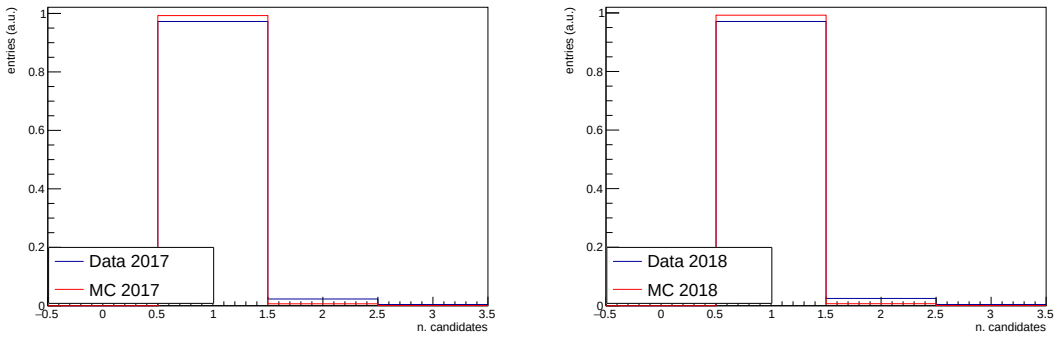

Figure 3.5: Average number of τ candidates per event, before arbitration, in data (blue line) and signal MC (red line) in 2017 (left) and 2018 (right).

τ candidate isolation

Leptons from W decays tend to have little or no hadronic activity surrounding them as opposed to leptons produced in charm and beauty meson and baryon decays.
To exploit this phenomenon, an isolation observable is defined as the sum of the transverse momentum of the tracks found in a cone of radius R=0.8 around the direction of the

[3]The vertex is considered valid if the probability derived from the track interpolation is larger than 5%.

[4]The transverse mass m_T is defined as $\sqrt{2p_T^\tau p_T^\nu \cos\theta}$, where p_T^τ is the transverse momentum of the signal candidate, p_T^ν is the missing transverse momentum and θ is the angle between the two in the transverse plane.

Table 3.2: List of vetoed resonances and values of the width considered for the 2σ exclusion. The width, in case of narrow resonances, corresponds roughly to CMS experimental resolution.

Resonance	Nominal mass [GeV]	σ [GeV]
η	0.5479	0.030
ρ	0.7753	0.075
ω	0.7827	0.030
ϕ	1.0195	0.030
J/Ψ	3.0969	0.030
$\Psi(2S)$	3.6861	0.030
Υ	9.4603	0.070
$\Upsilon(2S)$	10.0233	0.070
$\Upsilon(3S)$	10.3552	0.070
Z	91.1976	2.495

τ candidate and compatible within $\Delta z < 0.2\,\text{cm}$ from the primary vertex, excluding the three signal muons themselves, and the sum of the transverse momentum of the photons found in the same cone. Contributions to the second term from photons from pile-up collisions are statistically removed by subtracting an amount of energy proportional to the sum of the transverse momentum of tracks not compatible with the primary vertex, $\Delta z > 0.2\,\text{cm}$, that fall within the cone. The proportionality factor is $\Delta\beta = 0.2$ and it has been optimized in the context of the hadronic τ reconstruction [72] in order to maintain the efficiency to genuine leptons as constant as possible as a function of pile-up (Fig. 3.6). Furthermore, along with the absolute isolation described above, the relative isolation of the signal candidate is obtained by dividing the absolute isolation value by the transverse momentum of the τ candidate. The isolation variable is not used at pre-selection stage. Instead, it is passed to a multivariate discriminator (see Sec 3.1.4).
Equation 3.2 shows the mathematical definition of the relative isolation as described above.

$$I^{\text{abs}} = \sum p_{\text{T}}^{\text{charged}}(d_z < 0.2\ \text{cm}) + \max(0, \sum p_{\text{T}}^{\gamma} - \Delta\beta \sum p_{\text{T}}^{\text{charged}}(d_z > 0.2\ \text{cm})) \quad (3.1)$$

$$I^{\text{rel}} = I^{\text{abs}} / p_T^{\tau} \quad (3.2)$$

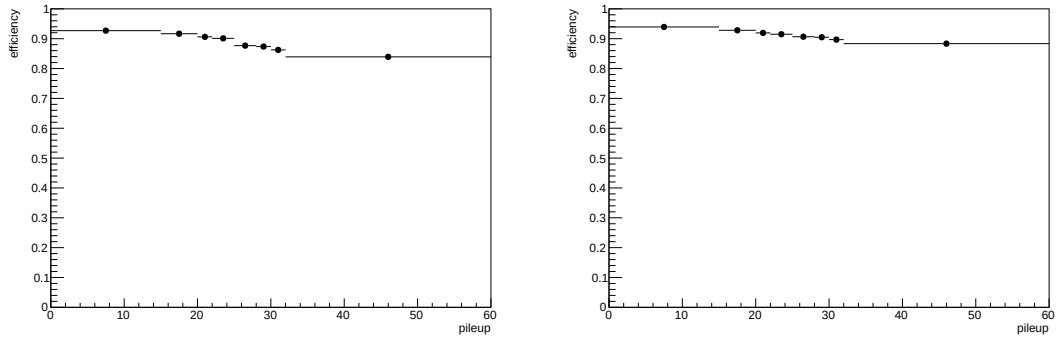

Figure 3.6: Efficiency to pass $I^{rel} < 0.2$ (relative isolation as defined in Eq. 3.2) for three-muon τ candidates as a function of the number of PU interactions as evaluated on the 2017 signal sample (left) and on the 2018 signal sample (right). A small loss can be observed at higher PU values, although mitigated by the $\Delta\beta$ correction

Longitudinal momentum of the neutrino

If on one hand the neutrino presence represents a good handle to discriminate W boson decays, due to the large missing transverse momentum it carries, on the other it makes

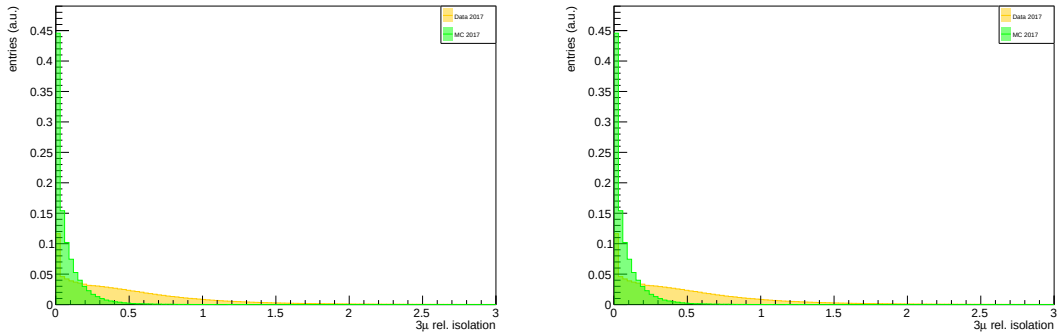

Figure 3.7: Tau relative isolation for 2017 samples (left) and 2018 samples (right). The background distribution (yellow) is obtained from data events in the signal mass sidebands ($1.6 < m_\tau < 1.74$ or $1.82 < m_\tau < 2.0$), while the signal distribution (green) is obtained from the simulation.

the closure of the W$\to \tau\nu$ kinematics not possible, as its longitudinal component, $\not{p}_z$, cannot be measured directly.
It is, however, possible to estimate the magnitude of the longitudinal component of the neutrino momentum solving the equation $E^2 = m^2 + p^2$, assuming $m = m_W$ (80.4 GeV). The equation results in the formula:

$$\not{p}_z^2(E_{3\mu}^2 - p_z^2) - 2A p_z \not{p}_z + (E_{3\mu}^2 \not{p}_z^2 - A^2) = 0 \tag{3.3}$$

where

$$A = \not{p}_x p_x + \not{p}_y p_y + \frac{1}{2}(m_W^2 - m_{3\mu}^2), \tag{3.4}$$

p_j are the components of the momentum of the three-muon final state, and the neutrino transverse components (x and y) are set equal to the event x and y components of the MET.
Eq. 3.3 has two solutions, both mathematically acceptable and used in the training. For about 30% of the signal events, the equation does not have real solutions due to the MET resolution. In such cases, the discriminant of the equation is set to zero, resulting in two coincident solutions.
As shown in figure 3.8, the distribution of these observables differs from data and MC, and can then be used for the signal-background discrimination.

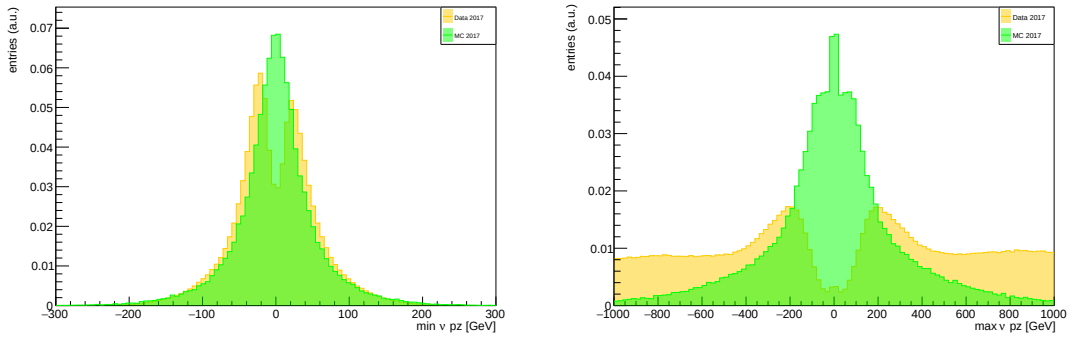

Figure 3.8: Distribution of the observables defined by the two solutions of Eq. 3.3, obtained on the 2017 background and signal samples. Signal events are shown in green, background events are shown in orange.

HLT matching

Trigger matching is performed to ensure that the selected muons correspond to the trigger objects which have fired the analysis HLT. The trigger matching is performed between

the objects identified by the offline reconstruction and the objects identified by the trigger reconstruction. The distance between two objects is defined as dR = $\sqrt{\Delta\phi^2 + \Delta\eta^2}$, η being the pseudorapidity of the object and ϕ its azimuthal angle coordinate. The threshold dR < 0.1 is chosen as matching criterion.
The three signal muons selected by the offline pre-selection (as described above) are matched to the three of the muons reconstructed and selected by the trigger during the data acquisition. Moreover, the sum of the offline four-momenta (the τ candidates) is also matched to the $\tau \to 3\mu$ HLT object.
An event is considered matched if the offline signal muons and τ candidate are matched to unique trigger objects.

3.1.3 Simulation corrections

As the analysis relies on simulated MC samples to describe the signal process, it is necessary to ensure that such samples correctly describe the data taking conditions and the reconstruction efficiencies observed on real data.
Various sources of mismodeling have been taken into account, and the corresponding per-event weights have been calculated. The sources of disagreement considered for the study are: the distribution of the number of primary vertices, the muon reconstruction and identification efficiency, the trigger isolation efficiency and the W transverse momentum and pseudorapidity spectra.
The scale factors (SF) obtained from these studies are used to re-weight the MC sample event per event, and the procedure used for their computation is explained in the following sections.

Pileup weighting

At CMS, interaction vertices are identified using tracks clustered with the deterministic annealing algorithm [73]. The average number of proton-proton interaction registered by CMS during the 2017 and 2018 runs is 32. Among these, the vertex with the highest sum of p_T^2 of the associated tracks is selected as the leading primary vertex, while the other vertices in the event are considered to be originated from the pile-up collisions (see Sec. 2.1).
Although the simulated samples are generated to roughly cover the data-taking conditions, the distribution of reconstructed vertices is sensitive to the details of their reconstruction, to differences in the underlying events in data and MC, and to the offline and online event selection criteria, so that the distribution of the number of interaction vertices in the Monte Carlo samples does not exactly match that of the data. To achieve a better agreement between data and simulations, the true distribution of primary vertices[5] is re-weighted to the one expected from data. The former can be easily obtained by the MC simulations, the latter is computed from the instantaneous luminosity measured by CMS in each lumi-section[6], assuming a proton-proton cross-section of 69.2 mb.

Figure 3.9 shows the distribution of the number of primary vertices in data and MC for the 2017 and 2018 datasets, and their ratio.

[5]The true distribution of vertices is used instead of the observed one in order to reduce the bias deriving by reconstruction of the vertices. This reconstruction has an efficiency of about 70%

[6]A lumi-section is the CMS fundamental unit of time for luminosity calculation, about 23.3 seconds.

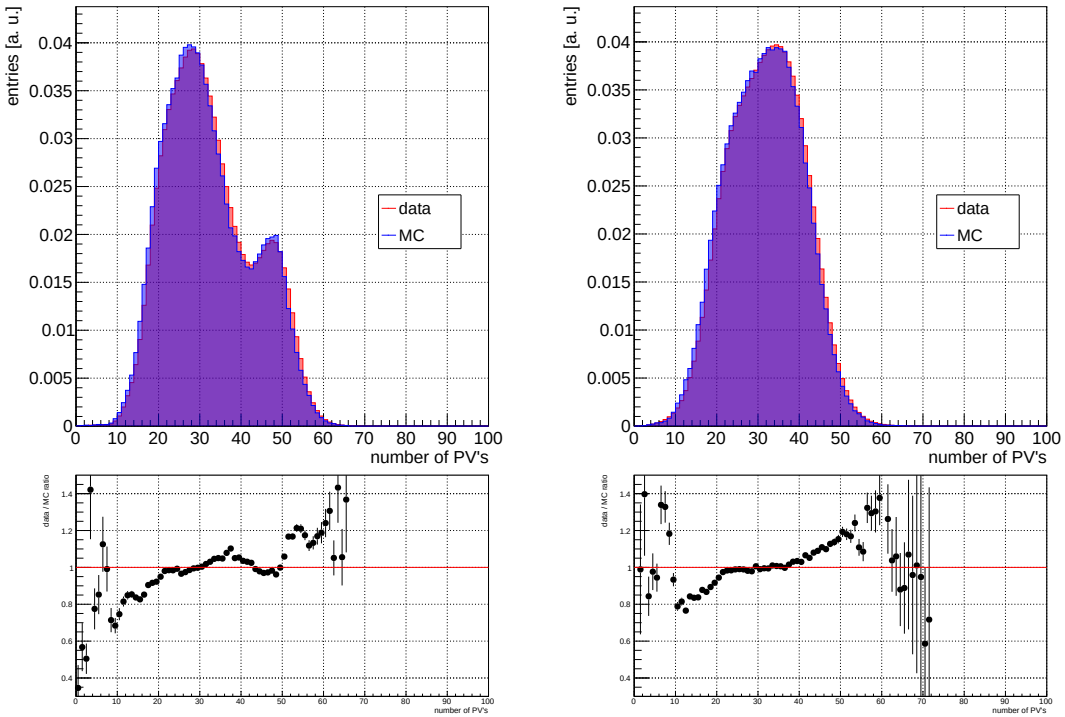

Figure 3.9: Distribution of the number of primary vertices in data (red) and MC samples (blue) for the 2017 (left) and 2018 (right) datasets, and their ratio (black dots in the lower pads).

Muon identification efficiency

The single muon efficiency has been studied on data and simulated samples through the tag-and-probe method, described below, following the strategy adopted in the 2016 analysis of first measuring the muon offline reconstruction efficiencies, and then the trigger efficiencies with respect to offline muons.
The offline single muon efficiency is therefore calculated as the product of the following terms:

1. ε_{Track}: offline muon tracking efficiency in the silicon tracker
2. $\varepsilon_{ID}|\varepsilon_{Track}$: offline reconstruction efficiency in the muon chambers and additional muon quality cuts, with respect to a silicon track
3. $\varepsilon_{trigger}$: online reconstruction efficiency with respect to the offline muon object

The TnP method consists of the reconstruction of the J/ψ resonance as a pair of muons, one of which has passed a tight identification ("tag") and the other a loose identification ("probe"). The probes are divided into two categories, "passing" and "failing", depending on a specific selection criteria. The efficiency of the single muon reconstruction is computed as the ratio of the number of the passing probes over the total number of probes in the sample, as obtained through a simultaneous fit to the di-muon invariant mass distributions of the events belonging to the different categories.

The muon-tracking efficiency has been extensively studied by the CMS Tracker Particle Object Group and is described in [74]. No action is require to correct the tracking efficiency, as the scale factors are very close to unity.
The tracking efficiencies and scale factors are shown in Fig. 3.10 as a function of the offline matched muon transverse momentum and pseudorapidity.

The offline muon reconstruction efficiency and scale factors for the medium muon ID (the one used to select muons in the analysis) have been computed by the CMS Muon Particle Object Group and the results have been used in the analysis.
The scale factors are defined as the ratio of efficiency computed on data over the efficiency computed on Monte Carlo samples. The efficiencies are computed using the tag-and-probe strategy described above. In particular, tag and probe muons are defined as follows:

tag: offline muon passing the TightID, with $p_T > 20$ GeV, matched to the HLT_Mu20 trigger leg [7].

[7] An HLT path selecting muons with a transverse momentum greater than 20 GeV

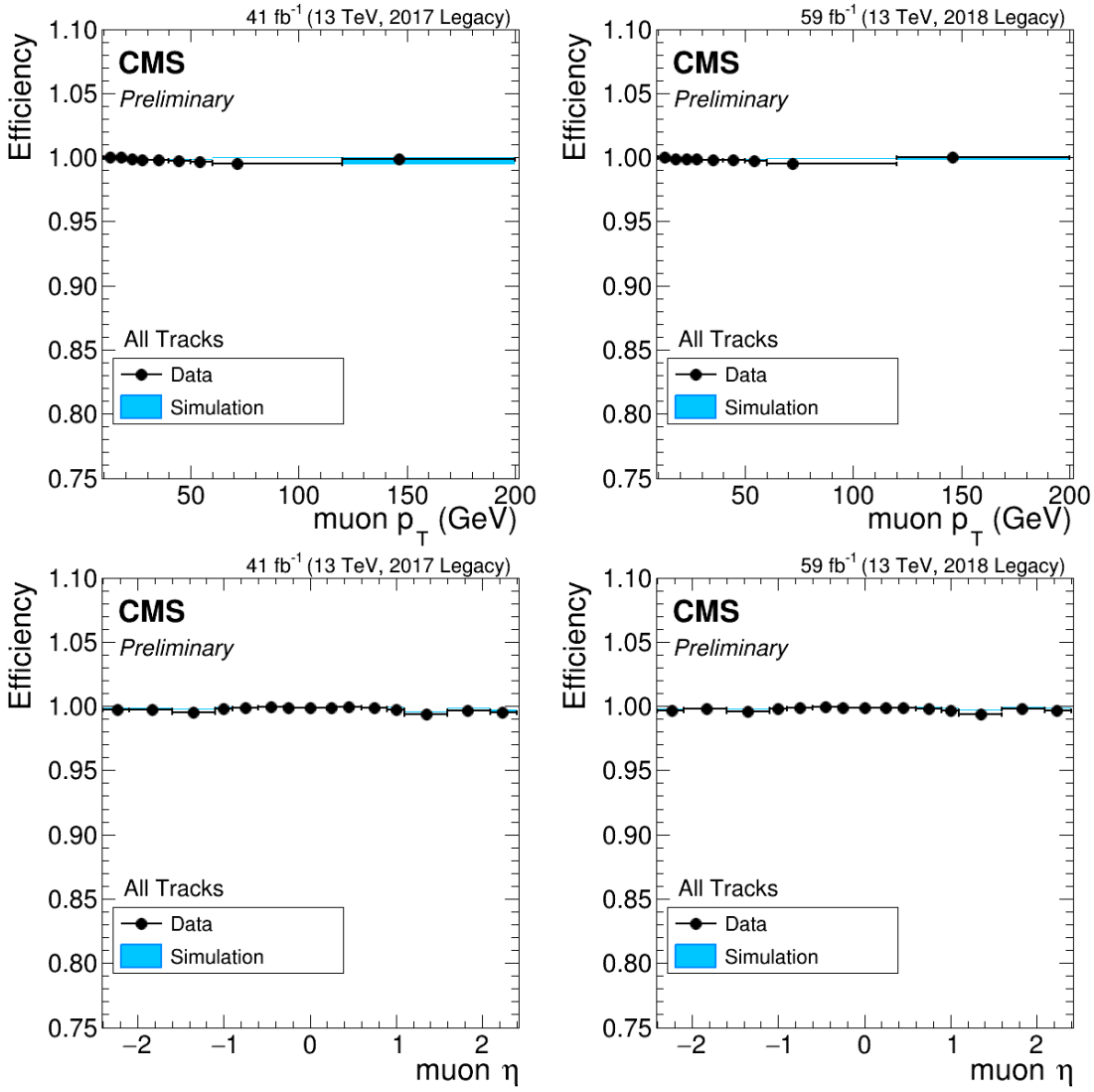

Figure 3.10: Scale factors (data-over-MC) for the track reconstruction evaluated on 2017 (left) and 2018 (right) samples as function of the transverse momentum of the probe track (upper plots) and of the pseudorapidity of the probe track (lower plots).

probe: offline tracks with $p_T > 2$ GeV; furthermore, the tag and probe muons are required to have $\Delta R_{M1}(\mu_{tag}, \mu_{probe}) > 0.3$ (the radial distance evaluated at the first muon chamber) and $\Delta Z(\mu_{tag}, \mu_{probe}) < 0.5$.

passing probe: probes passing the medium muon ID.

Since the signal muons of the analysis are very close to each other (see Fig. 3.11), it has been verified that the medium muon ID efficiency does not depend on the distance between the tag and the probe (where the distance between the tag and probe tracks is defined as $dR = \sqrt{\Delta\phi^2 + \Delta\eta^2}$). Figure 3.12 shows the efficiency of the medium muon ID as a function of the tag and probe distance (measured at vertex). The variation of the efficiency as a function of dR is small and can be ignored.
It has also been verified that the scale factor for the medium muon ID does not depend on the distance between the tag and the probe measured at the first muon station. Results are shown in Fig. 3.13; also in this case, the variation of the efficiency is small and has been ignored.

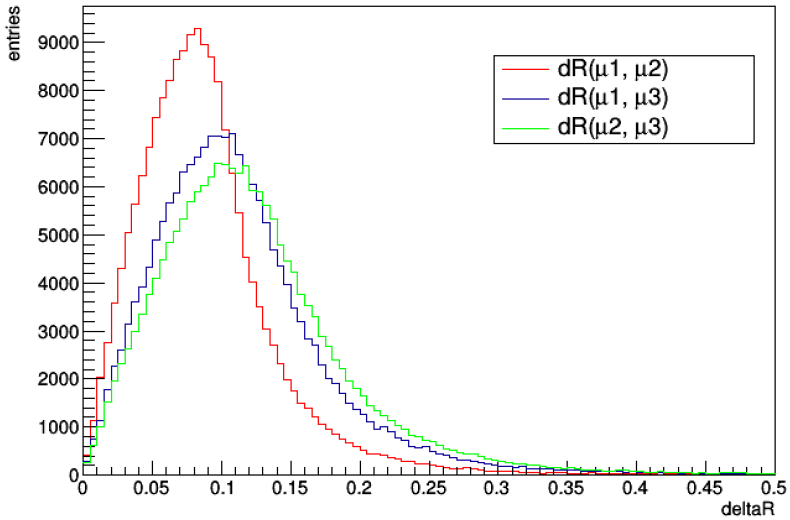

Figure 3.11: Distribution of the radial distance (evaluated at vertex) between the three signal muon couples evaluated on the 2018 simulated signal sample. The distance between two muons is defined as $\sqrt{\Delta\phi^2 + \Delta\eta^2}$. Signal muons are considered collimated, as the distance between them hardly exceed 0.3 and it peaks below 0.1.

Figure 3.15 shows values and errors of the scale factors of the medium muon ID flag as evaluated on the 2017 and 2018 samples as a function of the probe pseudorapidity and transverse momentum. Where the scale factor could not be evaluated due to the lack of statistics, the value 1 ± 0 is used. This does not pose a problem for the result of the

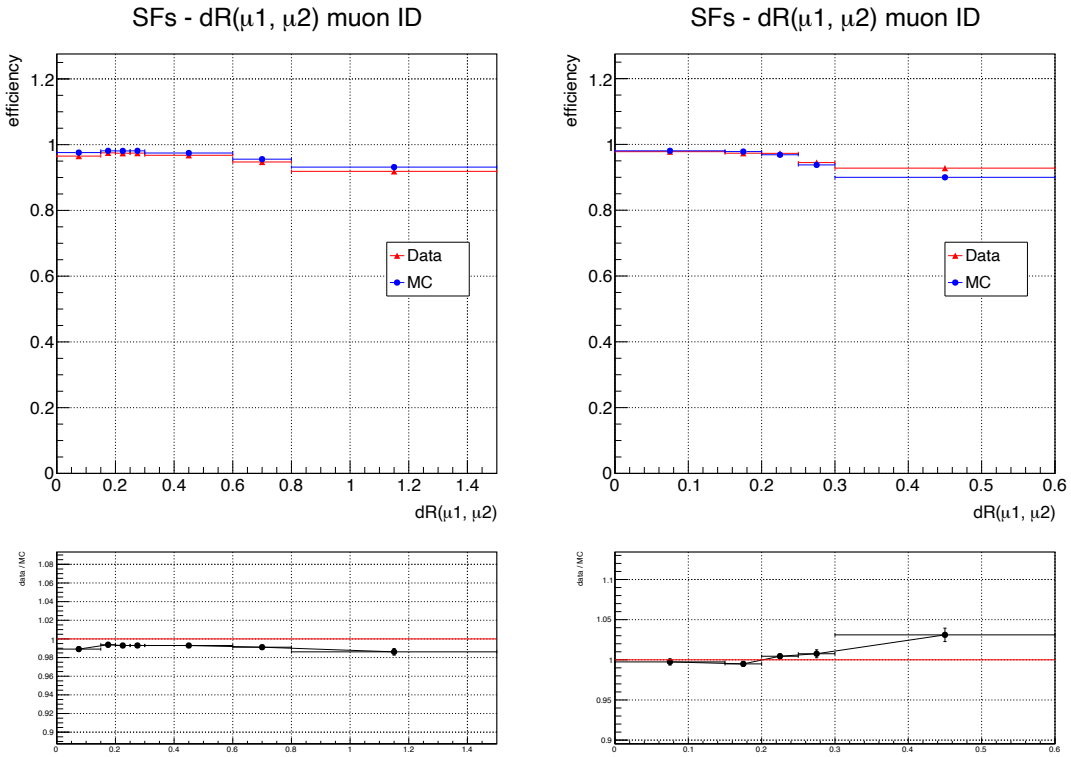

Figure 3.12: Efficiency and scale factors for the medium muon ID evaluated on 2017 (left) and 2018 (right) samples using the TnP method as function of the radial distance between the tag and the probe muon (evaluated at the vertex). Each figure shows the efficiencies of the medium muon ID for data (red) and MC (blue) samples in the upper pad, and the ratio of the data and MC efficiencies (the scale factor) in the lower pad. The scale factors do not show a relevant dependence on the radial distance between the tag and the probe muons in the region of the analysis (dR < 0.3).

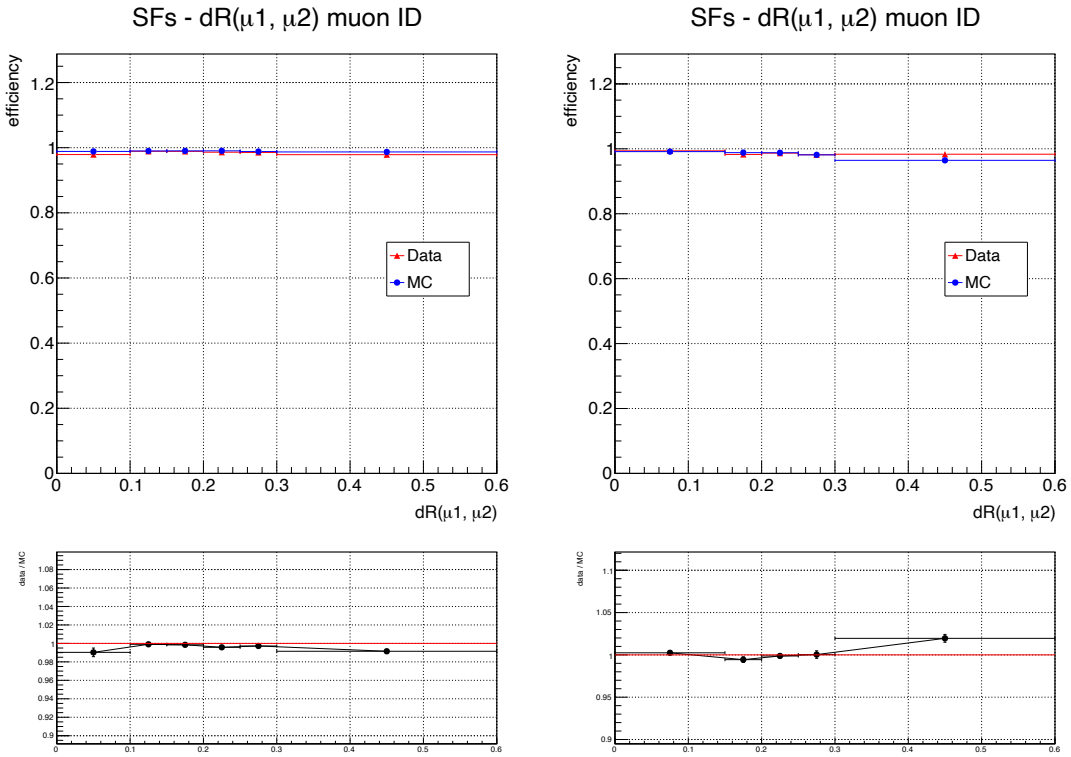

Figure 3.13: Efficiency and scale factors for the medium muon ID evaluated on 2017 (left) and 2018 (right) samples using the TnP method as function of the radial distance between the tag and the probe muon (evaluated at the first muon station). Each figure shows the efficiencies of the medium muon ID for data (red) and MC (blue) samples in the upper pad, and the ratio of the data and MC efficiencies (the scale factor) in the lower pad. The scale factors do not show a relevant dependence on the radial distance between the tag and the probe muons in the region of the analysis (dR < 0.3).

analysis, as these regions correspond to low-count regions in the signal sample as well (see Fig. 3.14), and scale factors are very close to unity.

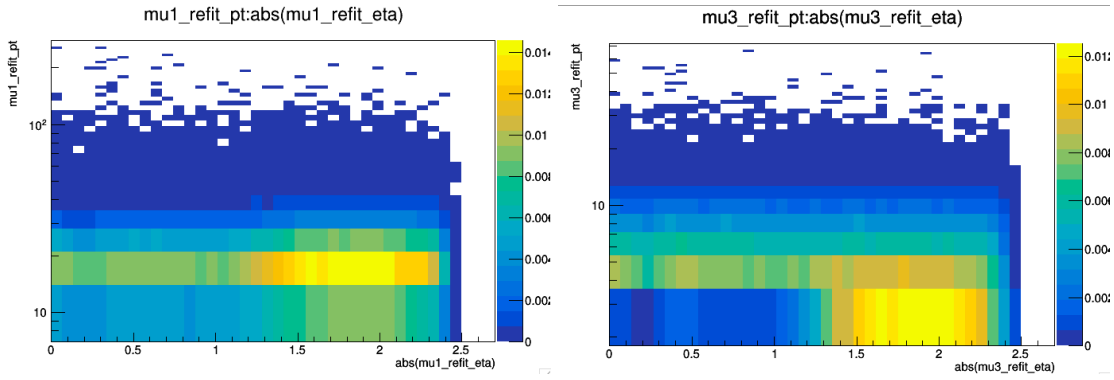

Figure 3.14: Distribution of signal muons in the p_T -η plane for the leading-p_T (left) and trailing-p_T (right) muons of the signal sample (here showing 2018 as an example). As expected, the low-η low-p_T region is not populated by signal candidates.

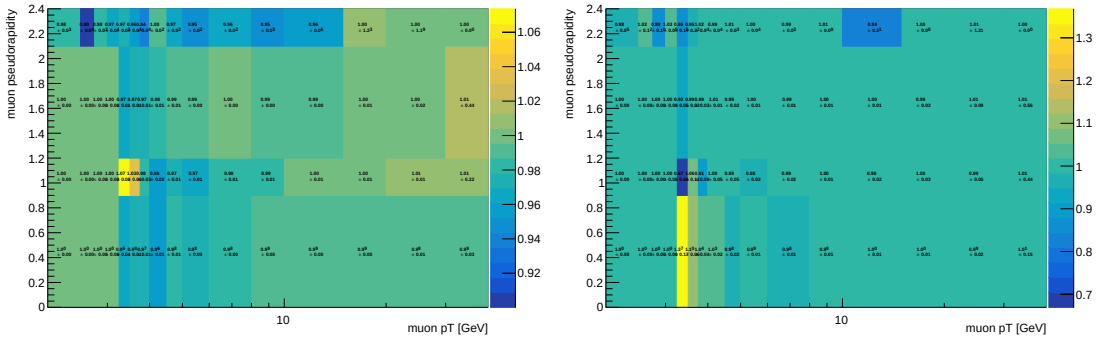

Figure 3.15: Scale factors (data-over-MC) of the medium muon ID measured on 2017 (left) and 2018 (right) samples with the TnP method, as function of the transverse momentum and pseudorapidity of the probe muon

The online muon identification efficiency has been studied using the TnP approach on $J/\psi \to \mu^+\mu^-$ events. The tag and the probe muons are defined as:

tag: offline muon passing the tight ID, with $p_T > 20$ GeV, matched to the HLT_Mu20 trigger leg [8].

[8] An HLT path selecting muons with a transverse momentum greater than 20 GeV

probe: offline muon passing the medium ID, with $p_T > 2$ GeV; furthermore, the tag and probe muons are required to have $\Delta R_{M1}(\mu_{tag}, \mu_{probe}) > 0.3$ (the radial distance evaluated at the first muon chamber) and $\Delta Z(\mu_{tag}, \mu_{probe}) < 0.5$.

passing probe: probes matched to an HLT muon.

Figure 3.16 shows the results obtained for the 2017 and 2018 samples as a function of the probe p_T in different bins of the probe pseudorapidity.

Trigger isolation efficiency

As an isolation cut is required at the HLT selection step, the correction of the simulated samples is completed computing the HLT isolation efficiency and scale factors. To do so, a version of the trigger without the isolation requirement on the three-muon final state is employed (HLT_Tau3Mu_Mu7_Mu1_TkMu1_Tau15_Charge1). This trigger has been online during 2017 and 2018 data taking together with the main trigger. During 2017, the trigger was prescaled by a factor varying from 2 to 20, and an integrated luminosity of 1.77 $fb^{-1}$was collected, while during 2018 the trigger was prescaled by a factor 10 and an integrated luminosity of 5.87 $fb^{-1}$was collected.

The scale factors are defined as the ratio of the efficiency computed on data and on the simulated Ds$\to \phi(\mu\mu)\pi$ samples, which in this case can serve as a proxy for the $\tau \to 3\mu$ decay. The denominator of the efficiency is the number of Ds$\to \phi(\mu\mu)\pi$ events matched to the non-isolated trigger version, while the numerator is defined as the number of Ds$\to \phi(\mu\mu)\pi$ events matched to the isolated trigger version. The efficiency is computed with a simultaneous fit to the invariant mass distributions of the events passing and failing this selection.
Data are selected by double-muon triggers, while the simulated sample is chosen to match the same generation conditions of the $\tau \to \mu\mu\mu$ MC samples used in the analysis (see Sec. 3.1.1).
Due to the non-isolated trigger prescale, only a small fraction of events can be used to compute the efficiency. For this reason, only a single value can be obtained for each year, and the scale factor cannot be differentiated in bins of the D_s pseudorapidity or transverse momentum, as done for the muon scale factors.
The signal (the Ds meson peak) is modelled with a gaussian function in data and with the sum of two gaussian functions in the MC. The smooth part of the background is modelled with an exponential function; the D^+ peak, observed in data, is modelled with a gaussian function and is included in the background, so that it is not considered for the efficiency calculation.
The results are shown in Fig. 3.17 and summarized in Tab. 3.3.

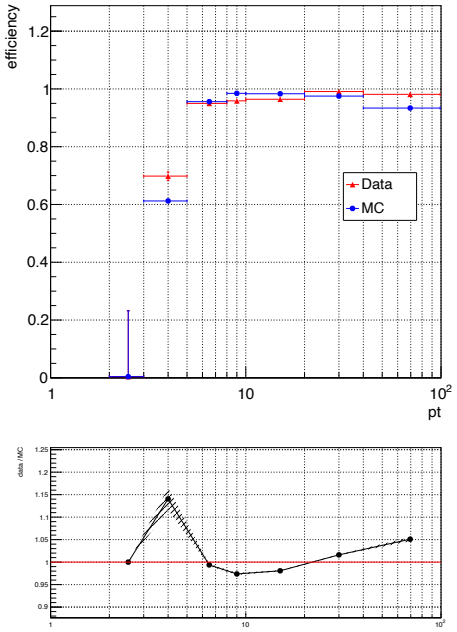

(a) $0 \leq \eta < 0.9$ - 2017

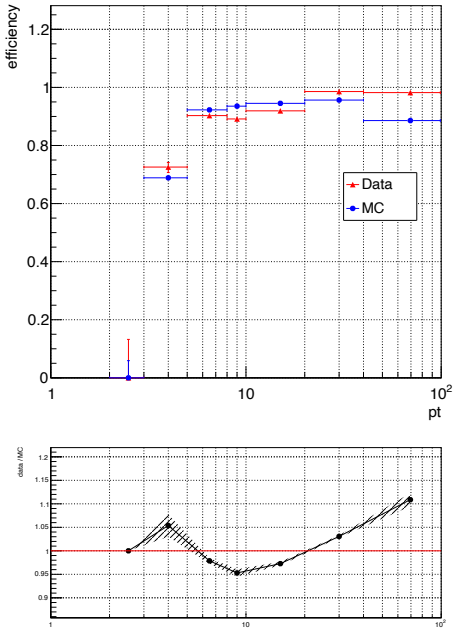

(b) $0.9 \leq \eta < 1.2$ - 2017

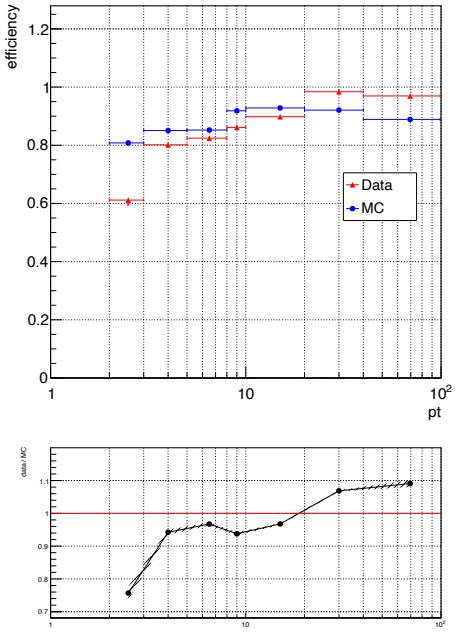

(c) $1.2 \leq \eta < 2.1$ - 2017

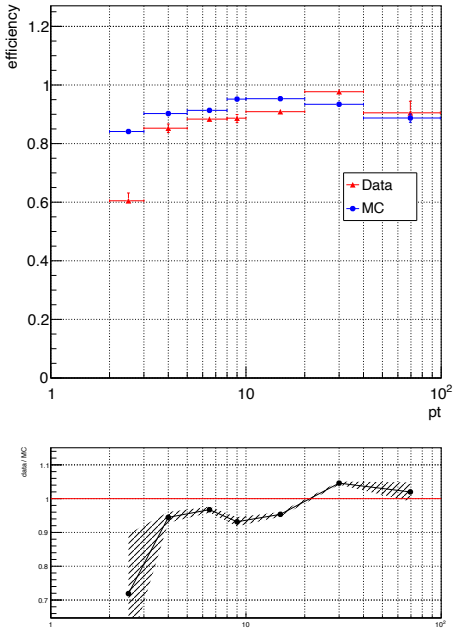

(d) $2.1 \leq \eta < 2.4$ - 2018

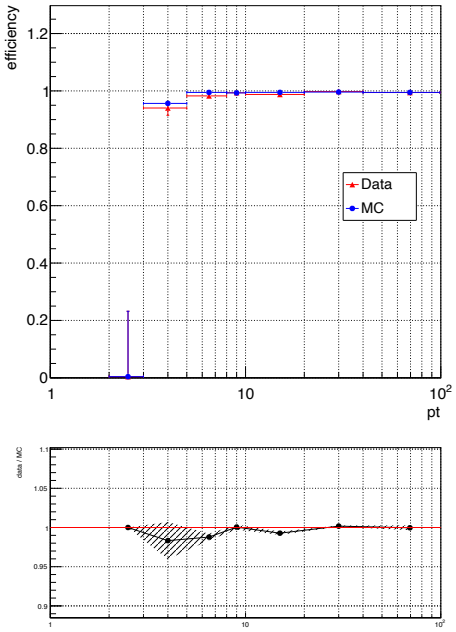

(e) $0 \leq \eta < 0.9$ - 2017

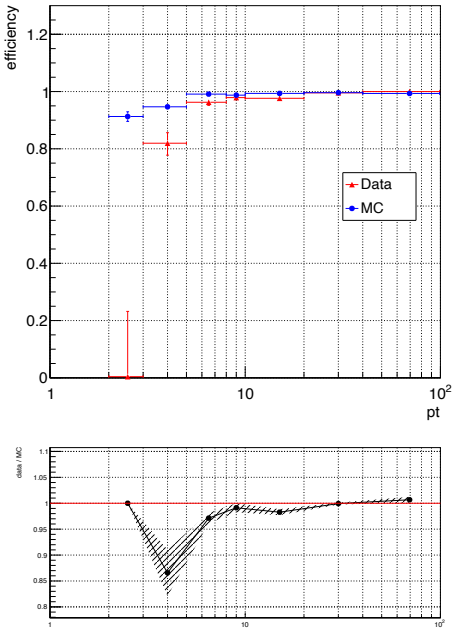

(f) $0.9 \leq \eta < 1.2$ - 2017

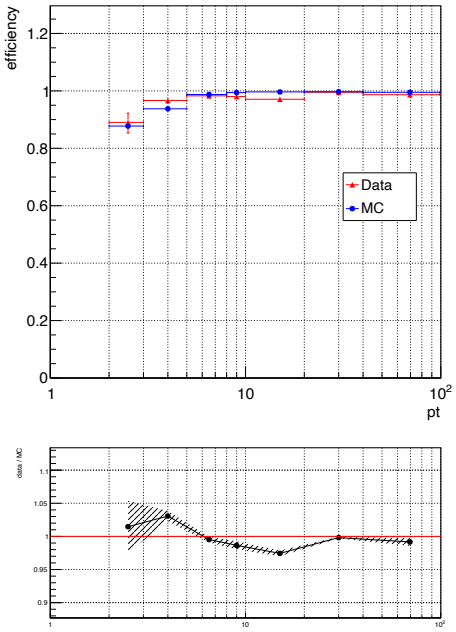

(g) $1.2 \leq \eta < 2.1$ - 2017

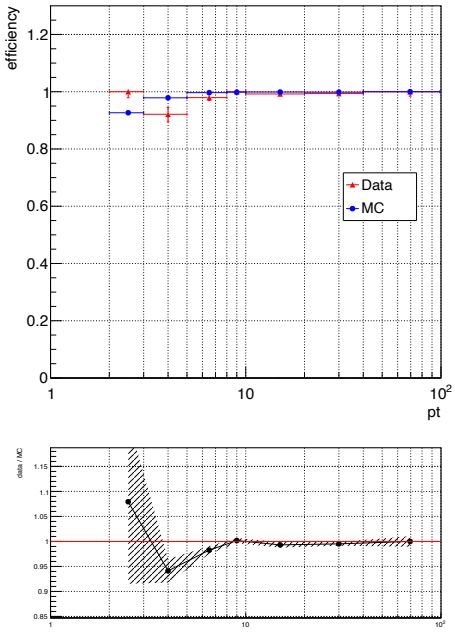

(h) $2.1 \leq \eta < 2.4$ - 2018

Figure 3.16: Reconstruction efficiency of HLT muons measured with the TnP method, as a function of the probe muon p_T , in different ranges of the probe muon pseudorapidity, for 2017 and 2018.

Table 3.3: HLT isolation efficiencies and scale factors computed on the 2017 and 2018 samples.

year	efficiency on data	efficiency on MC	scale factor
2017	0.458 ± 0.056	0.488 ± 0.010	0.939 ± 0.117
2018	0.613 ± 0.024	0.490 ± 0.029	1.250 ± 0.089

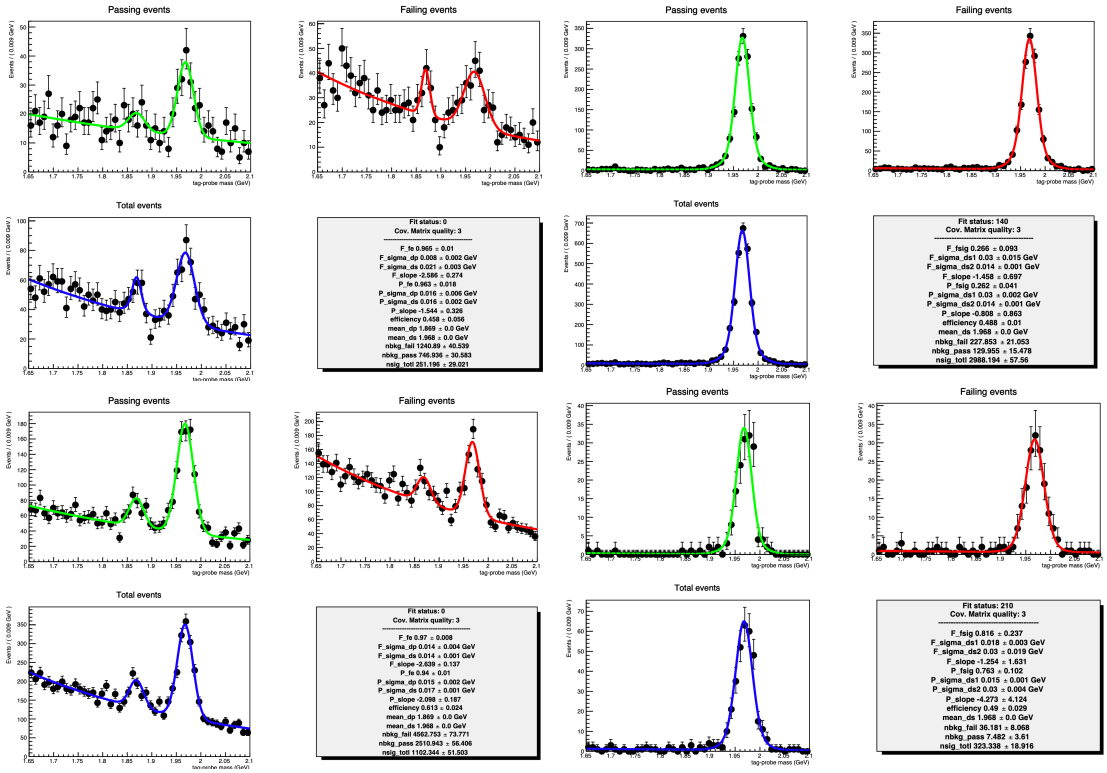

Figure 3.17: Fit to the Ds→ $\phi(\mu\mu)\pi$ invariant mass distribution on data (left) and MC (right) for 2017 (upper plots) and 2018 (lower plots) samples. Each plot is showing the fit to the passing (green line) and failing (red line) sets of events. The total set of events is also shown and the fitted model is plotted over it (blue line)

Next-to-leading order reweighing

The signal sample of the analysis is simulated with leading order (LO) precision, as the next-to-leading order (NLO) computation would take too long. However, the efficiencies of the selection steps (mainly the BDT selection) are expected to depend on the kinematic properties of the generated particles, especially those of the W boson. For this reason, a smaller sample (50000 events) of pp→W events has been produced with NLO precision using the MadGraph5 software. The process has been generated using the SM pp→W diagrams, and the hadronization step is achieved using Pythia8, with the same configurations of Sec. 3.1.1. This sample has been used to re-weight the distribution of the generated W bosons in the p_T -η plane. The distribution of events in the LO and NLO samples, and their ratio, are shown in Fig. 3.18. The weight distribution, evaluated on the analysis signal samples, is shown in Fig. 3.19. The average weight (1.03) is very close to unity, despite its large spread.
The map of weights of Fig. 3.18 is applied event-per-event to the simulated signal samples used in the analysis. In the regions where the scale factor is not defined (due to the low statistics either in the LO or in the NLO sample), the value 1±0 is used.

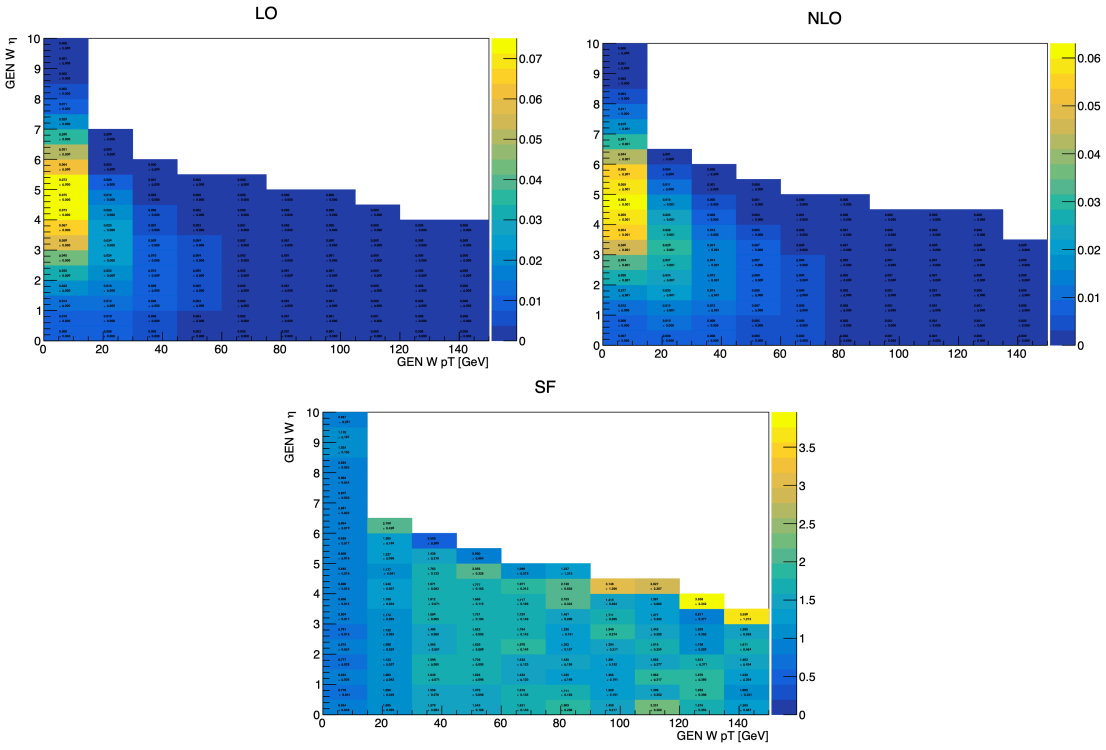

Figure 3.18: Distribution of the generated W bosons in the LO (upper left) and NLO (upper right) samples. Their ratio (lower plot) is used as a per-event scale factor. Empty bins correspond to kinematic regions not populated by the W→ τν, τ → 3μ decay.

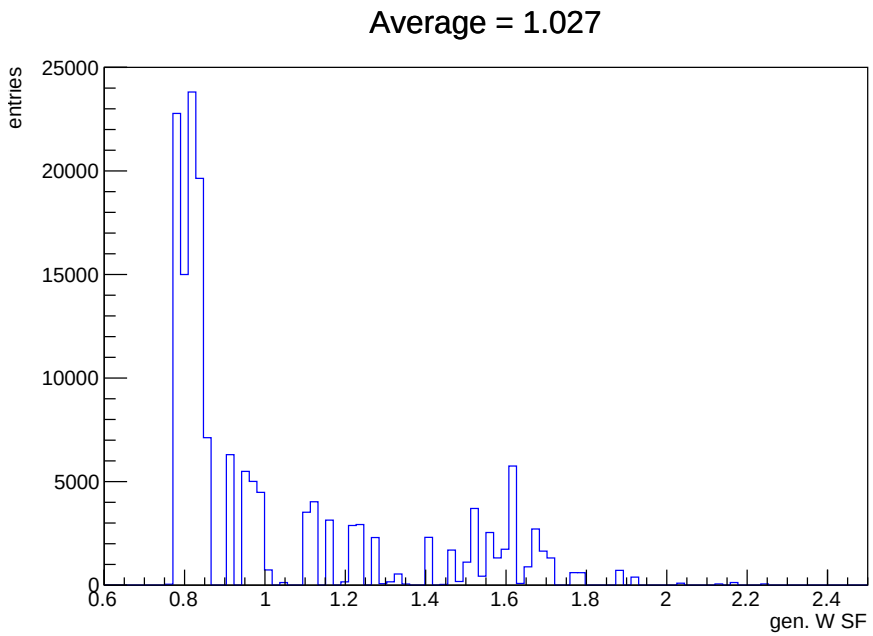

Figure 3.19: Distribution of the NLO weights evaluated on the analysis signal sample. The average weight is close to unity.

3.1.4 Multivariate selection

Data and MC events which pass the pre-selection step described in Sec. 3.1.2 are further processed by a multivariate discriminator in order to reduce the background contamination in the final set of signal candidates. The discriminator adopted for this task is a Boosted Decision Tree (BDT); for the analysis, the XGBoost [75] boosting algorithm has been chosen.

BDT setup

The performance of the BDT is influenced by different hyper-parameters; their value has been chosen to minimize the impact of overtraining while keeping a good signal-background discriminating power. The values and meaning of the parameters are listed in Tab. 3.4.

Table 3.4: Hyper-parameters of the BDT used to reject background events in the W channel.

parameter	value	description
Max depth	5	maximum depth of each tree
Learning rate	0.01	weight reduction assigned to each tree
Number of tree	10000	number of trained trees
Sub-sampling	0.7	fraction of the training sample randomly selected to train each tree
Column sampling	0.7	fraction of the input features randomly selected to train each tree
Minimum weight	50	Minimum weight of each leaf to continue the splitting
Early stopping	100	maximum number of rounds without improvement before early stopping

The BDT is trained using the simulated signal samples described in Sec. 3.1.1 (about 0.4 million events), re-weighted as described in Sec. 3.1.3, and real data lying outside the signal region (about 0.3 million events). Smaller samples of simulated signal with a shifted value of the τ lepton mass have been added to the training to populate the analysis invariant mass range. The values considered are 1.65, 1.70, 1.85, 1.90 and 1.95 GeV. Each sample counts 50000 generated events, of which about 10000 events pass the pre-selection step.
The events used in the training are selected as described in Sec. 3.1.2. The events are also divided into two sub-samples, one used during the BDT training (the train sample, 60% of the events), the other used to evaluate the BDT performance (the test sample, 40% of the events).

BDT features

The BDT input features used in the training are shown in table 3.5. These variables describe the W boson, τ lepton and muons topological and kinematic properties. The

distributions of the BDT features obtained from the background and signal samples are reported in App. C.

Table 3.5: Input features used to train the BDT

Variable name	description
τ p_T	transverse momentum of the τ candidates
W p_T	transverse momentum of the W boson, obtained summing the transverse momentum of the τ candidate and the MET
mT(τ, ν)	transverse mass of the τ plus the MET vector, defined as $\sqrt{2p_T^{\tau}p_T^{\nu}\cos\theta}$, where θ is the angle between pT_{τ} and the MET in the transverse plane
τ rel. isolation	relative isolation of the τ candidate
$\Delta\phi(\tau, \text{MET})$	azimuthal angular distance between the τ candidate and the transverse missing energy
pT_{τ} / MET	ratio of τ candidate transverse momentum and the MET
max($\not{p}_z$)	maximum of the two solutions obtained from from eq. 3.3
min($\not{p}_z$)	minimum of the two solutions obtained from from eq. 3.3
$\Delta p_z(\mu_1,\mu_2)$	difference of the longitudinal momenta of μ_1 and μ_2
$\Delta p_z(\mu_1,\mu_3)$	difference of the longitudinal momenta of μ_1 and μ_2
$\Delta p_z(\mu_2,\mu_3)$	difference of the longitudinal momenta of μ_2 and μ_3
SV L/σ	significance of the distance in the transverse plane between the beamspot and the three-muon vertex
SV prob	χ^2 of the three-muon vertex
SV cos(θ^{IP})	cosine of the pointing angle between the τ candidate momentum and the vector from the beamspot and the three-muon vertex in the transverse plane

Bias tests

Possible correlation between the τ mass and the BDT response could create false enhancements in the mass distribution. As shown by the correlation matrix in Fig. 3.21, linear correlation is not present. To exclude possible correlations other than linear, we evaluated the efficiency of the BDT discriminator (defined as the number of events passing the BDT working point divided by the number of events passing the pre-selections) as a function of the reconstructed τ mass. First, the check is performed on data events coming from the sidebands (Fig. 3.22). Then, the same test is performed on MC samples with different values of the τ lepton mass (Fig. 3.20). As shown in these figures, the efficiency on data follows a smooth patter, while it is clearly shaped when evaluated on the MC sample. In this case, however, the efficiency values are compatible among samples with different values of the τ lepton mass. The difference between events coming from the tails of the $\tau \to 3\mu$ distribution and the events coming from the central part is also visible in the distribution of some input features of the BDT (the signal candidate isolation, the estimation of the longitudinal component of the neutrino momentum, the pseudorapidity of the signal candidate, the muon ID tight flag, the different between the longitudinal momenta of the signal muons, the secondary vertex pointing angle), as shown in Fig. 3.25. The difference between the two types of events has been ascribed to the difference of the pseudorapidity distributions. As shown in Fig. 3.23, the BDT efficiency is constant in a small-enough pseudorapidity range, and get lower as pseudorapidity increases. The shape observed on the MC sample is thus imputed to the diversity present in the reconstruction of some of the observables in different regions of

the detector.

As an additional sanity check, the distribution of the BDT score for data signal candidates with electric charge equal to +1 and -1 is compared. Figure 3.24 shows that the two distributions are compatible, as expected since the BDT does not include features related to the signal candidate electric charge.

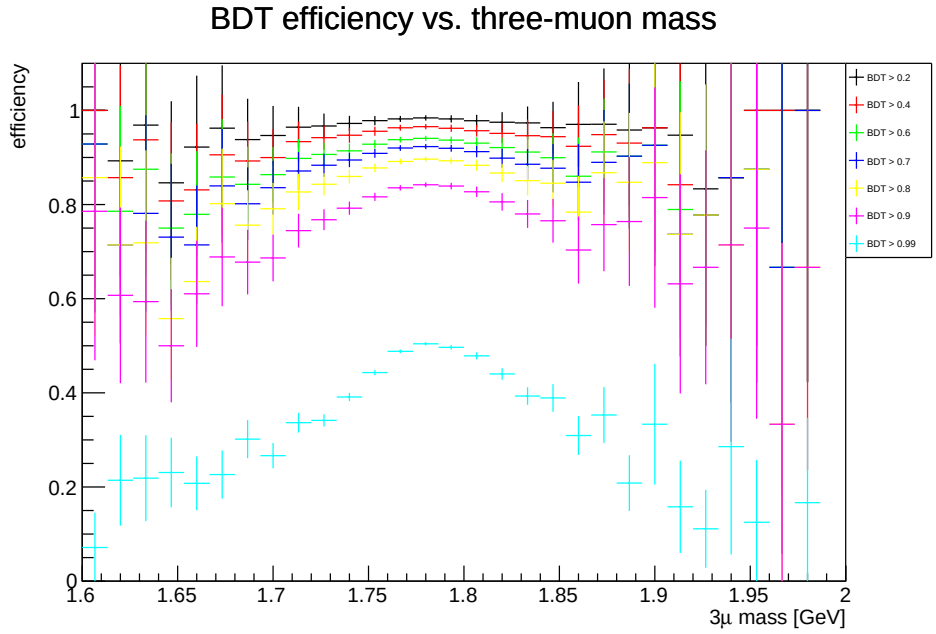

Figure 3.20: BDT selection efficiency, for different BDT score thresholds, as a function of the signal candidate invariant mass, evaluated on simulated signal events. Each curve corresponds to a different BDT score threshold used to reject background events (the higher the value, the tighter the selection). The cut 0.99 (light blue curve) is the closest to the analysis working point.

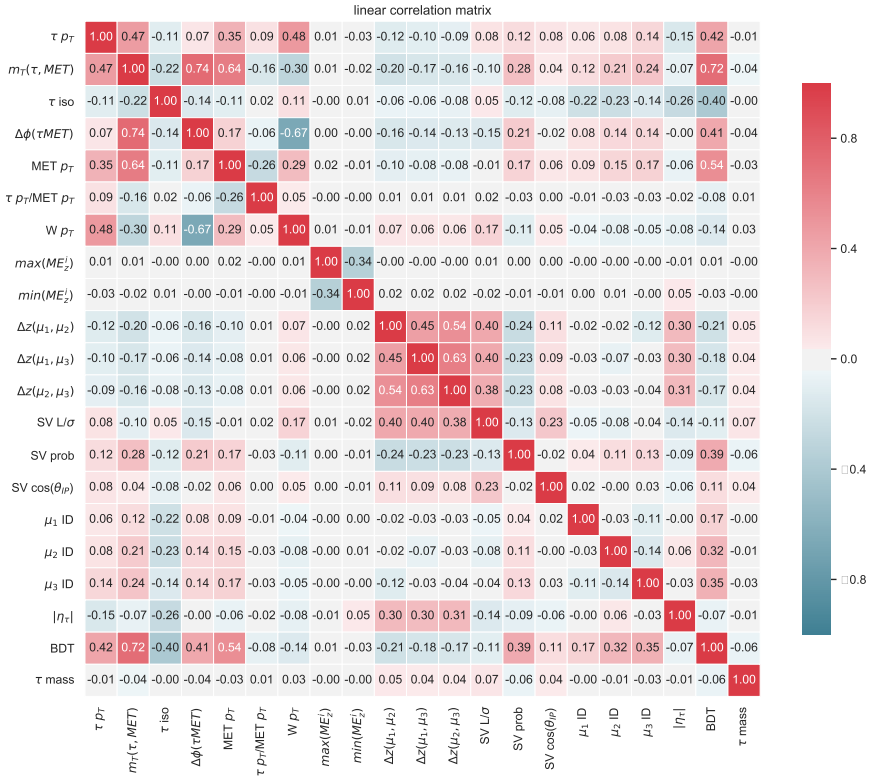

Figure 3.21: Correlation matrix showing the linear correlation among the training features, as evaluated on the data sample.

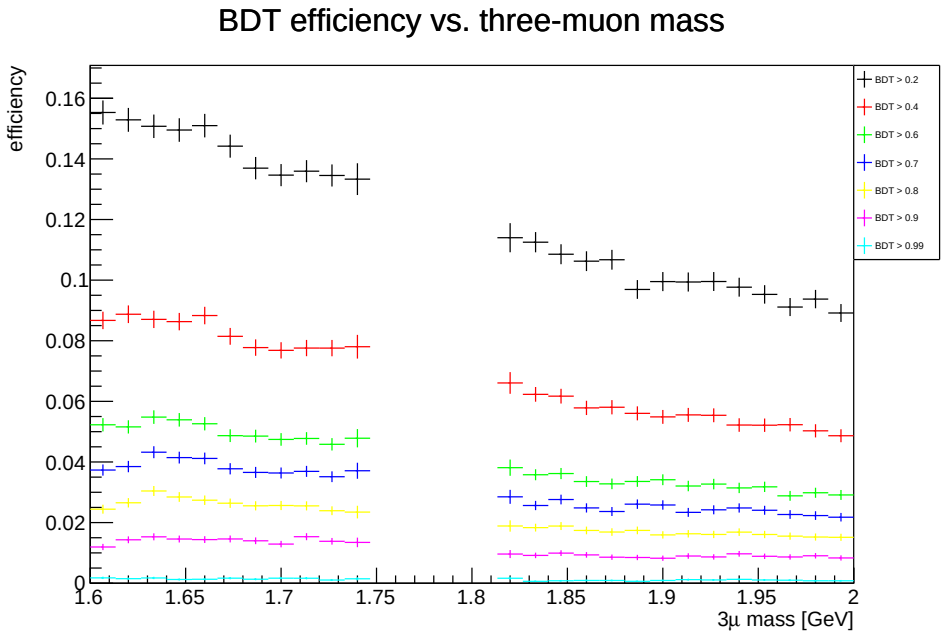

Figure 3.22: BDT selection efficiency, for different BDT thresholds, as a function of the signal candidate invariant mass, evaluated on data.

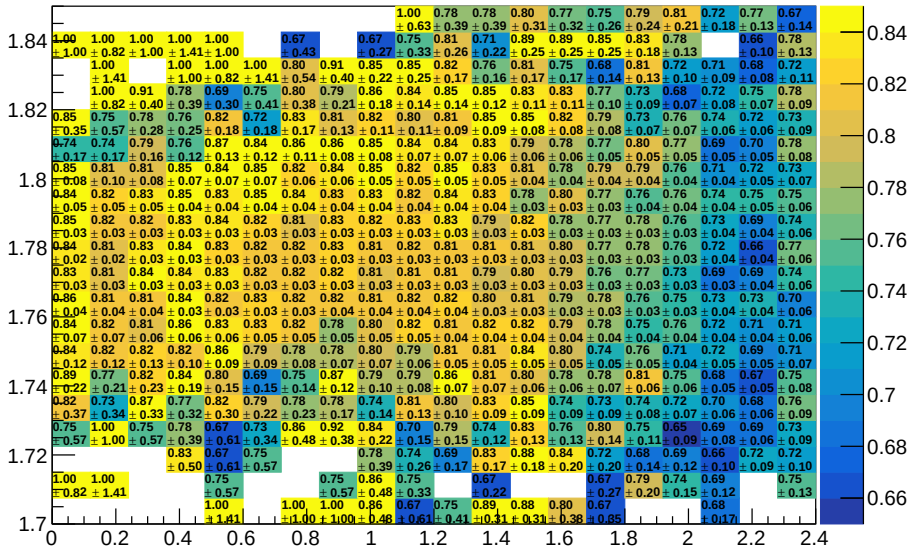

Figure 3.23: BDT efficiency (color bar) as a function of the signal candidate invariant mass (vertical axis) and of the signal candidate pseudorapidity (horizontal axis), evaluated on the simulated signal sample. The efficiency is constant in a small-enough pseudorapidity range, but gets lower as the signal candidate invariant mass moves away from the simulated tau mass value (1.777 GeV). The efficiency is evaluated for a cut on the BDT score equal to 0.99.

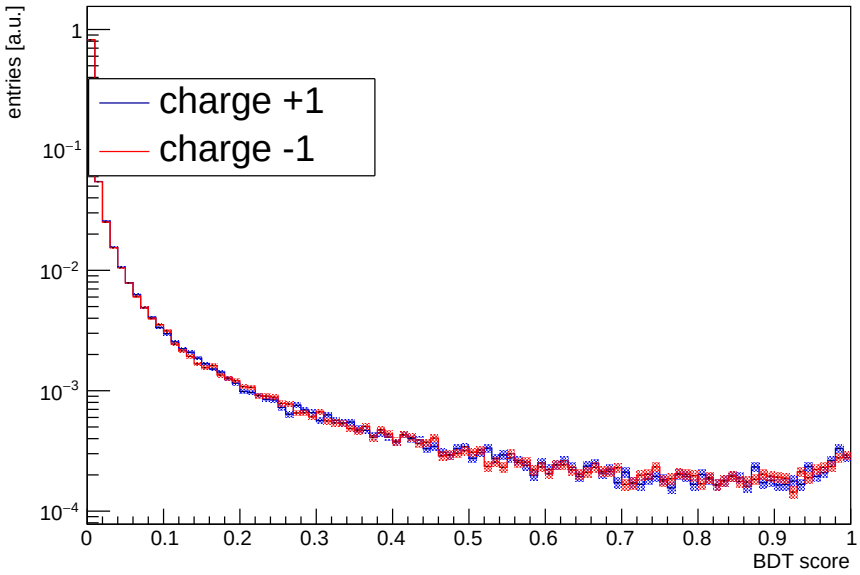

Figure 3.24: Distribution of the BDT score of signal candidates from the data sample. In blue, data candidate have charge +1. In red, data candidates have charge -1.

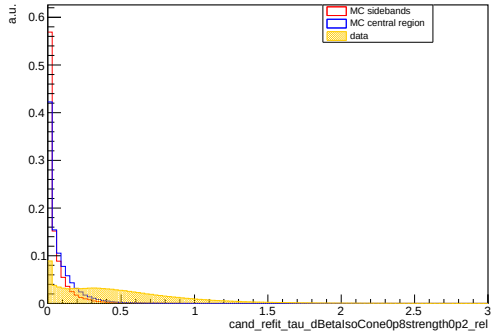

(a) τ candidate isolation

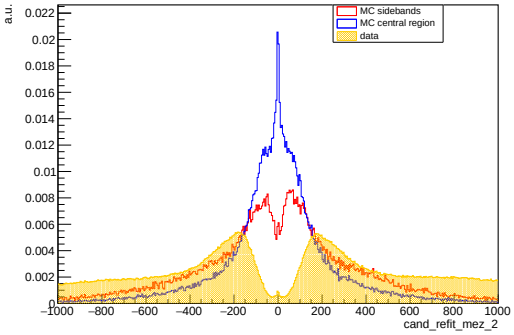

(b) Second solution of Eq.3.3

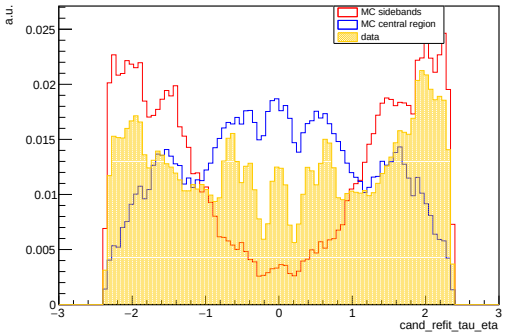

(c) τ pseudorapidity

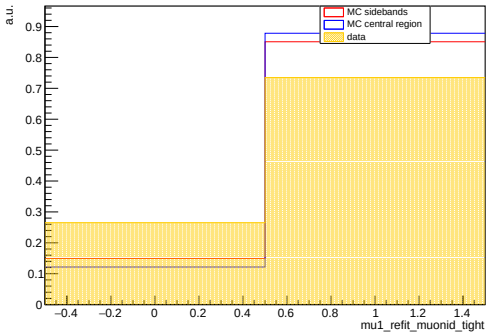

(d) Tight muon-ID flag evaluated on the leading muon

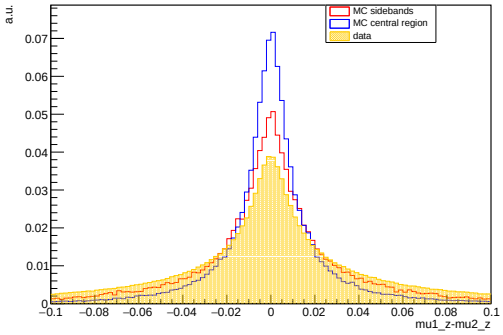

(e) Difference of the longitudinal components of the momenta of μ 1 and μ 2

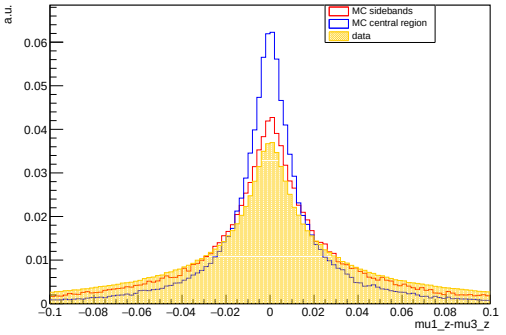

(f) Difference of the longitudinal components of the momenta of μ 1 and μ 3

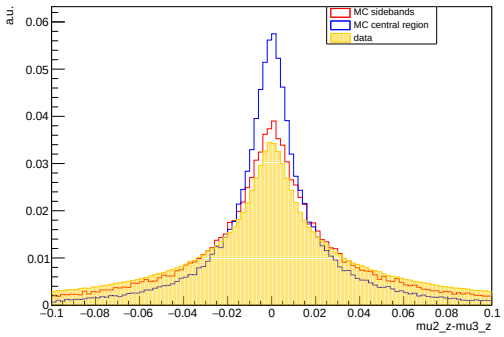

(g) Difference of the longitudinal components of the momenta of μ 2 and μ 3

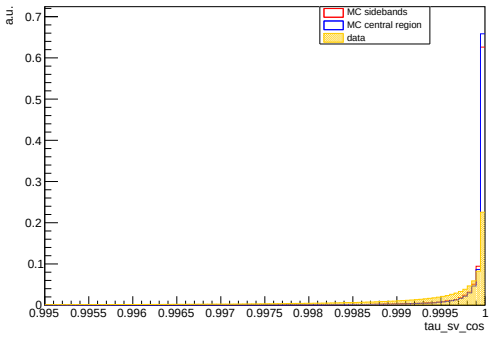

(h) Poiting angle between the primary and secondary vertex

Figure 3.25: Distribution of some of the BDT features obtained on signal and background events. Signal events are considered in two different groups: events with an invariant mass value lying far from the nominal tau mass value (1.777 GeV), i.e. outside the range (1.75 GeV, 1.81 GeV) (red line), and events with an invariant mass value lying close to the nominal tau mass value, i.e. inside the range (1.75 GeV, 1.81 GeV) (blue line). The distributions for data events are also plotted for comparison (shaded orange distribution).

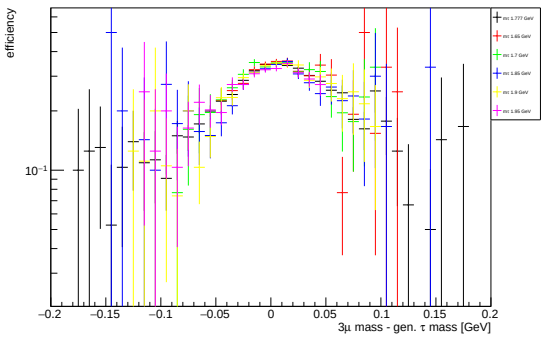

(a)

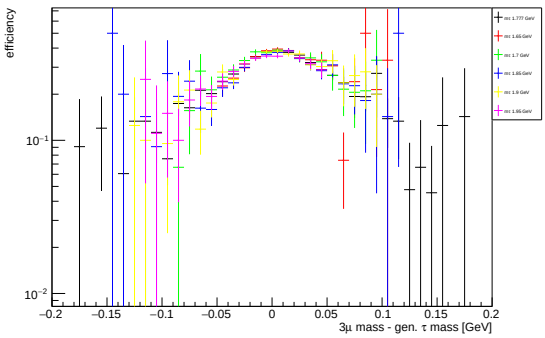

(b)

Figure 3.26: BDT efficiency (requiring a score greater than 0.9) evaluated on simulated signal samples with different values of the generated τ mass, as a function of the signal candidate invariant mass. On the left, the BDT was trained with all the fictious mass samples (1.65 GeV, 1.70 GeV, 1.85 GeV, 1.90 GeV and 1.95 GeV), on the right, the BDT was trained with only the nominal τ mass sample (1.777 GeV). Each distribution is shifted on the horizontal axis by its generated τ mass value to help the comparison.

3.1.5 Peaking backgrounds

The presence of a structured background could weaken the modeling adopted in the limit extraction. Moreover, the presence of a peaking background in the signal region could create an accumulation of events which would falsify the value of the final result. For this reason, the presence of three-body-final-state contaminations has been studied. In particular, events coming from D^+(1.87 GeV) meson decays could fall into the signal region (1.74-1.82 GeV).

Tab. 3.6 shows the list of three-body-final-state $D^+$and Ds decay channels which could contribute to the background. The number of Ds$\to \phi(\mu\mu)\pi$ and $D^+ \to \phi(\mu\mu)\pi$ events has been estimated from the 2017 and 2018 full datasets with a fit to the three-muon mass distribution, as shown in Fig. 3.27. Events are selected as described in sec. 3.1.2. In addition, the presence of two opposite-sign muons close to the ϕ mass (1020 MeV, in a 100 MeV window) and of a secondary vertex with a distance significance in the transverse plane greater than 5 and a probability greater than 0.01 are required. To improve the resolution of the D meson peaks, the pion mass is assigned to the muon not compatible with the ϕ selection.
The numbers obtained from the fit are divided by this additional selection efficiency, which has been evaluated on a Ds$\to \phi(\mu\mu)\pi$ MC sample; its value is 0.52 ± 0.03 and it is used to compute the expected number of events for each channel of Tab. 3.6.
The numbers reported in Tab 3.6 already include the correct power of the kaon-muon and pion-muon misidentification rate (an overestimating value of 5×10^{-3} [76] is considered), depending on the number of fake muons (pions and kaons) in the event.

Tab.3.6 shows that the biggest contribution from three-body-final-state decays is given by Ds$\to \phi(\mu\mu)\pi$ events. Fig. 3.28 shows the distribution of events, obtained from the 2017 and 2018 samples, containing a $\phi \to \mu\mu$ resonance, after the BDT selection. Only one event in the Ds mass region (1.97 GeV) survives this selection; thus, no contamination is expected from D^+three-body-final-state decays, assuming that the BDT efficiency is the same for all the channels considered for this study (see Sec. 3.1.4) [9].
The information derived from Fig. 3.28 and Tab. 3.6 shows that no further action should be taken after the BDT selection to suppress the peaking background.

The presence of di-muon resonances has been investigated further. Fig. 3.29 shows the presence of $\phi \to \mu\mu$ events after the BDT selection. For this reason, events where two of

[9] Since muon IDs are included in the BDT features, we can also expect three-fake events to be selected less efficiently than single-fake events.

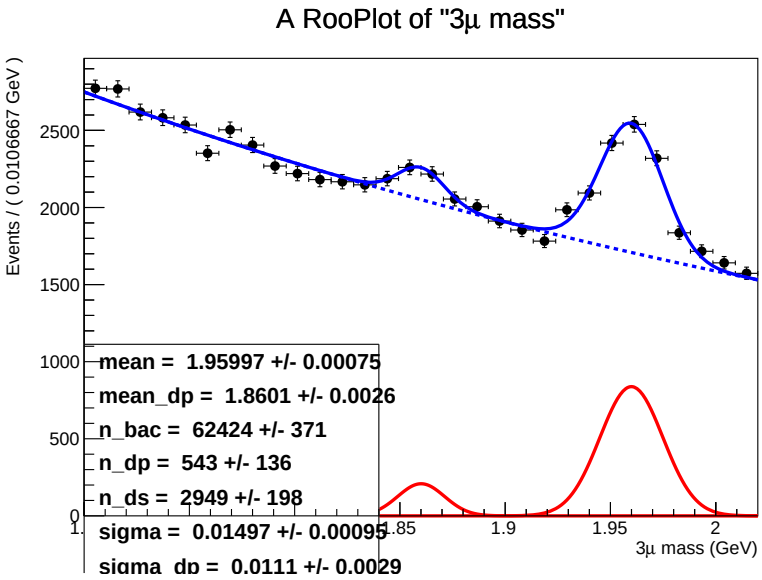

Figure 3.27: Fit to the three-muon invariant mass distribution after the pre-selection and an additional $\phi \to \mu\mu$ selection.

Table 3.6: Number of expected background events as evaluated in different three-body-final-state channels. The numbers reported in this table are computed before the BDT selection and after the pre-selection described in Sec. 3.1.2. The numbers shown in each column already inlcude the misidentification probability of kaons and pions, as described in sec. 3.1.5. The error on the estimation of these numbers is entirely due to the estimation of the number of Ds$\to \phi(\mu\mu)\pi$ and $D^+ \to \phi(\mu\mu)\pi$ events on data, and amounts to 7% for Ds channels and 25% for D^+ channels.

Channel	**w.r.t. Ds$\to \phi(\mu\mu)\pi$**	**expected n. of events**
Ds$\to \phi(\mu\mu)\pi$	1	5671 (obs. in data)
Ds$\to \eta(\mu\mu)\pi$	4×10^{-1}	2198
Ds$\to$KKπ	10^{-1}	549
Ds$\to \omega(\mu\mu)\pi$	4×10^{-2}	220
Ds$\to \pi\pi\pi$	2.4×10^{-2}	14
Channel	**w.r.t. $D^+ \to \phi(\mu\mu)\pi$**	**expected n. of events**
$D^+ \to \phi(\mu\mu)\pi$	1	984 (obs. in data)
$D^+ \to$KKπ	1.43	1407
$D^+ \to$KKπ	1.5×10^{-1}	148
$D^+ \to \pi\pi\pi$	5×10^{-2}	49
$D^+ \to \omega(\mu\mu)\pi$	1.5×10^{-2}	15
$D^+ \to \eta(\mu\mu)\pi$	1.3×10^{-3}	13

the signal muons are compatible with a $\phi \to \mu\mu$ decay are vetoed (within a window of 20 MeV around the ϕ mass). This brings to an improvement of about 8% in the expected upper limit.
From the same figure it can be inferred that there is no need to veto any other di-muon resonance, such as η or ω.

The contamination from partially-reconstructed events, such as the semileptonic decays of the D mesons (where neutrinos and neutral pions are are missed in the reconstruction of the final state) is expected to be one order of magnitude more abundant than Ds$\to$ $\phi(\mu\mu)\pi$ events. Anyway, the three-muon mass distribution of these events is not peaking, due to the missing momentum of the non reconstructed tracks. Since these events have an invariant mass strictly below the Ds or D^+masses, their presence could twist the background shape; as will be shown in Sec. 3.1.6, the distribution of background events is smooth over the full range of the analysis, although the small number of events surviving the BDT cut. No further study has been performed on these events.

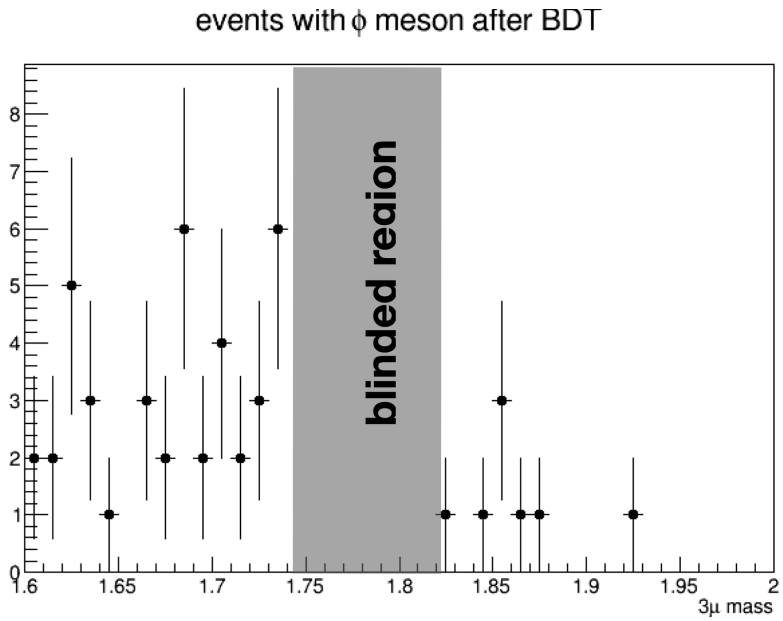

Figure 3.28: Distribution of the tau candidate invariant mass of the events selected by the BDT; only signal candidates where the opposite-sign muons are compatible with a $\phi \to \mu\mu$ decay are plotted.

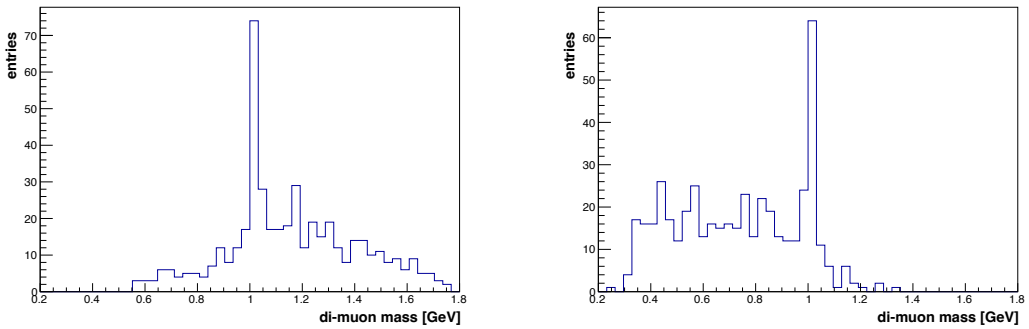

Figure 3.29: Distribution of the biggest (right) and smallest (left) invariant mass values of opposite-sign muon couples passing the BDT selection in data.

3.1.6 Exclusion limits

The $\tau \to 3\mu$ signal, if present, should manifest as a peak centred on the nominal mass of the tau $m_\tau = 1.777$ GeV in the three-muon mass distribution. Therefore, the three-muon mass is chosen as most discriminating observable to be processed in search for the signal.

The three-muon mass relative resolution[10] is used to define three mutually exclusive categories, which will be called category A, B and C. These categories are defined with their boundaries at the values of 0.7% and 1.2%, which roughly correspond to the pseudorapidity values 1 and 1.8. Figure 3.30 shows the distribution of the three-muon invariant mass relative resolution for signal and background events.

A simultaneous, unbinned maximum likelihood fit to the three categories is performed to extract the signal strength, which is fully correlated between the categories. The events considered for the fit are the events passing a certain BDT threshold; this threshold is defined as described in 3.1.6.

The background three-muon mass p.d.f. is an exponential function. The slope of this function is initially set by a fit to the sidebands, and it is constrained by a gaussian function (with a width given by the error of the estimation of the slope). The normalization of the background is left completely unbound, so that the fit can freely adjust it at no cost to the likelihood.
The signal p.d.f. is a gaussian, whose mean and width are fixed to the values obtained by the MC samples.

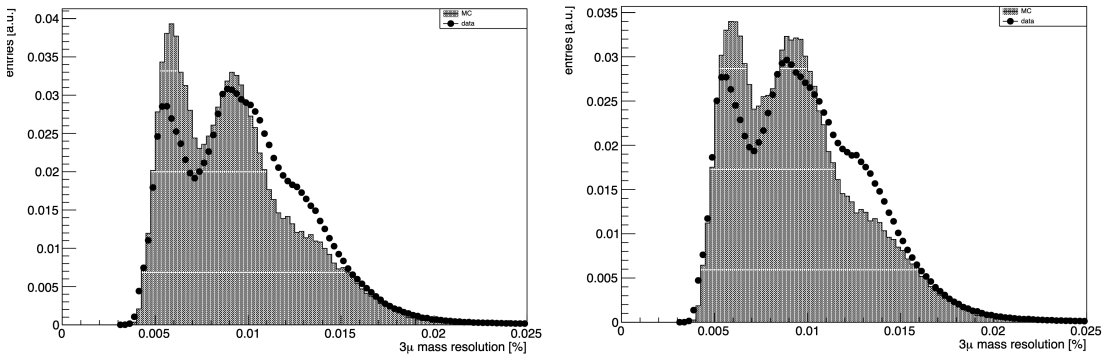

(a) *(b)*

Figure 3.30: Distribution of the relative mass resolution of the signal candidates evaluated on background (points) and signal (shaded area) samples for 2017 (left) and 2018(right)

[10]The relative mass resolution on the three-muon final state is defined as the ratio of the invariant mass uncertainty (obtained from the fit of the muon tracks to a common vertex) and the invariant mass itself.

Working point optimization

The BDT working point defines, for each category, the BDT score threshold used to mark $\tau \to 3\mu$ candidates as signal. Only events identified as signal are used to compute the final result.
The value of the working points is optimized with respect to the expected upper limit in each category. To do so, a scan of the expected upper limit is performed as a function of the score threshold of category A and B, and later for category C alone. The procedure used to compute the expected upper limit is described in App. A. This study is carried out separately for the 2017 and 2018 datasets.
Figure 3.31 shows the optimization result for 2017 and 2018, for the A and B categories. Figure 3.32 shows the optimization result on category C.
The working points chosen for the analysis are 0.991 (0.995) for category A, 0.994 (0.998) for category B, and 0.992 (0.994) for category C, for the year 2017 (2018).

A similar optimization has been done for the mass windows used to exclude $\phi \to \mu\mu$ events; the mass window around the ϕ mass (1020 MeV) has been optimized with respect to the expected upper limit in each category. Figure 3.33 and Fig. 3.34 show the result for the 2017 and 2018 years. The value of 20 MeV has been chosen as best cut for each category and each year, so that the vetoed window around the ϕ mass is 40 MeV large.

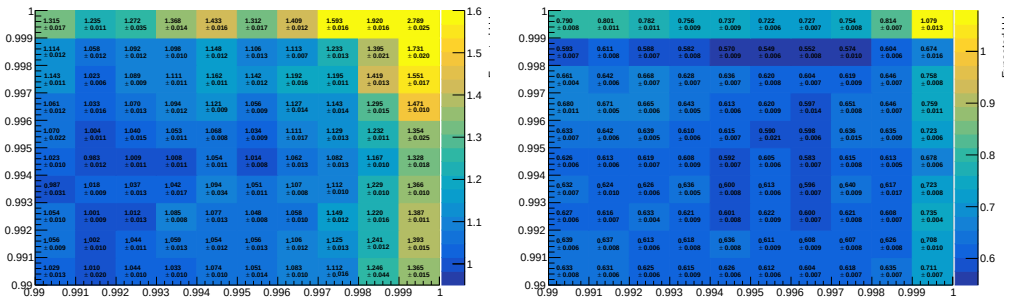

(a) *(b)*

Figure 3.31: Scan of the expected upper limit value (color bar) as a function of the BDT score thresholds on category A (horizontal axis) and B (vertical axis), for the 2017 (left) and 2018 (right) datasets. The bin with the lowest UL estimation is chosen as the working point of the analysis.

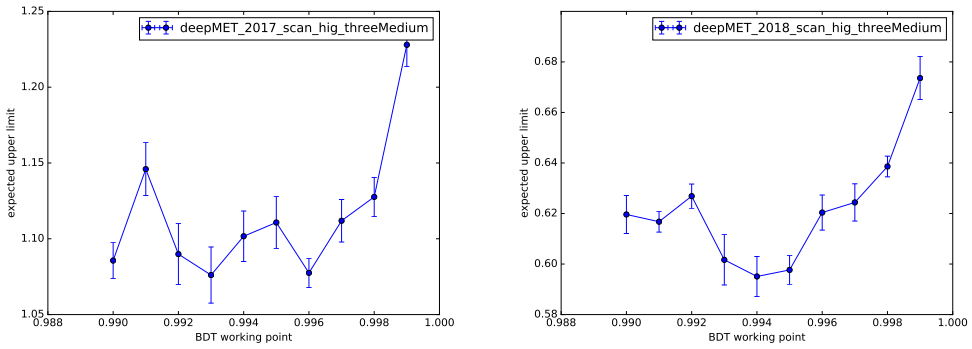

(a) *(b)*

Figure 3.32: Scan of the expected upper limit as a function of the BDT score thresholds on category C, for the 2017 (left) and 2018 (right) datasets. The bin with the lowest UL estimation is chosen as the working point of the analysis.

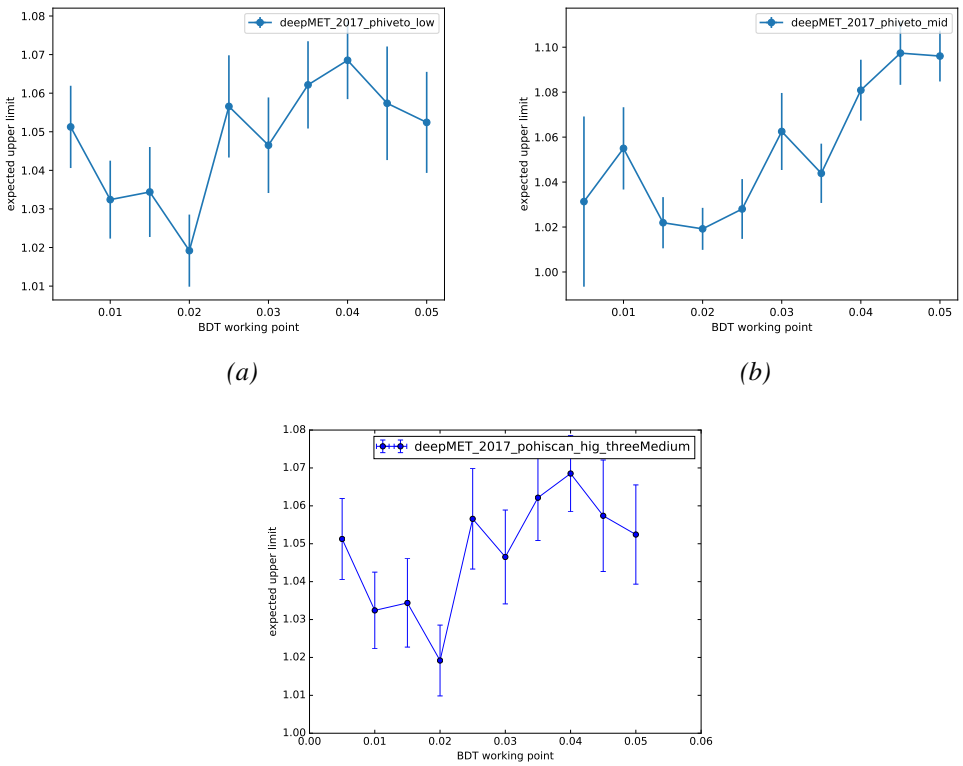

(a) *(b)*

(c)

Figure 3.33: Scan of the expected upper limit as a function of the $\phi \to \mu\mu$ veto mass window applied to signal muon couples for the 2017 dataset. The plots show this optimization for events falling into category A (upper left), B (upper right), and C (bottom central). The bin with the lowest UL estimation is chosen as the working point of the analysis.

s

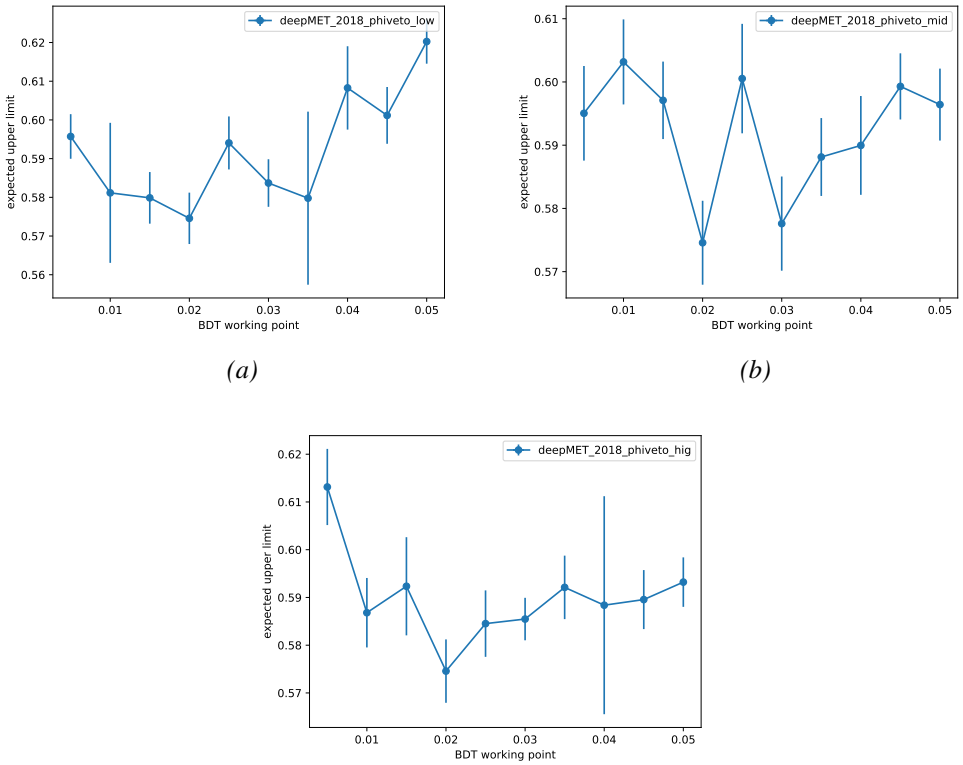

(a) *(b)*

(c)

Figure 3.34: Scan of the expected upper limit as a function of the $\phi \to \mu\mu$ veto mass window applied to signal muon couples for the 2018 dataset. The plots show this optimization for events falling into category A (upper left), B (upper right), and C (bottom central). The bin with the lowest UL estimation is chosen as the working point of the analysis.

Systematic uncertainties

Theoretical and experimental systematic uncertainties are represented in the likelihood fit by nuisance parameters, and affect mainly the signal MC as normalization uncertainties with log-normal priors (log-normal functions are chosen as priors as the normalization coefficients are positive). We evaluated the impact of the muon identification correction (both online and offline), of the uncertainties on the luminosity, pp$\rightarrow$W cross section, and W$\rightarrow \tau\nu$ and W$\rightarrow \mu\nu$ branching fraction values assumed to normalize the signal sample, of the finite statistics of the simulated sample, of the error on the evaluation of the HLT isolation scale factor, and of the NLO reweighing.
A 2.3% (2.7%) uncertainty [77, 78] on the total integrated luminosity of 2017 (2018) is considered. The signal is normalized using the CMS measurement of σ(pp$\rightarrow$W) $\times$ BR(W$\rightarrow \tau\nu$) at 13 TeV [37] and multiplying this value by the ratio BR(W$\rightarrow \tau\nu$) / BR(W$\rightarrow \mu\nu$) as reported by the Particle Data Group [79], using the formula of Eq. 1.46. The total uncertainty on the measured σ(pp$\rightarrow$W) $\times$ BR(W$\rightarrow \mu\nu$), corresponding to 3.7%, is assumed together with an uncertainty of 2.1% on BR(W$\rightarrow \tau\nu$).
The per-muon uncertainties on the muon scale factors are obtained from the studies described in Sec. 3.1.3. The systematic error associated to the re-weighting of the signal yield is computed varying up and down the weights associated to each muon by their error and taking the relative signal yield difference with respect to the nominal yield as the systematic uncertainty. The same approach is adopted for the generated W boson spectrum correction, and the NLO reweighing uncertainty amounts to 4%.

The offline muon identification uncertainty amounts to 1.4% (1.4%) in category A, 2.1% (2.1%) in category B and to 4.6% (4.5%) in category C for the 2017 (2018) period.
The online muon identification uncertainty amounts to 0.7% (0.8%) in category A, 0.8% (1.1%) in category B and to 1.9% (1.9%) in category C for the 2017 (2018) period. Moreover, a 12% (7%) uncertainty, defined as the error associated to the measurement described in Sec. 3.1.3, is associated to the HLT isolation correction.
The systematic uncertainty associated to the finite MC statistics amounts to 1.0% (0.7%) in category A, 0.7% (1.2%) in category B and to 1.1% (1.2%) in category C for the 2017 (2018) period.

The uncertainty associated to the mismodeling of the signal properties (mean value and width) has been studied comparing Ds$\rightarrow \phi(\mu\mu)\pi$ events between data and MC. The samples used for data are selected by *double-muon* triggers, the samples used for the MC are Ds$\rightarrow \phi(\mu\mu)\pi$ samples simulated under the same conditions of the signal sample. Figure 3.35 shows the result of the comparison. The difference in the mean value is only

0.2%; the mean value is considered well-modelled and not studied further. The width can be mismodeled up to 6% (category C), with MC simulations yielding a larger value. To study the impact of this mismodeling, the width of the MC sample used to model the signal has been scaled down by 6% in all categories, and the expected upper limit has been compared to the original one. The observed difference is lower than 0.1%, thus no systematic uncertainty is assigned to the signal mismodeling.

Since no prior knowledge of the background is assumed, the slope of the exponential is passed to the fit as a parameter with a gaussian constraint and its normalisation as an unconstrained rate parameter, that is the background is constrained by the data without any penalty to the likelihood.
Systematic uncertainties are summarised in Tab. 3.7.

Table 3.7: Summary of systematic uncertainties for 2017 (2018).

Source of uncertainty	process	type - constrain	cat. A	cat. B	cat. C	correlated
luminosity	sig.	rate - logN	2.3% (2.5%)	2.3% (2.5%)	2.3% (2.5%)	yes
$\sigma(pp \to W)$	sig.	rate - logN	3.7%	3.7%	3.7%	yes
$\mathscr{B}(W \to \tau\nu)$	sig.	rate - logN	0.15%	0.15%	0.15%	yes
$\mathscr{B}(W \to \mu\nu)$	sig.	rate - logN	0.21%	0.21%	0.21%	yes
finite MC statistics	sig.	rate - logN	1.0% (0.7%)	0.7% (0.5%)	1.1% (1.2%)	no
offline muon identification	sig.	rate - logN	1.4% (1.4%)	2.1% (2.1%)	4.6% (4.5%)	no
online muon identification	sig.	rate - logN	0.7% (0.8%)	0.8% (1.1%)	1.9% (1.9%)	no
HLT isolation correction	sig.	rate - logN	12% (7%)	12% (7%)	12% (7%)	yes
NLO reweighing	sig.	rate - logN	4% (4%)	4% (4%)	4% (4%)	yes
slope of the exponential	bac.	model - gaussian	-	-	no	no
background normalisation	bac.	rate - unconstrained	-	-	no	no

Sanity checks on the Asimov dataset

To ensure the sanity of the procedure and workflow adopted to compute the final result, some checks have been performed on the Asimov dataset[11].
In general, the values and errors on the nuisance parameters are set by independent measurement, so these parameters are expected not to be constrained by the fit. Thus, the values of the nuisance parameters and the ratio of their uncertainties before and after the fit of the model to the Asimov dataset are compared. This test is computed both under the background-only hypothesis (i.e., setting the signal strength to zero) and the signal-plus-background hypothesis (i.e., setting the signal strength to one).
Figures 3.36 and 3.37 show the pre-fit, background-only fit and signal-plus-background

[11]The Asimov dataset is a dataset generated using the pre-fit values of the model (that is, the values used to initialize the model) neglecting the statistical fluctuations.

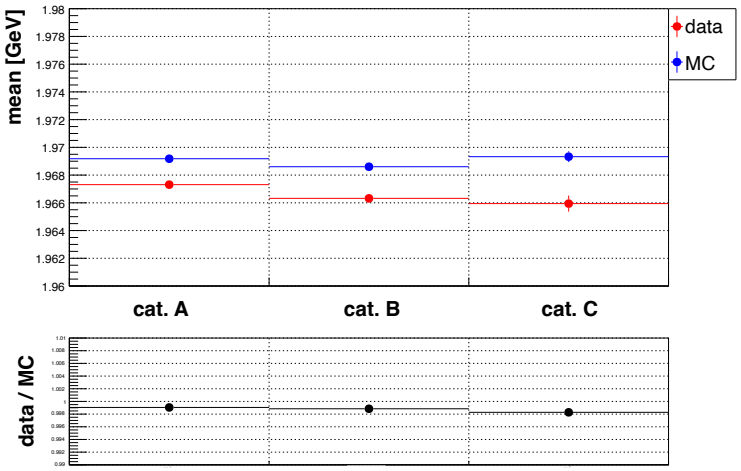

(a)

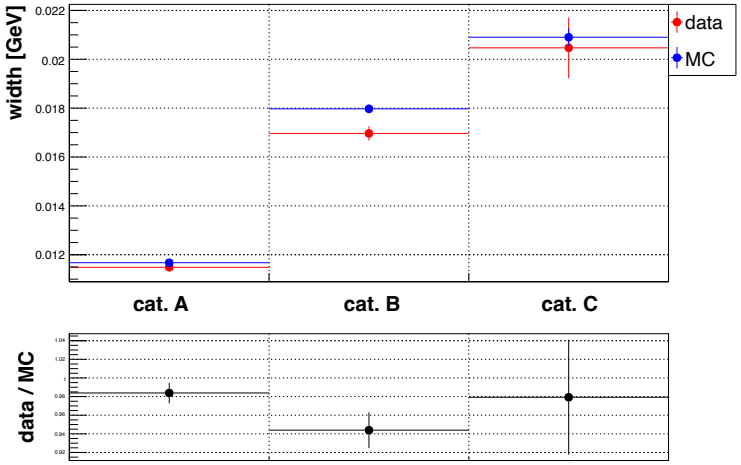

(b)

Figure 3.35: Fig. a) the upper pad shows the fitted value of the Ds meson mass in the Ds$\to$ $\phi(\mu\mu)\pi$ channel on data (red) and MC (blue) samples for the three analysis categories (three bins in the plot), the lower pad shows their ratio. Fig. b) the upper pad shows the fitted value of the Ds meson width in the Ds$\to$ $\phi(\mu\mu)\pi$ channel on data (red) and MC (blue) samples for the three analysis categories (three bins in the plot), the lower pad shows their ratio. These studies are conducted on the 2017 and 2018 datasets together.

fit to the Asimov datasets generated under the two hypotheses. The value of the signal strength obtained by the fit to the Asimov sample generated with a null signal is $0.003^{+0.294}_{-0.003}$, and the value obtained by the fit to the Asimov sample generated with a signal component is $1.000^{+0.479}_{-0.399}$. Both the values are in full agreement with the Asimov truth.

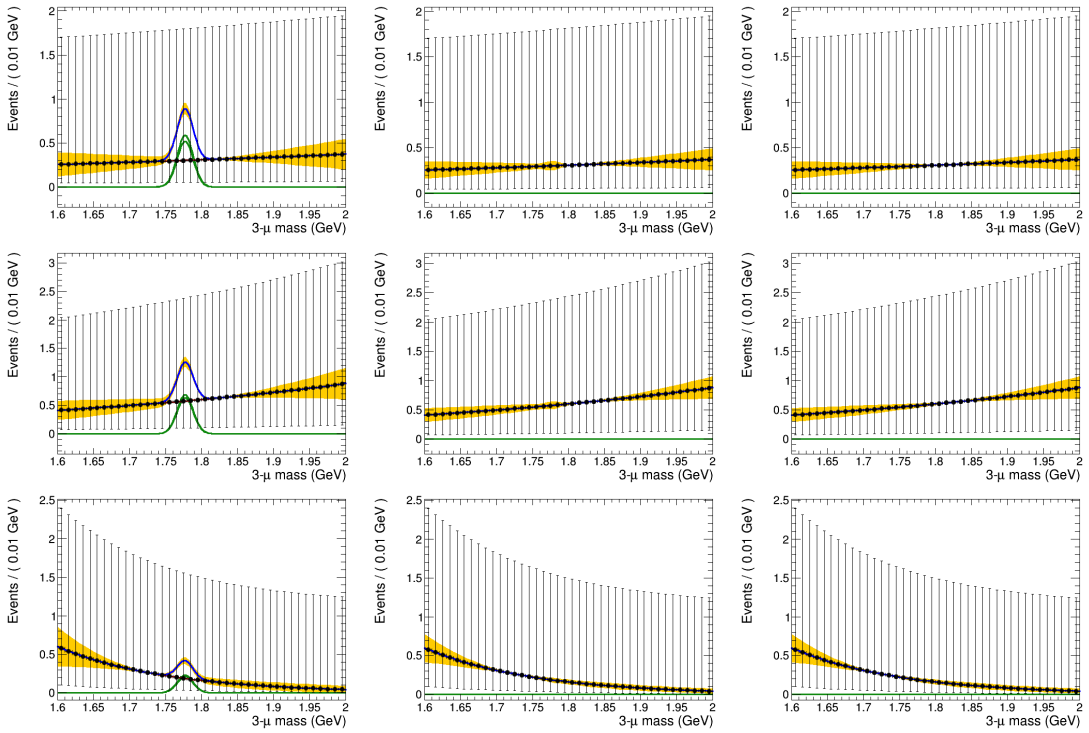

Figure 3.36: Studies on the Asimov dataset generated under the background-only hypothesis. The picture shows the pre-fit values of the analysis model on the Asimov dataset (first column), the signal-plus-background model fitted to the Asimov dataset (second column), and the background-only model fitted to the Asimov dataset (third column), for category A (first row), category B (second row) and category C (third row). All the fits are successful and reproduce the Asimov truth.

Figure 3.38 shows the pulls and ratio obtained from the signal-plus-background fit to the Asimov datasets[12]. As expected, the pulls of the nuisances are zero, and the error ratios are one. The only exception are the parameters used to model the background slope in

[12]In the picture, *a0* indicates the slope of the exponential function used to model the background, *bkgNorm* is the normalization scale factor associated to the background model, *HLT_iso* is the systematic uncertainty related to the HLT isolation correction, *xs_W* is the systematic uncertainty associated to the pp$\to$W, W$\to \mu\nu$ cross section value, *Lumi* is the systematic uncertainty associated to the integrated luminosity value, *mc_stat* is the systematic uncertainty associated to the MC sample size, and *br_Wtaunu* is the systematic uncertainty associated to the W$\to \tau\nu$ branching fraction value. Most of the nuisance parameters differ in the categories; in such cases, a subscript indicates the category name and year.

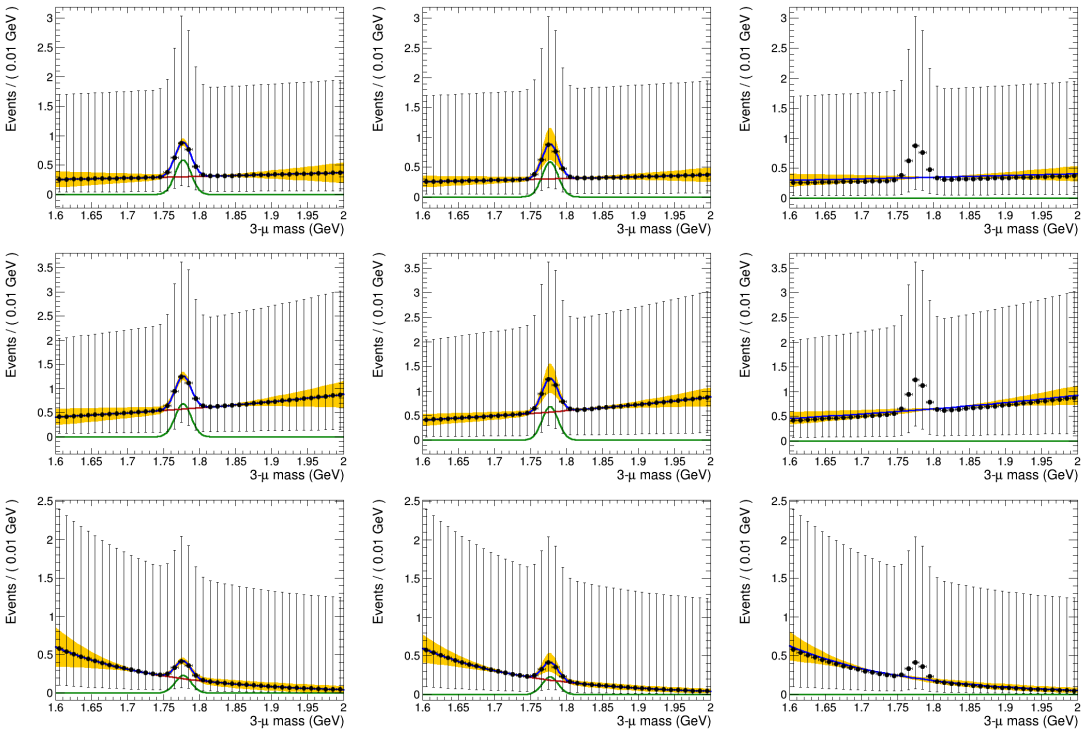

Figure 3.37: Studies on the Asimov dataset generated under the signal-plus-background hypothesis. The picture shows the pre-fit values of the analysis model, plotted on the Asimov dataset (first column), the signal-plus-background model fitted to the Asimov dataset (second column), and the background-only model fitted to the Asimov dataset (third column), for category A (first row), category B (second row) and category C (third row). All the fits are successful and reproduce the Asimov truth. The background-only fits overestimate the slope of the exponential to compensate for the signal peak present in the Asimov dataset(as expected).

each category, which show an error ratio of the pre-fit and post-fit values lower than one. This behaviour is expected since the pre-fit values are obtained through a fit to the data sidebands, while the post-fit values are obtained through a fit including also the signal region of the Asimov dataset; this brings to a smaller uncertainty to the estimation of the exponential parameters due to the additional information added to the fit.

Results

Branching ratio exclusion limits are determined at the 90% CL[13] following the CLs approach, as described in App. A. At the time this thesis was written, the analysis was still under the collaboration internal review, thus only expected results, computed excluding the signal region from the data[14], can be stated. Figure 3.39 shows the invariant mass distribution of the $\tau \to 3\mu$ candidates identified as signal by the BDT. For the reason stated above, the signal region is blinded, and the MC distribution of signal events is displayed instead (normalized to $\mathscr{B}(\tau \to 3\mu) = 10^{-7}$). The results are summarized in Tab. 3.8, and the overall upper limit set by the W channel on the $\tau \to 3\mu$ process is

$$\mathscr{B}(\tau \to 3\mu) < 4.4 \times 10^{-8} \quad at\ 90\%\ of\ C.L. \tag{3.5}$$

The 68% and 95% confidence intervals on the estimation of the expected upper limit are respectively (3.2, 6.5) and (3.1, 9.6) in units of 10^{-8} at 90% of CL. Table 3.9 shows the expected signal and background yields in the categories of the W analysis in units of 10^{-8} at 90% of CL.

Table 3.8: Expected upper limit in each of the analysis categories, computed in units of 10^{-8} *at 90% of CL.*

year	category A	category B	category C
2017	21.1	26.1	60.3
2018	10.1	12.3	28.1

3.2 The heavy flavour channel

In parallel with the W channel study, an analysis of $\tau \to 3\mu$ from *heavy flavours* (HF) (B and D mesons) has been performed within CMS. The two channels present some

[13]The choice of 90% over 95% CL is motivated by the intention to be consistent with the existing literature and to make the comparison easier.

[14]This procedure is known as *blinding*.

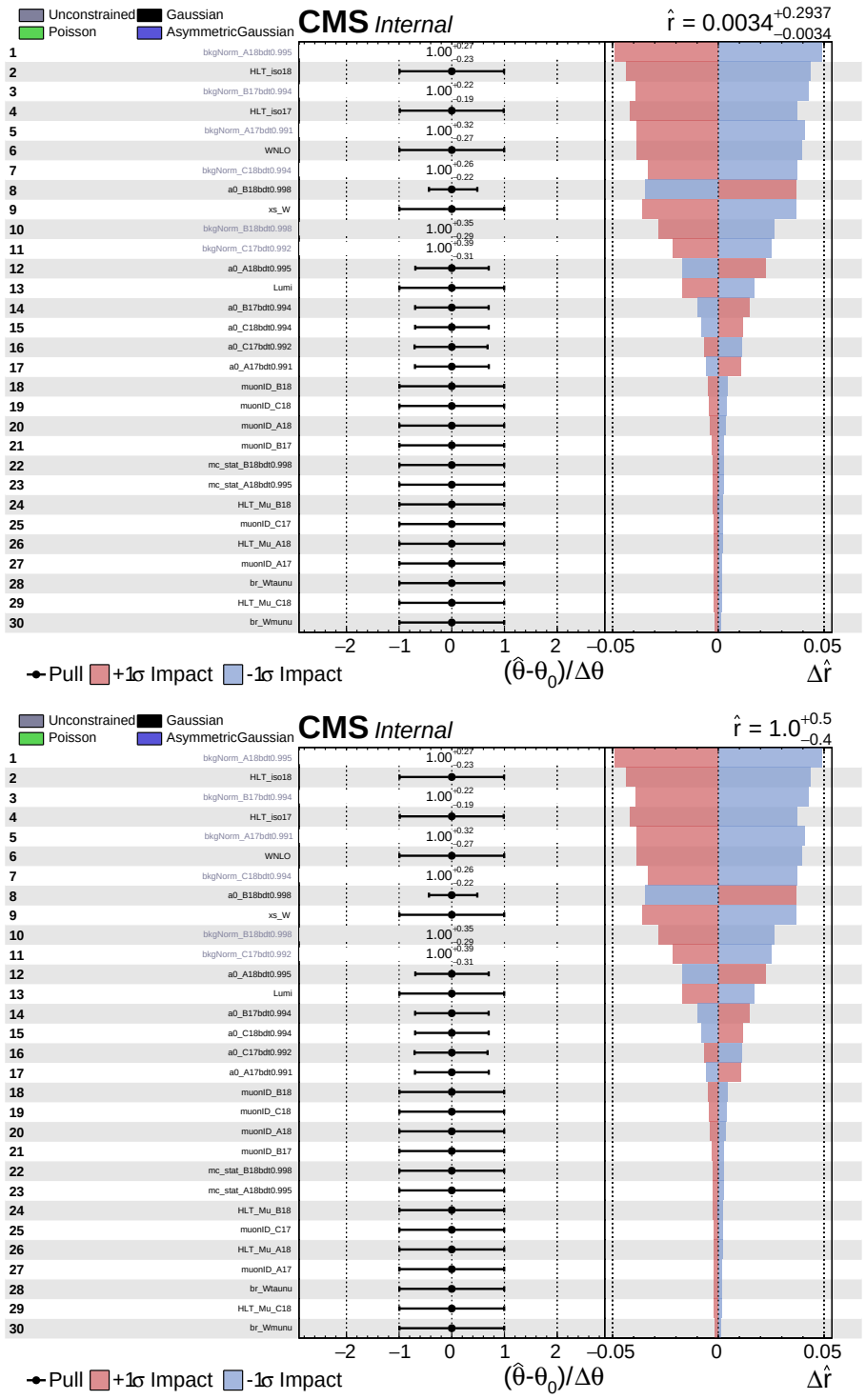

Figure 3.38: Pulls and impacts of the analysis nuisance parameters evaluated on an Asimov dataset generated under the background-only hypothesis (upper plot) and under the signal-plus-background hypothesis (lower plot). Each plot shows the list of the nuisance parameters (left column), their pulls and the error ratios (central column) and their impact (right column). The fitted value of the signal strength is also shown in the upper-right corner of each plot. Low-impact parameters are not shown.

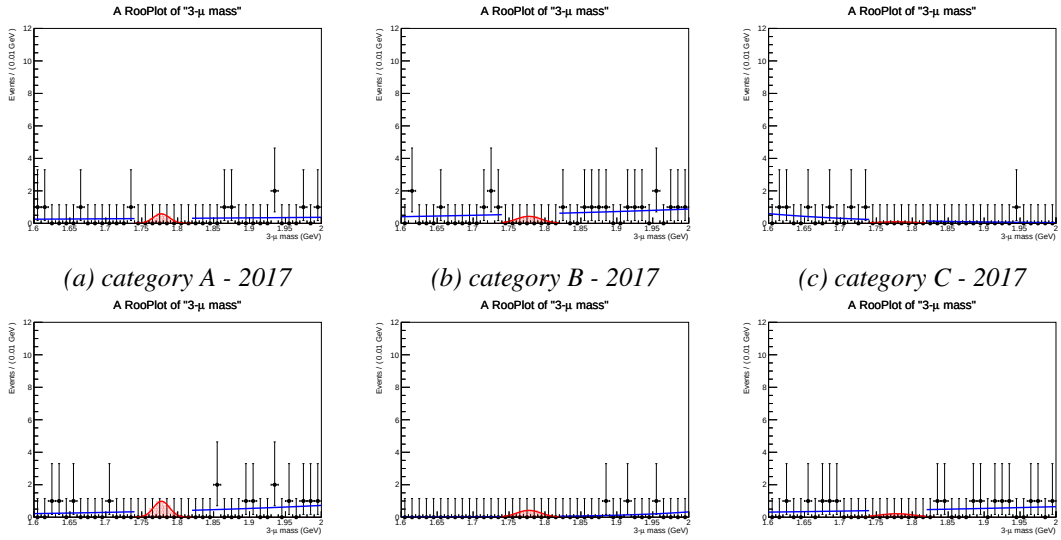

(a) category A - 2017 *(b) category B - 2017* *(c) category C - 2017*

(d) category A - 2018 *(e) category B - 2018* *(f) category C - 2018*

Figure 3.39: Invariant mass distribution of the signal candidates passing the W channel preselection and BDT selection steps described in Chap. 3.1. The signal region is blinded and the MC sample is plotted instead, normalized to $\mathcal{B}(\tau \to 3\mu) = 10^{-7}$.

Table 3.9: Expected number of signal (background) events in each of the analysis categories.

year	category A	category B	category C
2017	1.4 (12.4)	1.7 (24.6)	0.6 (8.5)
2018	3.2 (17.1)	2.1 (10.3)	1.7 (18.5)

common issues and, of course, some peculiar aspects. I contributed to the synchronization of the two channels. I present here a short outline of the HF analysis and the related expected limit before discussing the two channel combination.

3.2.1 Analysis outline

The HF analysis follows a workflow similar to that applied to the W channel.
However, a first fundamental difference lies in the trigger used to select events online, developed to target the softer kinematics of the HF channel. The trigger paths used are HLT_DoubleMu3_Trk_Tau3mu (online during 2017) and HLT_DoubleMu3_TkMu_DsTau3Mu (online during 2018), and present the following requirements:

- two L3 muons with with transverse momentum greater than 3 GeV
- one track (one tracker muon for 2018) with transverse momentum greater than 1.2 GeV
- an invariant mass of the three-body state between 1.6 GeV and 2.02 GeV
- a vertex displacement of the three tracks from the beamspot in the transverse plane greater than two times its error

Both HLT paths are seeded by single-muon, double-muon and triple-muon L1 seeds: The analysis is conducted on events selected by those triggers, which collected an integrated luminosity of 38 fb^{-1}during 2017 and 59.8 fb^{-1}during 2018.
Data events are then processed offline; signal candidates are formed using three-muon candidates with the following requirements:

- the signal candidate has unitary electric charge
- the three signal muons form a valid secondary vertex (i.e. with a χ^2 lower than 100) with a displacement from the primary vertex greater than twice its position uncertainty (3.75 times for the 2018 datasets)
- each signal muon pair has a radial distance $\sqrt{\Delta\phi^2 + \Delta\eta^2}$lower than 0.8

- each signal muon pair has a maximum separation in the z coordinate lower than 0.5 cm (evaluated extrapolating the muon tracks inward, towards the beam line)
- the signal candidate has an invariant mass value between 1.6 GeV and 2.0 GeV
- the three signal muons should match (as already described in Sec.3.1.2) the HLT objects which fired the trigger with a maximum radial distance of 0.03 and a maximum p_T difference of 10%

Events in the HF channel are split into two non-overlapping classes: one containing three global muons and one containing two global muons and one tracker muon. As the transverse momentum of the signal muons originating from HF decays is very soft, standard muon flags are not able to guarantee an acceptable purity while keeping a good selection efficiency. For this reason, the analysis employs dedicated MVA discriminators to select global and tracker muons, which have shown better performance in the phase space of the analysis if compared to the common tools employed at CMS. These discriminators are BDT's trained on real and fake muon simulated samples, using detector information related to the muon track quality.

Events are divided, for both classes, into three categories (labelled A, B and C) based on the signal candidate relative mass resolution; the values 0.7% and 1.5% are chosen as thresholds to define these categories; these values are chosen to match the mechanical configuration of the muon sub-detectors (central, overlap and forward regions, which present different detection technologies, as explained in Sec. 2.2.4)
Signal candidates are later selected by a per-event BDT, which reduces the background contamination. The BDT is trained using signal candidates coming from the analysis sidebands[15] for the background and simulated $\tau \to 3\mu$ samples from D_s and B mesons decays for the signal.
Two versions of the BDT are created for the two different classes of the analysis, both with dedicated trainings for each category. Based on the BDT score distribution, three sub-categories are defined for each category of the three-global class and two for each category of the two-global-plus-one-tracker class. The sub-categories are labelled 1, 2 and 3, so that the analysis categories are A1, A2, A3, B1, B2, etc. Figure 3.40 shows the score distribution of the per-event BDT, showing the sub-category splits. Events not falling into one of these categories (i.e. events with a low BDT score) are considered background and are rejected. The remaining events are used to compute the expected upper limit on the $\tau \to 3\mu$ branching ratio.

[15]The sidebands of the analysis are defined as the regions of the three-muon invariant mass between 1.6 GeV and 1.74 GeV, and between 1.82 GeV and 2.0 GeV.

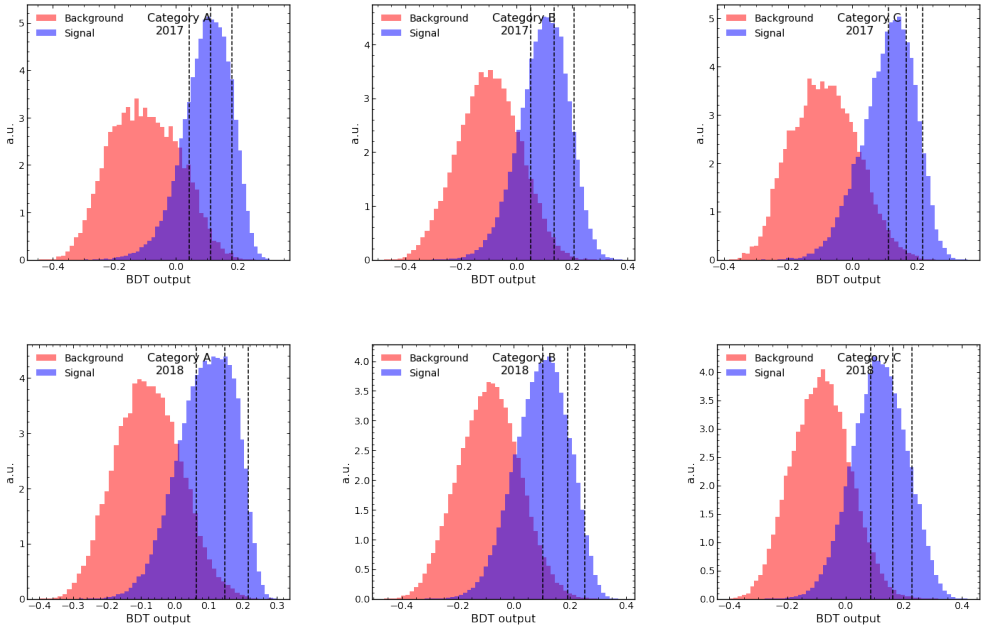

Figure 3.40: Distributions of the three-global class per-event BDT score evaluated on background (red) and signal (blue) events in 2017 (upper plots) and 2018 (lower plots) samples, for category A (left), B (central) and C (right). The vertical lines indicate the separation for the sub-categories 1, 2 and 3. Candidates not falling into one of the three sub-categories (i.e. with a per-event BDT score lower than the leftmost threshold) are considered as background events and rejected.

The upper limit is computed following the same approach used by the W channel (the CLs method using the LHC test statistics - see App. A), using the invariant mass of the signal candidate as discriminating variable. The background p.d.f. is modeled with an exponential function, while the signal with a gaussian. The signal width and mean are fixed to the $\tau \to 3\mu$ MC samples; the signal normalization is computed from the Ds$\to \phi(\mu\mu)\pi$ yield using the formulae:

$$N_{sig}^{D_s} = N_{norm} \quad \frac{\mathscr{B}(D_s \to \tau\nu)}{\mathscr{B}(D_s \to \phi(\mu\mu)\pi)} \frac{\mathscr{A}_{3\mu}}{\mathscr{A}_{2\mu\pi}} \frac{\varepsilon_{3\mu}^{reco}}{\varepsilon_{2\mu\pi}^{reco}} \frac{\varepsilon_{3\mu}^{2\mu trig}}{\varepsilon_{2\mu\pi}^{2\mu trig}} \mathscr{B}(\tau \to 3\mu) \tag{3.6}$$

$$N_{sig}^{B^+} = f\, N_{norm} \quad \frac{\mathscr{B}(B \to \tau X)}{\mathscr{B}(D_s \to \phi(\mu\mu)\pi)\mathscr{B}(B \to D_s X)} \frac{\mathscr{A}_{3\mu}}{\mathscr{A}_{2\mu\pi}} \frac{\varepsilon_{3\mu}^{reco}}{\varepsilon_{2\mu\pi}^{reco}} \frac{\varepsilon_{3\mu}^{2\mu trig}}{\varepsilon_{2\mu\pi}^{2\mu trig}} \mathscr{B}(\tau \to 3\mu) \tag{3.7}$$

where N_{norm} is the measured $D_s \to \phi(\mu\mu)\pi$ yield, $\mathscr{A}$ is the detector acceptance, ε^{trig} and ε^{reco} are the trigger and reconstruction efficiencies, and f is the fraction of D_s mesons in b hadron decays and the branching fraction of the $\tau \to 3\mu$ process is assumed to be 10^{-7}. The value 10^{-7} is only used to scale the final result to reasonable units, as the CMS sensitivity is expected to be near 10^{-8}) and make the distribution of MC events visible in the plots; it does not affect the final result in any way. The fraction f is estimated with a fit to the proper decay length distribution of the D_s meson, distinguishing the contribution of prompt D_s mesons and of those originating from a B meson decays ($B \to D_s$) (targeting Ds$\to \phi(\mu\mu)\pi$ decays); the shape of the two categories is obtained from MC simulations and fit to data, as shown in Fig. 3.41. The contribution for the smaller production channels $D^+ \to \tau^+ X$ and $B_s \to \tau X$ is estimated using the simulation software Pythia. To count for those contributions, the signal yield of the main channels D_s and B^+ is augmented respectively by 4% and 12%, with an associated systematic error of 100%. Different sources of mismodeling are taken into account and addressed as normalization nuisance parameters, with an associated systematic uncertainty. They include: global and tracker MVA muon identification (studied with the tag-and-probe strategy on J/$\psi \to \mu^+\mu^-$ events, as done for the W channel - see Sec. 3.1.3), signal normalization (due to the uncertainty on the hadron decay branching fraction and on the detector acceptance and efficiency - see Eq. 3.7), L1 trigger efficiency (studied comparing the data and MC yields of the Ds$\to \phi(\mu\mu)\pi$ process), BDT selection (studied comparing the BDT efficiency on Ds$\to \phi(\mu\mu)\pi$ events). Table 3.10 lists the sources of systematic uncertainty and their impact on the signal yield.

The background model is initialized by a fit to the sidebands; its normalization and slope parameters are unconstrained in the model.
The upper limit is computed using signal candidates selected as described above, falling

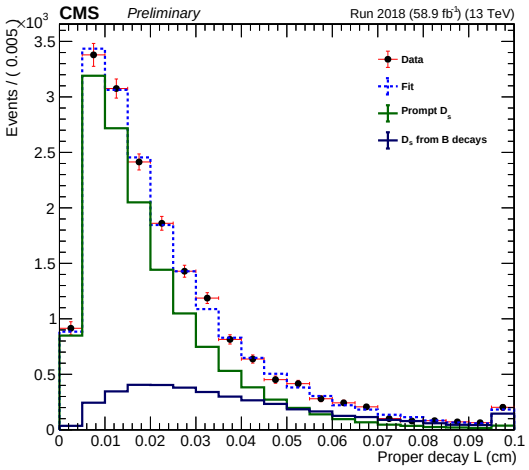

Figure 3.41: Proper decay length distribution of $D_s \to \tau\nu$ events evaluated on data (points), on prompt D_s simulated events (blue) and on simulated D_s events coming from B meson decays (green). The MC distributions are fit to the data to obtain the non-prompt fraction of D mesons; the fit result is shown with a dashed blue line.

Table 3.10: Sources of systematic uncertainties of the HF analysis and their impact on the signal yield.

Source of uncertainty	impact 2017	impact 2018
B($D_s \to \tau\nu$)	3%	3%
B(Ds$\to \phi(\mu\mu)\pi$)	8%	8%
B($B \to D_s + X$)	5%	5%
B($B \to \tau + X$)	3%	3%
B-to-D ratio f	3%	3%
Scaling D_s to include D_+	3%	3%
Scaling B^0 and B^+ to include B_s	4%	4%
Number of events triggered by tri-muon trigger	3%	3%
Ratio of 3μ and $2\mu\pi$ acceptances	1%	1%
Muon identification efficiency	1.5%	1.6%
BDT cut efficiency	9%	4%

in one of the per-event BDT sub-categories. Figure 3.42 and Fig. 3.43 show the mass plots of the BDT-selected signal candidates and the pre-fit values of the fit model for each category of the HF analysis. As the analysis was not approved at the time this thesis was written, only blinded results can be given.
The HF analysis obtained an expected upper limit on the $\tau \to 3\mu$ branching fraction equal to

$$\mathscr{B}(\tau \to 3\mu) < 3.2 \times 10^{-8} \quad at\ 90\%\ of\ C.L. \tag{3.8}$$

3.3 The combination

The combination of the HF and W channel is then preformed. The two channels are almost non-overlapping, with only one common event identified in the collected data (passing the full set of selections of the two analyses). This event is removed from the HF channel. Furthermore, some events from the W$\to \tau\nu$, $\tau \to 3\mu$ simulations can be selected by the HF analysis, while failing the W selections. If the $\tau \to 3\mu$ signal was present, these events would be reconstructed by the HF channel analysis, although they are not modeled by its simulations. Thus, the HF yield is incremented by the corresponding percentage, defined as the number of events coming from the W channel simulated samples which pass the HF channel selection but not the W channel selection, over the number of events coming from the HF channel simulated samples selected by the HF channel. These numbers are 6% for the 2017 sample and 4.4% for the 2018 sample. Vice versa, the contamination from signal events failing the HF analysis and selected by the W analysis is negligible, since the W channel selection (mostly the BDT step) is much tighter.
Since the two channels are statistically independent, the combination is preformed by mean of likelihood product. In addition, the analysis is also combined with the results obtained on 2016 data [5] with the same approach, thus completing the search for the $\tau \to 3\mu$ process on Run-II data. The expected upper limit on the $\tau \to 3\mu$ rate, obtained on the full Run-II statistics, is set to:

$$\mathscr{B}(\tau \to 3\mu) < 2.3 \times 10^{-8} \quad at\ 90\%\ of\ C.L. \tag{3.9}$$

Although only the expected upper limit can be given, as the analysis was under internal review at the time this thesis was written, the result is competitive with the world-best limit set by the Belle collaboration [3].

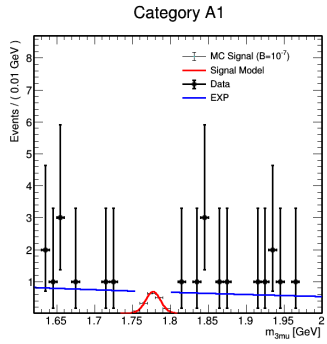

(a) cat. A1 - 2017

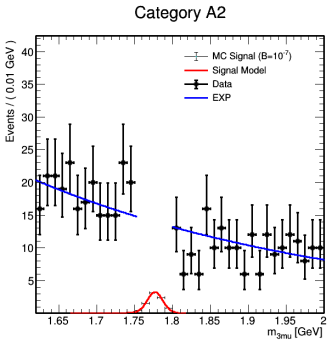

(b) cat. A2 - 2017

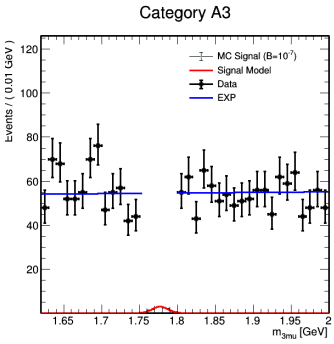

(c) cat. A3 - 2017

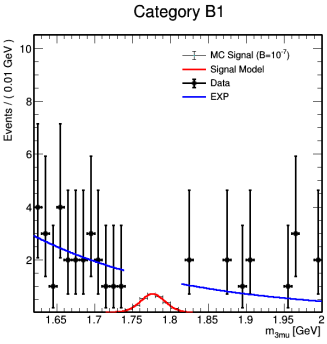

(d) cat. B1 - 2017

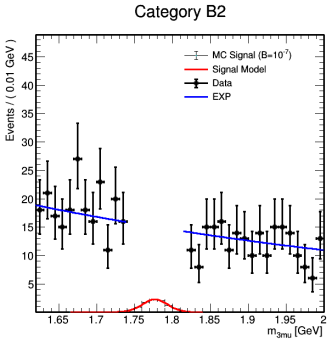

(e) cat. B2 - 2017

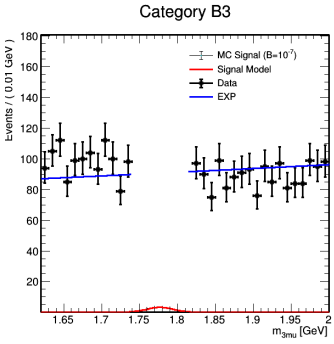

(f) cat. B3 - 2017

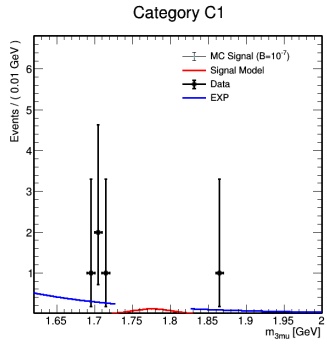

(g) cat. C1 - 2017

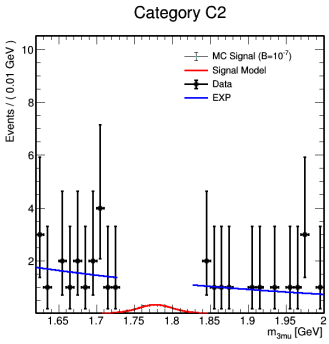

(h) cat. C2 - 2017

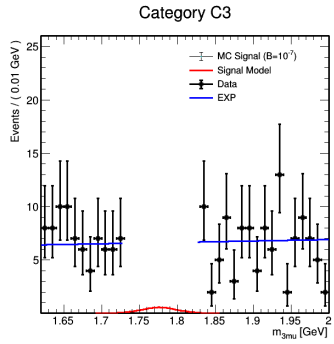

(i) cat. C3 - 2017

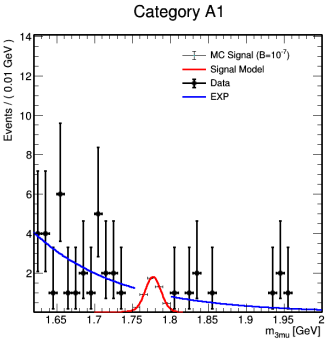

(j) cat. A1 - 2018

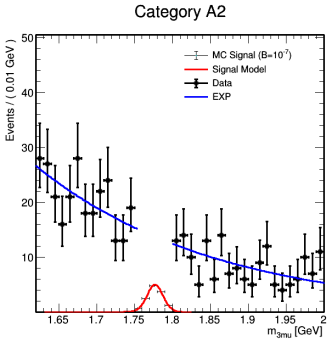

(k) cat. A2 - 2018

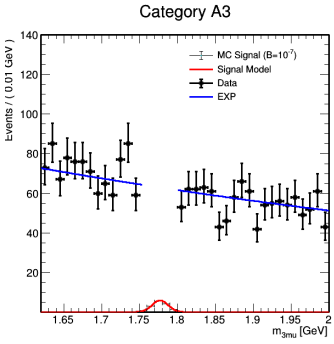

(l) cat. A3 - 2018

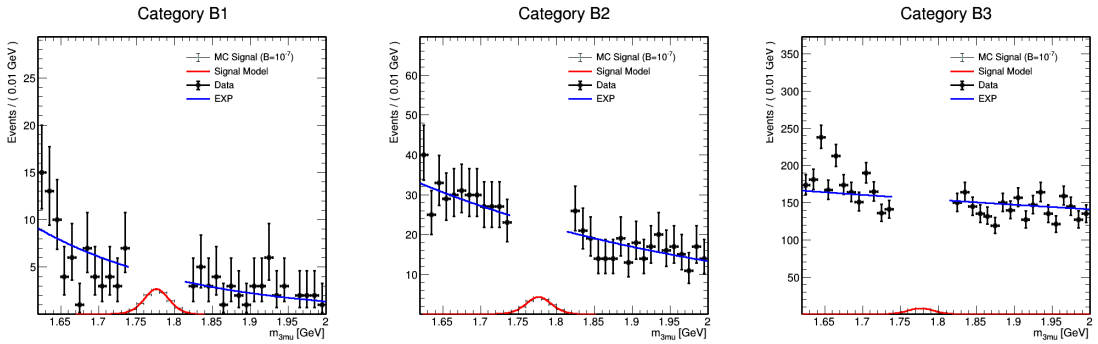

(m) cat. B1 - 2018 *(n) cat. B2 - 2018* *(o) cat. B3 - 2018*

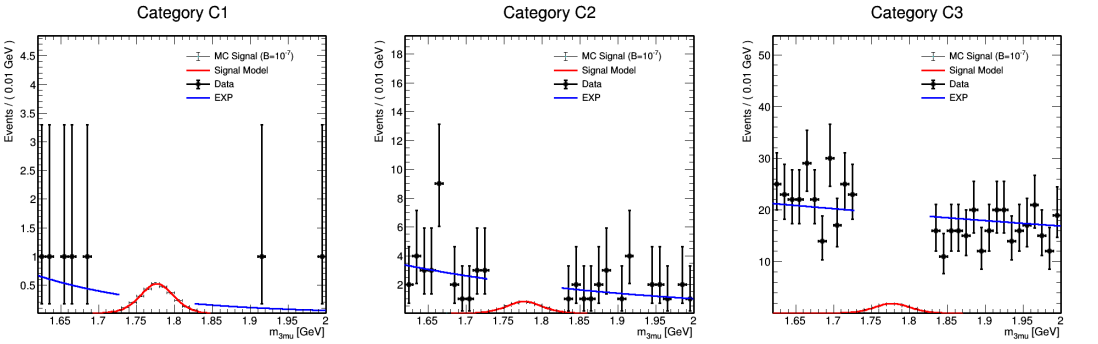

(p) cat. C1 - 2018 *(q) cat. C2 - 2018* *(r) cat. C3 - 2018*

Figure 3.42: Mass plots for the three-global class. The signal region is blinded. Black points represent data events, and the red histogram is the signal contribution coming from the simulated $\tau \to 3\mu$ sample normalized to $\mathscr{B}(\tau \to 3\mu) = 10^{-7}$.

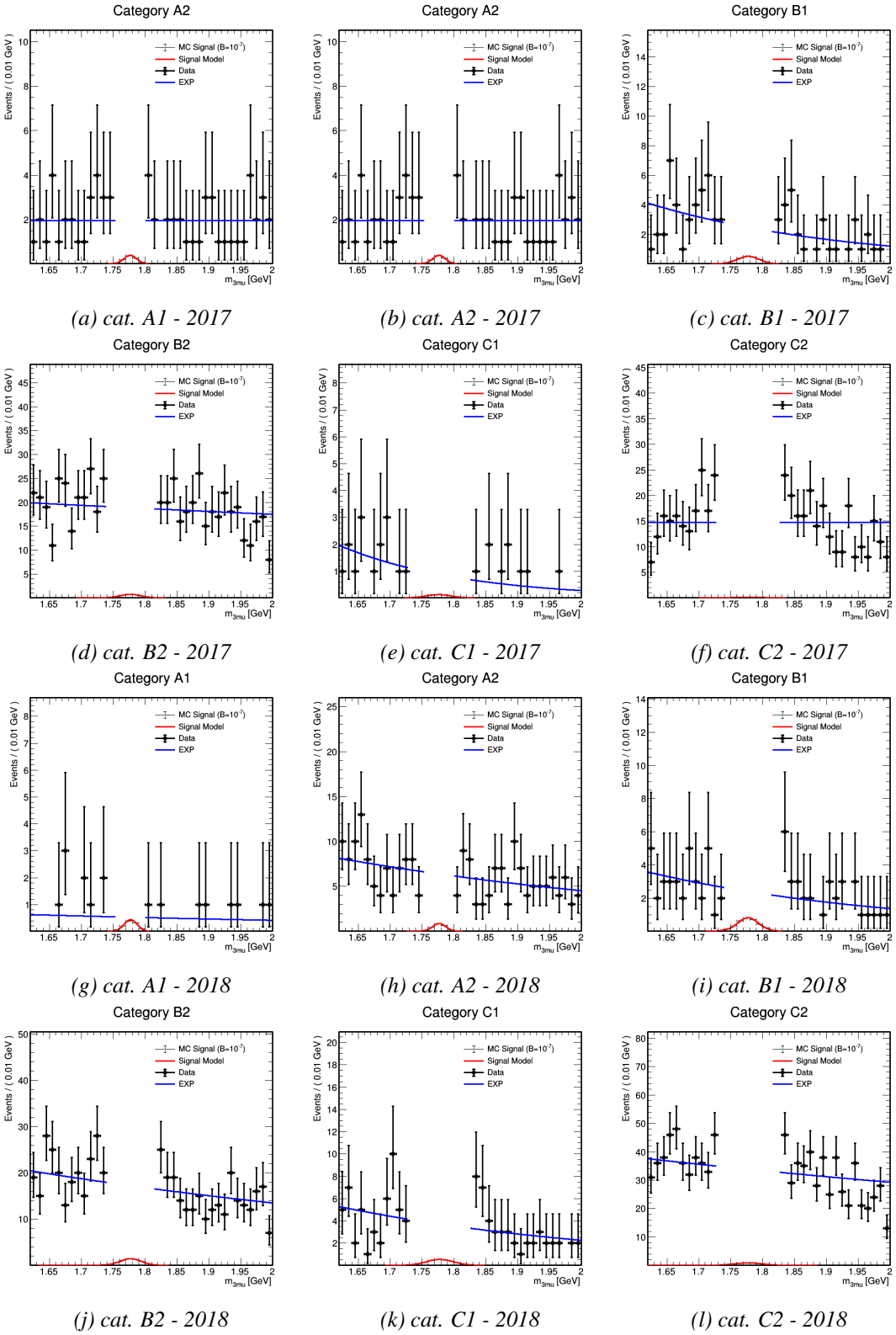

(a) cat. A1 - 2017 *(b) cat. A2 - 2017* *(c) cat. B1 - 2017*

(d) cat. B2 - 2017 *(e) cat. C1 - 2017* *(f) cat. C2 - 2017*

(g) cat. A1 - 2018 *(h) cat. A2 - 2018* *(i) cat. B1 - 2018*

(j) cat. B2 - 2018 *(k) cat. C1 - 2018* *(l) cat. C2 - 2018*

Figure 3.43: Mass plots for the two-global class. The signal region is blinded. Black points represent data events, and the red histogram is the signal contribution coming from the simulated $\tau \to 3\mu$ sample normalized at $\mathscr{B}(\tau \to 3\mu) = 10^{-7}$.

3.4 Conclusions

The search for the rare LFV process $\tau \to 3\mu$ has been discussed. The analysis has been carried out at CMS using proton-proton collision data at the centre of mass energy of 13 TeV, collected by the CMS experiment during Run-II (2016 to 2018). The analysis has exploited τ lepton coming from the W boson and D/B meson decays, merging the two production channel by likelihood combination. As the analysis is still under internal approval, only the expected upper limit to the $\tau \to 3\mu$ branching fraction can be reported. The value obtained is $\mathscr{B}(\tau \to 3\mu) < 2.3 \times 10^{-8}$ at 90% of confidence level.
This value is competitive with the limit observed by the Belle collaboration [3] (2.1×10^{-8} at 90% of confidence level), proving the impact that CMS can have on low-p_T analyses in search for new physics processes.
In Run-III (2022 to 2024) CMS will double the statistics and some improvements in the sensitivity are expected, pushing the limit to 10^{-8} at 90% of confidence level. A big improvement is expected to come from the new detector Belle-II [32], which relies on the recently upgraded e^+e^- collider SuperKEKB, promises to breach the threshold of 10^{-9}, thus leaving this analysis in the B-factories domain in the next years.
In a longer prospective, the hadronic colliders will re-enter the game. Indeed, the High-Luminosity LHC upgrade is scheduled to begin its activity in 2026, after the fourth long shutdown. It will collect an integrated luminosity of 3000 fb^{-1}, ten times the current reach, also achieving peaks of instantaneous luminosity five times larger than the current ones (see Fig. 3.45).
During this phase (known as Phase-II), the CMS detector will undergo major changes, pushing its performance even further. A new tracking system [80] will allow detection of charged particles in the forward region, extending its reach to the pseudorapidity value of 4. The improvements in the overall processing power and bandwidth of the detector, together with a dedicated tracker design [80], will enable the usage of tracking elements during data taking, and allow for the development of more sophisticated algorithms at trigger level.
A dedicated timing sub-detector, known as MIP timing detector (MTD) [81], will mitigate the impact of the high-luminous hadron activity, and allow to resolve pileup vertices within about two hundred proton-proton interactions per event.
A new muon system[82] will extend the coverage of muon detection to match the one of the inner tracker, bringing a benefit for many analysis, among which the search for $\tau \to 3\mu$.
Indeed, recent projections [83] show that the Phase-II upgrade will allow CMS to reach the sensitivity of 10^{-9} at 90% of confidence level on the $\tau \to 3\mu$ search (see Fig. 3.44), confirming the capability of the CMS experiment in the search for new physics processes

in the low-p_T region.

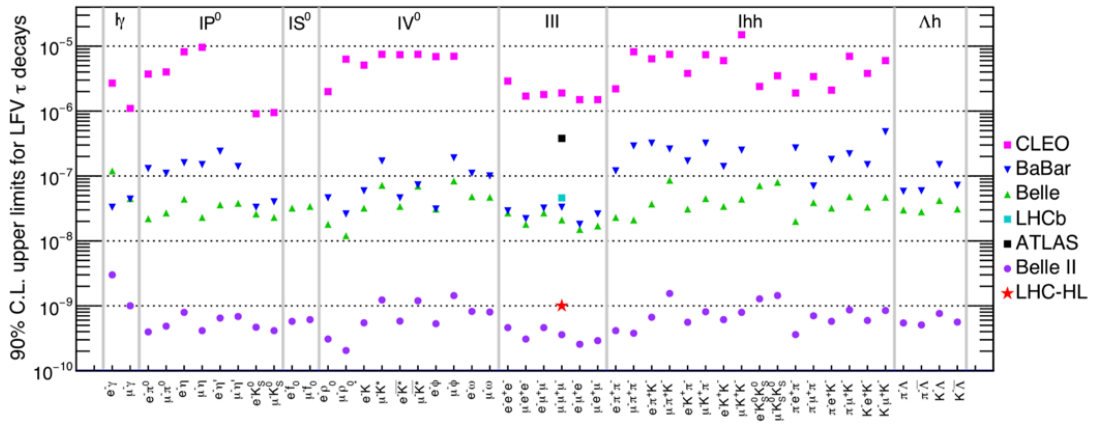

Figure 3.44: Predicted upper limits at the HL-LHC for many τ LFV decays. The CMS contribution to the $\tau \to 3\mu$ process is marked with a red star.

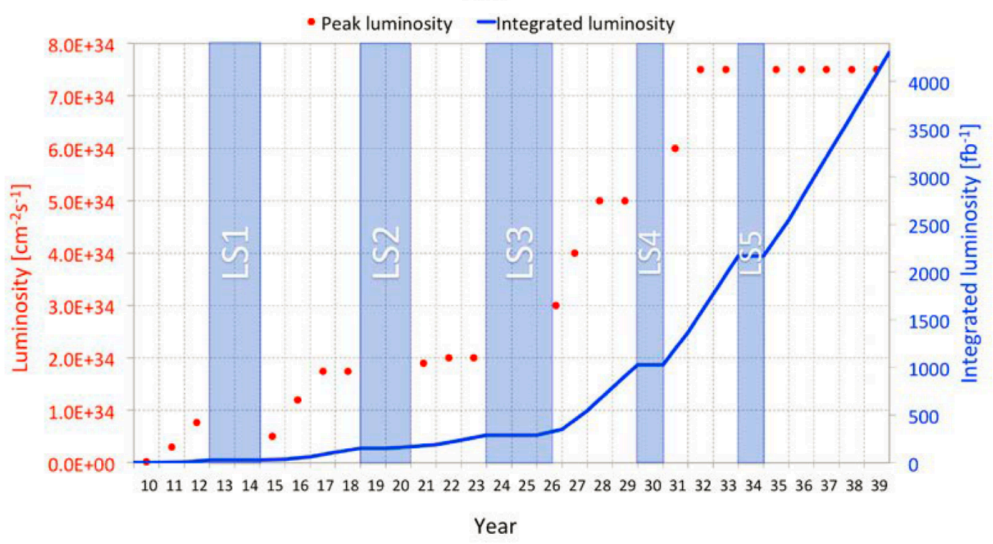

Figure 3.45: Scheduled profile of the instantaneous luminosity of the LHC. Phase-II is predicted to start in 2026, after the fourth long shutdown period.

Appendices

A Upper limit estimation

In this appendix the method used to derive the upper limit on the $\tau \to 3\mu$ branching fraction is described.
The upper limit on the branching fraction of physical process is an estimation, at a given confidence level (CL), of the maximum allowed signal strength which would be masked by the expected background. That is, the upper limit is an estimation of the sensitivity of the experiment to detect that process.

In order to asses an upper limit, a statistical model must be defined. The signal strength is derived with an unbinned maximum likelihood fit, and the likelihood function takes the form:

$$\mathscr{L}(\mu, \vec{\theta}) = \prod_i [b(x_i, \vec{\theta}) + \mu s(x_i, \vec{\theta})] \times \prod_j p_j(\theta_j) \tag{10}$$

where x_i are the observed values of the discriminant variable (the signal candidate invariant mass, in the case of this analysis), s is the signal model (describing the $\tau \to 3\mu$ process as a function of x), b is the background model (describing the standard model, as a function of x), μ is the signal strength (the parameter of interest), $\vec{\theta}$ is the vector of the nuisance parameters θ_j (fixed by some independent pre-fit measurements on data) and p_j their constraints.
The null hypothesis under test (H^{null}) is the signal-plus-background model, while the alternative hypothesis ($H^{alt.}$) is the background-only model. The test statistics used for upper limits computations is the so called LHC statistics, already in use by the CMS and ATLAS collaborations for the search of new physics processes, such as for search of the Higgs boson. The LHC test statistics takes the form:

$$\lambda_{\overline{\mu}} = \frac{\mathscr{L}(\overline{\mu}, \hat{\hat{\theta}} \mid \vec{x})}{\mathscr{L}(\hat{\mu}, \hat{\hat{\theta}} \mid \vec{x})} \tag{11}$$

$$q_{\overline{\mu}} = \begin{cases} -2\ln\lambda_{\overline{\mu}} & \hat{\mu} \leq \overline{\mu} \\ 0 & \hat{\mu} > \overline{\mu} \end{cases} \tag{12}$$

where the symbol $\hat{}$ denotes the maximum likelihood estimation of a parameter and $\hat{\hat{}}$ the profiled value of a parameter when fixing a value of $\mu = \overline{\mu}$. The choice of setting $\lambda_{\overline{\mu}}$ to zero for values of $\hat{\mu}$ greater than $\overline{\mu}$ is adopted in order to define a one-sided test, so that upward fluctuations of the signal yield do not serve as an evidence against the signal [84].
The probability distribution function (p.d.f) of $q_{\overline{\mu}}$, f, can be described by mean of asymptotic formulae [85], or with the use of simulated toy samples. In the case of this analysis, the toy approach is preferred, as the asymptotic limit validity is not guaranteed by the low number of events passing the final selections.

Given an observed value of $q_{\overline{\mu}}$ under $H^{alt.}$, $q_0^{obs.}$, a p-value can be defined as

$$p(q_{\overline{\mu}} \geq q_0^{obs.} \mid H^{null}) = \int_{q_0^{obs.}}^{\infty} f(q_{\overline{\mu}} \mid H^{null})\, dx \tag{13}$$

To state the sensitivity of a search, the median value of the background-only distribution of $q_{\overline{\mu}}$ is chosen as $q_0^{obs.}$.
First, the background-only p.d.f. is generated using a *blinded* dataset, where the background-only model is defined by some pre-fit values which are not updated during the limit computation. In the case of this analysis, the pre-fit values for the background model are obtained fitting the data sidebands (i.e. excluding the signal region), and the signal modelling is evinced from a MC sample, whose normalization is given by independent measurements of the signal selection efficiency, of the pp$\rightarrow$W cross section and of the W$\rightarrow \tau\nu$ branching fraction.
The value of $\overline{\mu}$ which gives a p-value of 1 - CL is defined as the *expected upper limit* on the $\tau \rightarrow 3\mu$ process. The confidence intervals at 68.3%, 94.5% and 99.7% of confidence level can be obtained substituting the corresponding quantiles of the background-only p.d.f. of $q_{\overline{\mu}}$ to the median, and are used to quote a credible interval for the expected upper limit. The blinding strategy ensures that no bias is put on the result estimation during the optimization steps of the analysis. Once the analysis strategy is finalized, the observed upper limit can be computed. In this case, the background model is initialized by its pre-fit values, which are updated with a fit on the full analysis range (i.e., including data coming from the signal region) during the limit computation. In case no signal evidence is present[16] the observed and expected upper limits must be in agreement.

[16]To test the significance of the fitted signal strength, a different statistical test is run [84, 85].

A.1 The CLs method

The procedure described in A represents a good approach for setting upper limits only in the case the null and the alternative hypothesis are well distinct, which means, if the false positive rate and the false negative rate (also known as type-I and type-II errors) are small. If this is not the case, the CLs approach (also known as p_{s+b} approach) is used. Instead of relying on the p-value of Eq. 13, the quantity CLs is used:

$$CLs = \frac{p(q_{\bar{\mu}} \geq q_0^{obs.} \mid H^{null})}{1 - p(q_{\bar{\mu}} \geq q_0^{obs.} \mid H^{alt.})} \tag{14}$$

The CLs method ensures the plausibility of the statistical approach described in A in case the sensitivity of the experiment is low.

B Corrections to the missing transverse momentum

This appendix describes how the missing energy is computed and corrected at CMS, and the correction adopted by the analysis.
The missing transverse momentum (also known as MET) is a measurement of the sum of the undetected particles transverse momentum of a collision event. By definition, it includes every possible source of momentum loss, being it neutrinos, new-physics particles, energy leakage or mis-reconstructions. The PF algorithm, described in Sec. 2.3.1, can reconstruct particle candidates using detector information; the PF missing transverse momentum is defined as the vector balancing the visible transverse momentum reconstructed by the algorithm.

$$MET = \sum_{vis} -\vec{p_T}^{vis} \tag{15}$$

B.1 Pileup-per-particle-identification correction

The PF MET definition includes, by construction, contribution to the missing energy from pileup interaction. However, it is useful for many analyses (such as the precision measurement of the W boson mass, the search for the Higgs boson in the $\tau\tau$ channel, or the search for the $\tau \to 3\mu$ process) to reduce the contamination of pileup, in order to improve the resolution of the leading vertex estimation of the MET. This is done via the PUPPI [86] algorithm.

For each particle in the event, the variable α is defined as

$$\alpha_i = \sum_j \frac{p_{Tj}}{\Delta R_{ij}} \times \Theta(\Delta R_{ij} - R_{min}) \times \Theta(R_{max} - \Delta R_{ij}) \tag{16}$$

where the index i identifies the particle under study, j runs over all the particles in the event, and Θ is the Heaviside step function.
The distribution of α can be computed for charged particles coming from PU interactions and from the leading vertex (LV) separately, as the tracker information allows to associate each particle to its vertex. Then, it is assumed that the same distribution is valid for neutral particles. Figure B.1 shows the distribution of α under different hypothesis, and validates the assumption done for neutral particles.

Then, the variable X^2 is defined

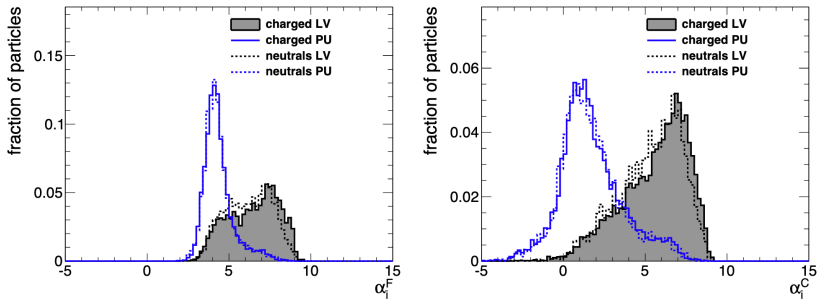

Figure B.1: The distribution of α_i, over many events, for particles i from the leading vertex (gray filled) and particles from pileup (blue) in a di-jet sample.

$$X_i^2 = \Theta(\alpha_i - \overline{\alpha}_{PU}) \times \frac{(\alpha_i - \overline{\alpha}_{PU})^2}{\sigma_{PU}} \tag{17}$$

where $\overline{\alpha}_{PU}$ is the median of the PU distribution of α and σ_{PU} its width.
As the distribution of α for PU particles is approximately gaussian, the p.d.f. of X^2 is a χ^2 distribution with one degree of freedom [86]. For each neutral particle, the complement to unity of the p-value computed at α_i is assigned as a weight to particle transverse momentum, while for charged particles the weight is either one or zero, based on the information from the tracker detector. Figure B.2 shows the mean weight distribution for PU and LV neutral particles, as a function of the particle p_T , as evaluated on a di-jet sample.
Figure B.3 shows the improvement on the estimation of the missing transverse momentum introduced by the PUPPI algorithm.

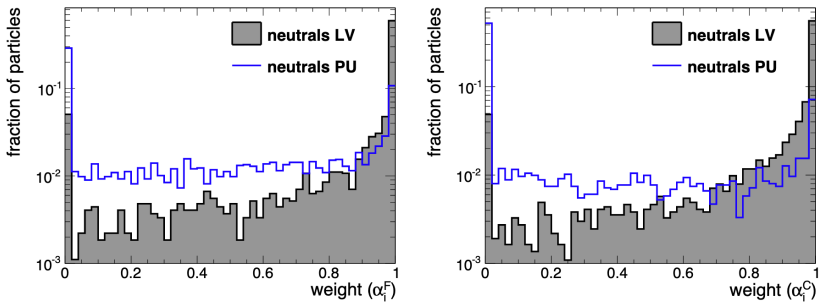

Figure B.2: The distribution of weights, over many events, for neutral particles i with $p_T > 1$ GeV from the leading vertex (gray) and particles from pileup (blue) in a di-jet sample, using events in the forward region of CMS (α_F) and in the central region of CMS (α_C).

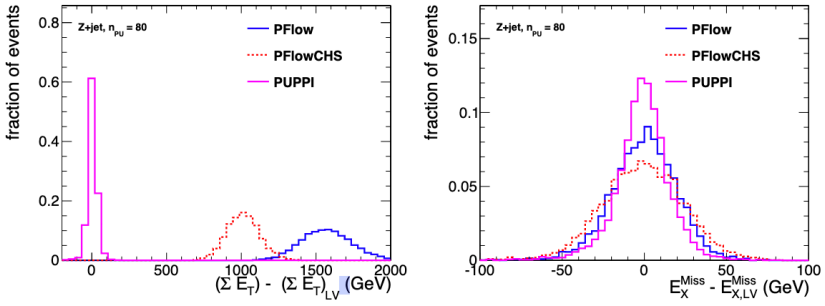

Figure B.3: The resolution of the MET (left) and the resolution of the x component of the MET (right) in $Z+$ jets events with 80 pileup vertices.

B.2 DNN correction

The correction to the PF missing energy applied in this analysis is achieved via a Deep Neural Network (DNN) developed at CMS, deepMET.
DeepMET uses the particle candidates reconstructed by the PF algorithm to derive corrections to the transverse components of the missing energy:

$$p_x^{miss} = \sum_i \omega_i \times p_{x,i} + b_{x,i} \quad (18)$$

$$p_y^{miss} = \sum_i \omega_i \times p_{y,i} + b_{y,i} \quad (19)$$

where the index i runs on all the PF candidates of the events, ω_i are the weights associated to each candidate, and b_i the biases.
The DNN is trained on a set of eight continuous variables (the impact parameter of the PF candidate in the transverse plane, its distance from the primary vertex in the z plane, its pseudorapidity, its transverse momentum, its mass, its x and y components of the momentum, and its PUPPI weight), and three categorical variables (the PF candidate charge, its pdg ID, and the information whether it comes from a primary vertex or not).
Figure B.4 shows the 15% improvement in the missing transverse momentum resolution observed on the $W\rightarrow \tau\nu$, $\tau \rightarrow 3\mu$ analysis simulated signal, and how it propagates to the estimation of the transverse mass of the τ-ν_τ final state.

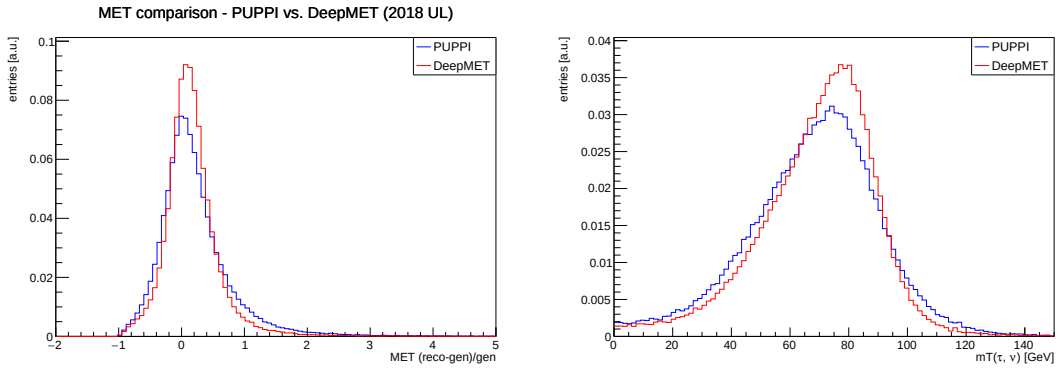

Figure B.4: Comparison of the deepMET (red) and PUPPI (blue) resolution (left) and transverse mass of the τ-ν_τ final state distribution (right).

C BDT features

This appendix presents the distribution of the features used to train the BDT of the W channel analysis. Background events are shown in red, signal events are shown in blue. Background distributions are obtained from data events lying outside the signal region (i.e. the sideband regions 1.6-1.74GeV and 1.82-2.0 GeV). Signal distributions are obtained from a simulated signal sample, as explained in Sec. 3.1.1.

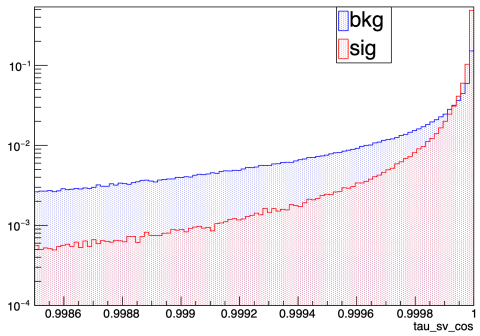

(a) Secondary vertex pointing angle

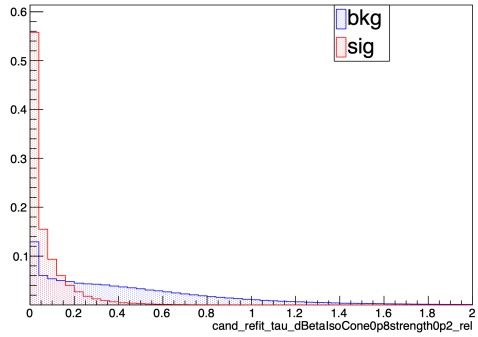

(b) Relative isolation of the τ candidate

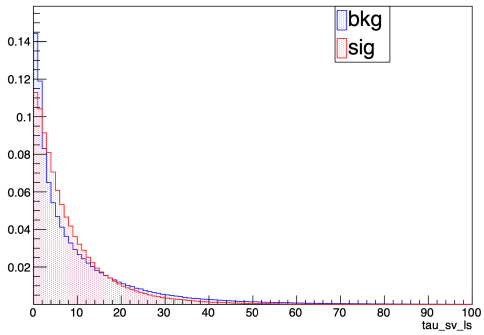

(c) Significance of the secondary vertex displacement

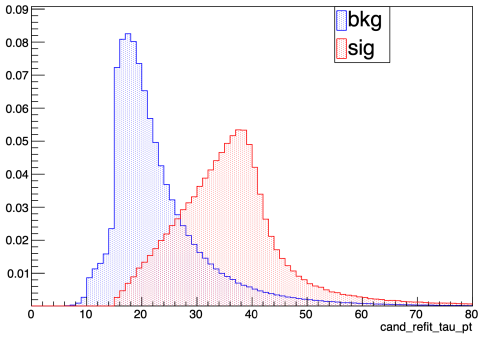

(d) Transverse momentum of the τ candidate

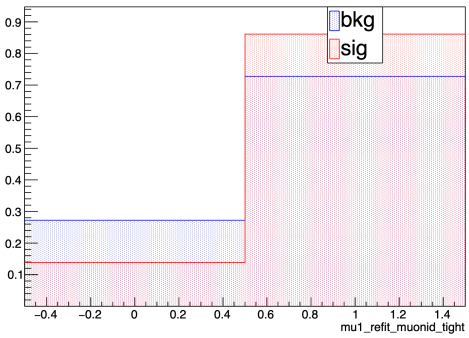

(e) TIght muon ID evaluated on the leading signal muon

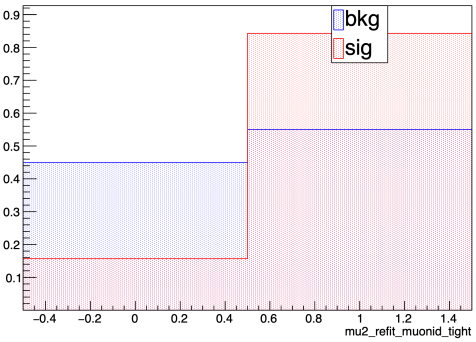

(f) Tight muon ID evaluated on the subleading signal muon

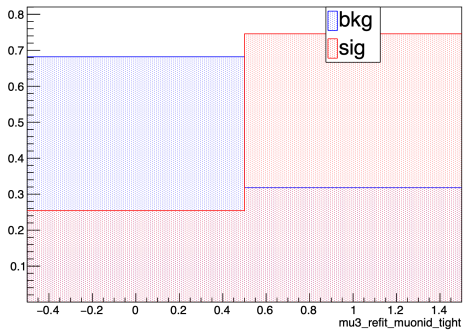

(g) Tight muon ID evaluated on the trailing signal muon

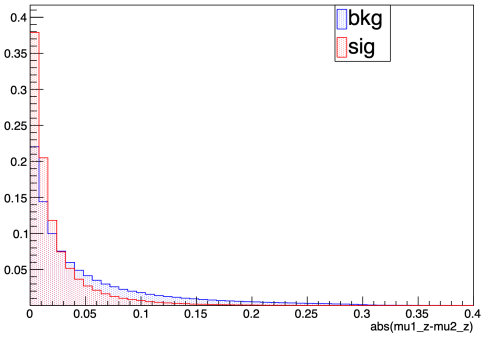

(h) Distance in the z direction between the leading and the subleading signal muons

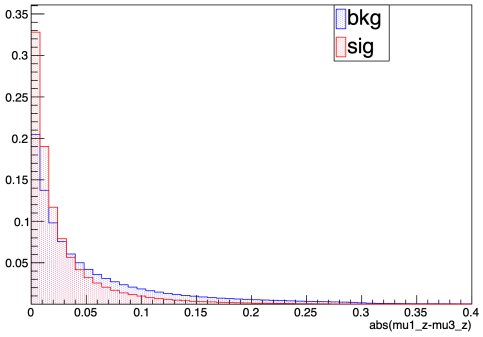

(i) Distance in the z direction between the leading and the trailing signal muons

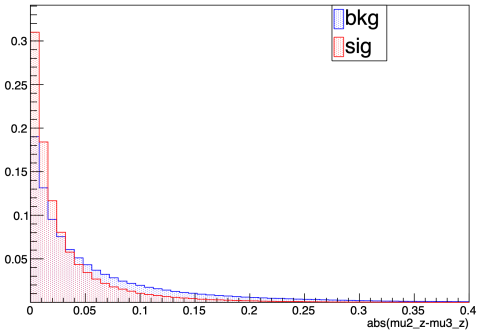

(j) Distance in the z direction between the subleading and the trailing signal muons

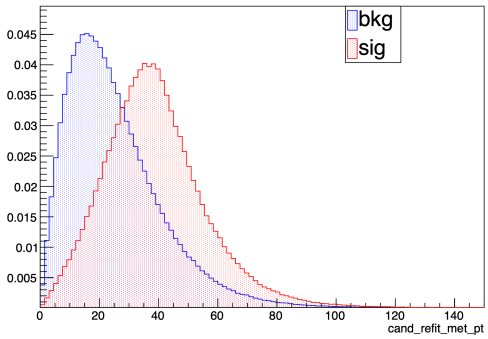

(k) Magnitude of the missing transverse momentum

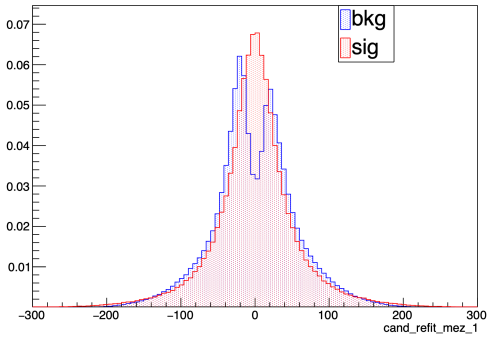

(l) Smaller solution of Eq. 3.3

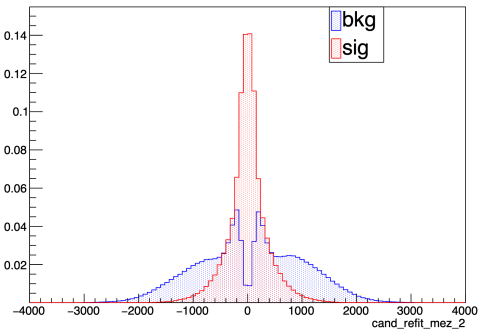

(m) Larger solution of Eq. 3.3

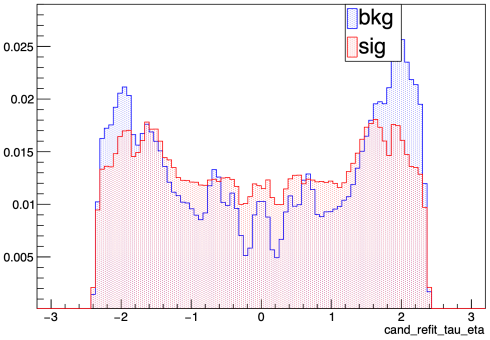

(n) Pseudorapidity of the τ signal candidate

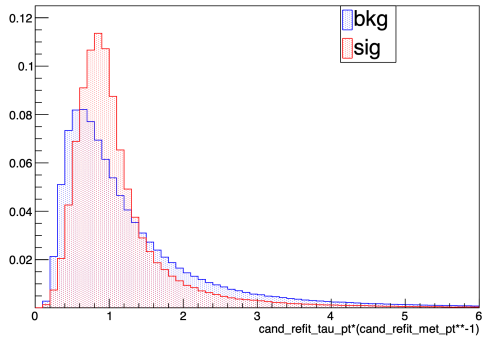

(o) Ratio of the τ signal candidate transcerse momentum and the missing transverse momentum

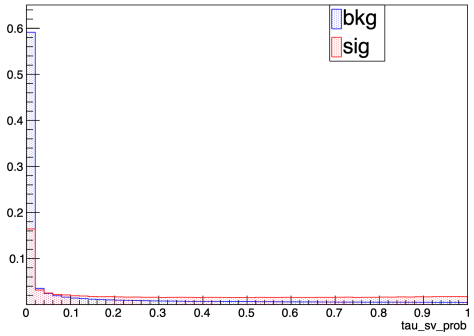

(p) Probability associated to the secondary vertex

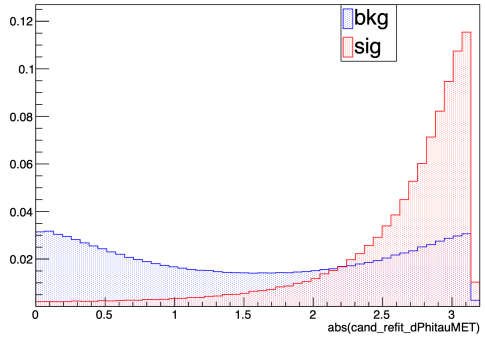

(q) Azimuthal angle distance between the τ candidate and the MET vector

Figure C.1: Distribution of the BDT input features evaluated on background events (blue) and signal events (red).

Bibliography

[1] Blackstone, Patrick and Fael, Matteo and Passemar, Emilie. $\tau \to \mu\mu\mu$ at a rate of one out of 10^{14} tau decays? *The European Physical Journal C*, 2020. 10.1140/epjc/s10052-020-8059-7.

[2] Marzia Bordone, Claudia Cornella, Javier Fuentes-Martín, and Gino Isidori. Low-energy signatures of the PS^3 model: from *B*-physics anomalies to LFV. *JHEP*, 2018. 10.1007/JHEP10(2018)148.

[3] K. Hayasaka, K. Inami, and Y. Miya. Search for lepton flavor violating tau decays into three leptons with 719 million produced tau+tau- pairs. *Phys. Lett. B*, 2010. 10.1016/j.physletb.2010.03.037.

[4] The ATLAS collaboration. Probing lepton flavour violation via neutrinoless $\tau \to 3\mu$ decays with the ATLAS detector. *Eur. Phys. J. C*, 2016. 10.1140/epjc/s10052-016-4041-9.

[5] The CMS collaboration. Search for the lepton flavor violating decay $\tau \to 3\mu$ in proton-proton collisions at $\sqrt{s} = 13$ TeV. *JHEP*, 2020. 10.1007/JHEP01(2021)163.

[6] M. E. Peskin and D. V. Schroeder. An introduction to quantum field theory. *CRC Press*, 1995. 10.1201/9780429503559.

[7] D. Griffiths. Introduction to the elementary particles. *Wiley*, 1987. 10.1002/9783527618460.ch1.

[8] C. Quigg. Electroweak symmetry breaking in historical perspective. *Ann. Rev. Nucl. Part. Sci.*, 2015. 10.1146/annurev-nucl-102313-025537.

[9] The ATLAS collaboration. Observation of a new particle in the search for the Standard Model Higgs boson with the ATLAS detector at the LHC. *Physics Letters B*, 2012. 10.1016/j.physletb.2012.08.020.

[10] The CMS collaboration. Observation of a new boson at a mass of 125 GeV with the CMS experiment at the LHC. *Physics Letters B*, 2012. 10.1016/j.physletb.2012.08.021.

[11] Seth H. Neddermeyer and Carl D. Anderson. Note on the nature of cosmic-ray particles. *Phys. Rev.*, 1937. https://doi.org/10.1103/PhysRev.51.884.

[12] Perl, Martin L. and others. Evidence for Anomalous Lepton Production in e+ - e- Annihilation. *Phys. Rev. Lett.*, 1975. 10.1103/PhysRevLett.35.1489.

[13] A. Bettini. Introduction to elementary particle physics. *Cambridge University Press*, 2008. 10.1017/CBO9780511809019.

[14] A. Pich. The Standard Model of Electroweak Interactions. *2006 European School of High-Energy Physics*, 2007. arXiv:0705.4264v1 [hep-ph].

[15] Takaaki Kajita. Atmospheric neutrino results from Super-Kamiokande and Kamiokande: Evidence for neutrino(mu) oscillations. *Nucl. Phys. B Proc. Suppl.*, 1999. 10.1016/S0920-5632(99)00407-7.

[16] Claudio Giganti, Stéphane Lavignac, and Marco Zito. Neutrino oscillations: The rise of the PMNS paradigm. *Prog. Part. Nucl. Phys.*, 2018. 10.1016/j.ppnp.2017.10.001.

[17] S. T. Petcov. The Processes $\mu \to e + \gamma, \mu \to e + \bar{e}, \nu' \to \nu + \gamma$ in the Weinberg-Salam Model with Neutrino Mixing. *Sov. J. Nucl. Phys.*, 1977. https://inspirehep.net/literature/109011.

[18] Xuan-Yem Pham. Lepton flavor changing in neutrinoless tau decays. *Eur. Phys. J. C*, 1999. 10.1007/s100529901088.

[19] M. Raidal et al. Flavour physics of leptons and dipole moments. *Eur. Phys. J. C*, 2008. 10.1140/epjc/s10052-008-0715-2.

[20] Ernesto Arganda and Maria J. Herrero. Testing supersymmetry with lepton flavor violating tau and mu decays. *Phys. Rev. D*, 2006. 10.1103/PhysRevD.73.055003.

[21] Roel Aaij et al. Test of lepton universality using $B^+ \to K^+ \ell^+ \ell^-$ decays. *Phys. Rev. Lett.*, 2014. 10.1103/PhysRevLett.113.151601.

[22] R. Aaij et al. Test of lepton universality with $B^0 \to K^{*0} \ell^+ \ell^-$ decays. *JHEP*, 2017. 10.1007/JHEP08(2017)055.

[23] J. P. Lees et al. Measurement of an Excess of $\bar{B} \to D^{(*)} \tau^- \bar{\nu}_\tau$ Decays and Implications for Charged Higgs Bosons. *Phys. Rev. D*, 2013. 10.1103/PhysRevD.88.072012.

[24] Roel Aaij et al. Measurement of the ratio of branching fractions $\mathscr{B}(\bar{B}^0 \to D^{*+} \tau^- \bar{\nu}_\tau) / \mathscr{B}(\bar{B}^0 \to D^{*+} \mu^- \bar{\nu}_\mu)$. *Phys. Rev. Lett.*, 2015. 10.1103/PhysRevLett.115.111803.

[25] Riccardo Barbieri, Gino Isidori, Andrea Pattori, and Fabrizio Senia. Anomalies in B-decays and $U(2)$ flavour symmetry. *Eur. Phys. J. C*, 2016. 10.1140/epjc/s10052-016-3905-3.

[26] Dario Buttazzo, Admir Greljo, Gino Isidori, and David Marzocca. B-physics anomalies: a guide to combined explanations. *JHEP*, 2017. 10.1007/JHEP11(2017)044.

[27] Lorenzo Calibbi, Andreas Crivellin, and Toshihiko Ota. Effective Field Theory

Approach to $b \to s\ell\ell^{(\prime)}$, $B \to K^{(*)}\nu\overline{\nu}$ and $B \to D^{(*)}\tau\nu$ with Third Generation Couplings. *Phys. Rev. Lett.*, 2015. 10.1103/PhysRevLett.115.181801.

[28] U. Bellgardt et al. Search for the Decay mu+ —> e+ e+ e-. *Nucl. Phys. B*, 1988. 10.1016/0550-3213(88)90462-2.

[29] A. M. Baldini et al. Search for the lepton flavour violating decay $\mu^+ \to e^+\gamma$ with the full dataset of the MEG experiment. *Eur. Phys. J. C*, 2016. 10.1140/epjc/s10052-016-4271-x.

[30] Gian F. Giudice, Gino Isidori, Alberto Salvio, and Alessandro Strumia. Softened Gravity and the Extension of the Standard Model up to Infinite Energy. *JHEP*, 2015. 10.1007/JHEP02(2015)137.

[31] N. Shimizu on behalf of the BELLE Collaboration. New Physics search in rare Tau decays at Belle and prospects at Belle II. *PoS*, 2016. 10.22323/1.280.0022.

[32] Boqun Wang. The belle ii experiment and superkekb upgrade. *J. Univ. Sci. Tech. China*. arXiv:1511.09434v2 [physics.ins-det].

[33] The BaBar collaboration and J. P. Lees. Limits on tau Lepton-Flavor Violating Decays in three charged leptons. *Phys. Rev. D*, 2010. 10.1103/PhysRevD.81.111101.

[34] The LHCb collaboration. Measurement of JPsi production in pp collisions at $\sqrt{s} =$ 7 TeV. *The European Physical Journal C*, 2011. 10.1140/epjc/s10052-011-1645-y.

[35] The LHCb collaboration. Prompt charm production in pp collisions at $\sqrt{s} = 7$ TeV. *Nucl. Phys. B*, 2013. 10.1016/j.nuclphysb.2013.02.010.

[36] P. Seyfert. The search for $\tau \to \mu\mu\mu$ at LHCb. *Heidelberg Univ.*, 2015-01-30. 10.11588/heidok.00018038.

[37] The CMS collaboration. Measurement of inclusive W and Z boson production cross sections in pp collisions at $\sqrt{s} = 13$ TeV. *CERN Document Server*, 2015. cds.cern.ch/record/2093537.

[38] Nobuhiro Shimizu. New Physics search in rare τ decays at Belle and prospects at Belle II. *PoS*, 2017. 10.22323/1.280.0022.

[39] The CMS collaboration. CMS Physics: Technical Design Report Volume 1: Detector Performance and Software. *CERN Document Server*, 2006. cds.cern.ch/record/922757.

[40] J.M. Jowett et al. The 2015 heavy-ion run of the LHC. *International Particle Accelerator Conference*, 2016. doi:10.18429/JACoW-IPAC2016-TUPMW027.

[41] Public CMS luminosity information. `https://twiki.cern.ch/twiki/bin/view/CMSPublic/LumiPublicResults`.

[42] G. Apollinari and O. Bruening and T. Nakamoto and L. Rossi. High Luminosity

Large Hadron Collider HL-LHC. *CERN Yellow Rep.*, 2017. 10.5170/CERN-2015-005.1.

[43] J. Wenninger. Beam Loss and Accelerator Protection. *Proceedings of the 2014 Joint International Accelerator School*, 2014. 10.5170/CERN-2016-002.

[44] C. Wyss. The LHC Magnet Programme: From Accelerator Physics Requirements to Production in Industry. *7th European Particle Accelerator Conference*, 2000. cds.cern.ch/record/466530.

[45] The TOTEM collaboration. First measurement of elastic, inelastic and total. *Eur. Phys. J. C*, 2017. 10.1140/epjc/s10052-019-6567-0.

[46] Irene Dutta. Precision Timing with the CMS MIP detector. *13th Conference on the Intersections of Particle and Nuclear Physics*, 2018. arXiv:1810.00350v1 [physics.ins-det].

[47] Simone Paoletti. The CMS Tracker Upgrade for the High Luminosity LHC. *CERN Document Server*, 2019. 10.22323/1.364.0138.

[48] V. Veszpremi on behalf of the CMS Collaboration. Operation and performance of the CMS tracker. *JINST*, 2014. 10.1088/1748-0221/9/03/C03005.

[49] The CMS collaboration. The CMS tracker system project: Technical Design Report. *CERN Document Server*, 1997. cds.cern.ch/record/368412.

[50] L. Borrello on behalf of the CMS collaboration. Overview of the CMS detector performance in LHC Run II. *5th International Conference on New Frontiers in Physics*, 2017. 10.1051/epjconf/201716407023.

[51] M. Dragicevic. The New Silicon Strip Detectors for the CMS Tracker Upgrade. *Tech. Univ. of Vienna*, 2010.

[52] Simon Spannagel. Status of the CMS Phase I Pixel Detector Upgrade. *Nucl. Instrum. Meth. A*, 2015. 10.1016/j.nima.2016.03.028.

[53] N. Parashar. CMS Pixel Detector Upgrade. 2011. arXiv:1110.2125v1 [physics.ins-det].

[54] The CMS collaboration. Description and performance of track and primary-vertex reconstruction with the CMS tracker. *JINST*, 2014. 10.1088/1748-0221/9/10/P10009.

[55] A. Massironi. Precision electromagnetic calorimetry at the energy frontier: CMS ECAL at LHC Run 2. 2015. arXiv:1510.02745v1 [physics.ins-det].

[56] Chatrchyan, Serguei and others. The performance of the CMS muon detector in proton-proton collisions at $\sqrt{s} = 7$ TeV at the LHC. *JINST*, 2013. 10.1088/1748-0221/8/11/P11002.

[57] Sirunyan, A. M. and others. Particle-flow reconstruction and global event description with the CMS detector. *JINST*, 2017. 10.1088/1748-0221/12/10/P10003.

[58] G. Abbiendi. The CMS muon system in Run2: preparation, status and first results. *PoS*, 2015. 10.22323/1.234.0237.

[59] Workbook Muon Analysis. https://twiki.cern.ch/twiki/bin/view/CMSPublic/WorkBookMuonAnalysis.

[60] Baseline muon selections for Run-II. https://twiki.cern.ch/twiki/bin/view/CMS/SWGuideMuonIdRun2.

[61] The CMS collaboration. The CMS trigger system. *JINST*, 2016. 10.1088/1748-0221/12/01/P01020.

[62] S. Dasu et al. CMS. The TriDAS project. Technical design report, vol. 1: The trigger systems. *CERN Document Server*, 2000. cds.cern.ch/record/706847.

[63] Sergio Cittolin, Attila Rácz, and Paris Sphicas. CMS The TriDAS Project: Technical Design Report, Volume 2: Data Acquisition and High-Level Trigger. CMS trigger an data-acquisition project. *CERN Document Server*, 2002. cds.cern.ch/record/578006.

[64] Albert M Sirunyan et al. Performance of the CMS muon trigger system in proton-proton collisions at $\sqrt{s} = 13$ TeV. *JINST*, 2021. 10.1088/1748-0221/16/07/P07001.

[65] M.C. Fouz T. Hebbeker P. Paolucci G. Rakness, C. Battilana. Performance of the CMS muon detector and reconstruction with protonproton collisions at $\sqrt{s} = 13$ TeV. *JINST*, 2018. 10.1088/1748-0221/13/06/P06015.

[66] MiniAOD. https://twiki.cern.ch/twiki/bin/viewauth/CMS/MiniAOD.

[67] Sj, Torbj. The PYTHIA Event Generator: Past, Present and Future. *Comput. Phys. Commun.*, 2020. 10.1016/j.cpc.2019.106910.

[68] Albert M Sirunyan et al. Extraction and validation of a new set of CMS PYTHIA8 tunes from underlying-event measurements. *Eur. Phys. J. C*, 2020. 10.1140/epjc/s10052-019-7499-4.

[69] Peter Skands, Stefano Carrazza, and Juan Rojo. Tuning PYTHIA 8.1: the Monash 2013 Tune. *Eur. Phys. J. C*, 2014. 10.1140/epjc/s10052-014-3024-y.

[70] The NNPDF collaboration. A first determination of parton distributions with theoretical uncertainties. *Eur. Phys. J. C*, 2019. arXiv:1905.04311v3 [hep-ph].

[71] Daniele Bertolini, Philip Harris, Matthew Low, and Nhan Tran. Pileup per particle identification. *Journal of High Energy Physics*, 2014. 10.1007/JHEP10(2014)059.

[72] The CMS collaboration. Performance of reconstruction and identification of tau leptons in their decays to hadrons and tau neutrino in LHC Run-2. *CERN Document Server*, 2016. cds.cern.ch/record/2196972.

[73] E Chabanat and N Estre. Deterministic Annealing for Vertex Finding at CMS. 2005. 10.5170/CERN-2005-002.287.

[74] The CMS collaboration. Muon tracking performance in the CMS Run-2

Legacy data using the tag-and-probe technique. *CERN Document Server*, 2020. cds.cern.ch/record/2724492.

[75] Chen, Tianqi and Guestrin, Carlos. XGBoost: A Scalable Tree Boosting System. *Association for Computing Machinery*, 2016. 10.1145/2939672.2939785.

[76] The CMS collaboration. Muon Identification performance: hadron mis-Id measurements and RPC Muon selections. *CERN Document Server*, 2014. cds.cern.ch/record/1712503.

[77] The CMS collaboration. CMS luminosity measurement for the 2017 data-taking at $\sqrt{s} = 13$ TeV. *CERN Document Server*, 2018. cds.cern.ch/record/2621960.

[78] The CMS collaboration. CMS luminosity measurement for the 2018 data-taking at $\sqrt{s} = 13$ TeV. *CERN Document Server*, 2019. cds.cern.ch/record/2676164.

[79] The Particle Data Group. `http://pdg.lbl.gov/`.

[80] The CMS collaboration. The Phase-2 Upgrade of the CMS Tracker. *CERN Document Server*, 2017. cds.cern.ch/record/2272264.

[81] Collaboration CMS. A MIP Timing Detector for the CMS Phase-2 Upgrade. *CERN Document Server*, 2019. cds.cern.ch/record/2667167.

[82] The CMS collaboration. The Phase-2 Upgrade of the CMS Muon Detectors. *CERN Document Server*, 2017. cds.cern.ch/record/2283189.

[83] A. Cerri et al. Opportunities in Flavour Physics at the HL-LHC and HE-LHC. *CERN Yellow Rep. Monogr.*, 2019. 10.23731/CYRM-2019-007.867.

[84] E. Gross. Practical Statistics for High Energy Physics. *CERN Yellow Rep. School Proc.*, 2018. doi.org/10.23730/CYRSP-2017-004.165.

[85] Glen Cowan, Kyle Cranmer, Eilam Gross, and Ofer Vitells. Asymptotic formulae for likelihood-based tests of new physics. *Eur. Phys. J. C*, 2011. 10.1140/epjc/s10052-011-1554-0.

[86] Daniele Bertolini, Philip Harris, Matthew Low, and Nhan Tran. Pileup Per Particle Identification. *JHEP*, 2014. 10.1007/JHEP10(2014)059.